FINAL MASTER'S PROJECT

**Master in materials science and engineering**

# OPTIMAL FEEDSTOCK COMPOSITION TO CONTROL THE POROSITY IN SOLID OXIDE FUEL CELL PRODUCED BY ADDITIVE MANUFACTURING



**Report and Annexes**

**Author:** Laura Cabezas i Peñalva
**Director:** Joan Josep Roa Rovira
**Call for proposal:** June 2020

# Abstract

Nowadays, the research of alternatives power resources has a huge importance in the society to develop new and eco-friendly systems to reduce the climate change. One good and studied option is the solid oxide fuel cells (SOFC), however, with the conventional shapes produced by using traditional processing routes, these systems present low efficiency. Within this context, one way to improve it is creating a high specific surface, and this can be achieved by means of the additive manufacturing (AM) technique.

During the last decade, the AM has been the manufacturing technique of the future, thanks of the advantages that it provides; being one of the most important advantages the ability to print complex geometries like honeycomb among others.

The purpose of this final Master's project is the combination of these two fields, following the work developed by myself during my Bachelor's project and some posterior work. In this case the idea is focused the project on the optimization of the resolution of the SOFC. As well as try to obtain the best feedstock composition to achieve the optimal porosity for each part. In addition, through this Master's project, a continuity on this AM field implemented within the CIEFMA group (Centre for Structural Integrity and Reliability of Materials) of the Department of Materials Science and Engineering (CEM) UPC's, can be assured, opening new applications of AM combined with the energy field.

To carry out this study, the used materials were: 8Y-TZP for the electrolyte, Lanthanum gallate strontium and magnesium doped for the cathode and gadolinium oxide for the anode. This study was divided in three parts; the first one consisted in an evaluation of the particle size, by using the laser diffraction particle size technique (also known as Mastersizer) and some scanning electron microscopy micrographs, with a step to process the powder and modify the size. In a second phase the best composition was search trying different ink compositions. The main rheological parameters for the optimal ceramic pastes (G', G'') will be studied. As a final step a cylindrical sample was printed by robocasting. Afterwards, the microstructural (e.g. density, phases, etc.) and micromechanical properties (e.g. hardness, elastic modulus, fracture mechanisms, etc.) will be determined by using advanced characterization techniques, like field emission scanning electron microscopy, focused ion beam, nanoindentation among others, to assure a minimal mechanical integrity of SOFC parts.

# Resum

Avui dia, la recerca de recursos energètics alternatius té una enorme importància en la societat per a desenvolupar sistemes nous i més sostenibles amb el medi ambient per a reduir l'efecte del canvi climàtic. Les piles de combustible d'òxid sòlid (SOFC) són una bona alternativa la qual ha estat bastant estudiada. No obstant això, les rutes de fabricació tradicionals fan que aquests sistemes presentin una baixa eficiència. En aquest context, una manera de millorar aquesta eficiència és crear una elevada superfície específica en la pila, cosa que es pot aconseguir mitjançant l'ús de la tècnica de Fabricació Additiva (AM).

Durant l'última dècada, la Fabricació Additiva ha estat la tècnica de fabricació del futur, gràcies als avantatges que proporciona; sent un dels més destacats la capacitat d'imprimir geometries complexes, exemple; la bresca d'abella.

El propòsit d'aquest treball de final de Màster (TFM) és la combinació d'aquests dos camps, seguint amb treballs previs com el meu treball de final de Grau (TFG) o altres treballs posteriors al TFG. En aquest cas el projecte es centra en millorar la resolució d'una SOFC. Així com tractar d'obtenir la millor composició de les tintes ceràmiques usades per a imprimir, intentant aconseguir la porositat òptima per a cada part de la SOFC. A més, a través d'aquest TFM, es pot assegurar una continuïtat del tema de Fabricació Additiva, a més d'obrir noves opcions d'aplicacions que combinen Fabricació additiva amb energia dins del grup CIEFMA (Centre d'Integritat Estructural i Fiabilitat dels Materials) del Departament de Ciència i Enginyeria dels Materials (CEM) de la UPC.

Per a dur a terme aquest estudi, es van utilitzar els següents materials: 8Y-TZP per a l'electròlit, Lantani Gal·li i Estronci dopat amb Magnesi (LSGM) per al càtode i òxid de Gadolini per a l'ànode. Aquest estudi es va dividir en tres parts; la primera va consistir en una avaluació del tamany de la pols ceràmica, utilitzant la tècnica de difracció làser pel tamany de les partícules (també coneguda com Mastersizer) i algunes micrografies de microscòpia electrònica d'escombratge (SEM). Després a aquesta pols se li va aplicar un processament químic per a modificar la seva mida. En una segona fase es va buscar la millor composició de les tintes d'impressió. Les quals es va estudiar els principals paràmetres reològics (G', G''). Com a pas final, es va imprimir una mostra cilíndrica per robocasting usant les composicions òptimes per a cada part. Posteriorment, es van determinar les propietats microestructurale com; densitat o fases. I micromecániques; duresa, mòdul elàstic o mecanismes de fractura. Per a això es van utilitzar tècniques avançades de caracterització, com la microscòpia electrònica d'escombratge d'emissió de camp, el feix d'ions focalitzats i la nanoindentación, entre altres, tot amb l'objectiu d'assegurar una mínima integritat mecànica de les piles de combustible.

UNIVERSITAT POLITÈCNICA DE CATALUNYA
BARCELONATECH
Escola d'Enginyeria de Barcelona Est

# Resumen

Hoy en día, la investigación de recursos energéticos alternativos tiene una enorme importancia en la sociedad para desarrollar sistemas nuevos y más amigables con el medioambiente para reducir el efecto del cambio climático. Las pilas de combustible de óxido sólido (SOFC) son una buena alternativa la cual ha estado bastante estudiada. Sin embargo, las rutas de fabricación tradicionales hacen que estos sistemas presenten una baja eficiencia. En este contexto, una forma de mejorar esta eficiencia es crear una elevada superficie específica en la pila, cosa que se puede lograr mediante el uso de la técnica de Fabricación Aditiva (AM).

Durante la última década, la Fabricación Aditiva ha sido la técnica de fabricación del futuro, gracias a las ventajas que proporciona; siendo una de las que más destaca la capacidad de imprimir geometrías complejas, ejemplo; el panal de abeja.

El propósito de este trabajo de final de Máster (TFM) es la combinación de estos dos campos, siguiendo con trabajos previos como mi trabajo de final de Grado (TFG) u otros trabajos posteriores al TFG. En este caso el proyecto se centra en mejorar la resolución de una SOFC. Así como tratar de obtener la mejor composición de las tintas cerámicas usadas para imprimir, intentando lograr la porosidad óptima para cada parte de la SOFC. Además, a través de este TFM, se puede asegurar una continuidad del tema de Fabricación Aditiva, además de abrir nuevas opciones de aplicaciones que combinan Fabricación aditiva con energía dentro del grupo CIEFMA (Centro de Integridad Estructural y Fiabilidad de los Materiales) del Departamento de Ciencia e Ingeniería de los Materiales de la UPC.

Para llevar a cabo este estudio, se utilizaron los siguientes materiales: 8Y-TZP para el electrolito, Lantano Galio y Estroncio dopado con Magnesio (LSGM) para el cátodo y óxido de Gadolinio para el ánodo. Este estudio se dividió en tres partes; la primera consistió en una evaluación del tamaño de polvo cerámico, utilizando la técnica de difracción láser del tamaño de las partículas (también conocida como Mastersizer) y algunas micrografías de microscopía electrónica de barrido (SEM). Después a este polvo se le aplico un procesado químico para modificar su tamaño. En una segunda fase se buscó la mejor composición de las tintas de impresión. Las cuales se estudió los principales parámetros reológicos (G', G''). Como paso final, se imprimió una muestra cilíndrica por robocasting usando las composiciones óptimas para cada parte. Posteriormente, se determinaron las propiedades microestructurale como; densidad o fases. Y micromecánicas; dureza, módulo elástico o mecanismos de fractura. Para ello se utilizaron técnicas avanzadas de caracterización, como la microscopía electrónica de barrido de emisión de campo, el haz de iones focalizados y la nanoindentación, entre otras, todo con el objetivo de asegurar una mínima integridad mecánica de las pilas de combustible.

UNIVERSITAT POLITÈCNICA DE CATALUNYA
BARCELONA**TECH**
Escola d'Enginyeria de Barcelona Est

UNIVERSITAT POLITÈCNICA DE CATALUNYA
BARCELONATECH
Escola d'Enginyeria de Barcelona Est

# Acknowledgements

The work presented in this final Master's project would not have been possible to accomplish without guidance, motivation, help and knowledge of many people.

First of all I would like to express generous gratitude Luis Llanes CIEFMA group leader and Joan Josep Roa my supervisor, to give me the chance to follow with my work on this topic, and having full confidence in myself and my work.

I would like to acknowledge to my master's colleagues that we made a really nice group and we gave each other moral support and assistance during these two years of the master. It was not easy, we had to work hard but we also had really nice moments.

To finish, I am very thankful to my parents. They are my moral support not just during this project, and they always try to find the positive side of all the things, especially during these moths of work for this project. We have experienced an exceptional and hard situation, but together we have gone forward.

UNIVERSITAT POLITÈCNICA DE CATALUNYA
BARCELONA**TECH**
Escola d'Enginyeria de Barcelona Est

# Glossari

**AE:** Auger electrons

**AFM:** Atomic force microscopy

**AM**: Additive manufacturing

**ASC:** Airbrushed solution combustion

**A ($h_c$):** Contact area

**BSE:** Backscattered electrons

**CAD:** Computer-aided design

**CIP:** Cold isostatic pressing

**CSM:** Cntinous stiffness measurement

**DED:** Direct energy deposition

**DLMS:** Direct laser metal sintering

**DLP:** Digital laser processing

**E:** Elastic modulus

**$E_{eff}$:** Effective modulus

**EBM:** Electron beam method

**FD:** Fraünhofer diffraction theory

**FESEM:** Field emission electron microscopy

**FIB:** Focused ion beam

**Fx:** Feedstock number 'x'

**G:** Shear modulus

**G\*:** Complex shear modulus

**G':** Storage modulus

**G":** Lost modulus

**Gd:** Gadolinium (III)

**GDC:** Gadolinium doped ceria

**GIS:** Gas injection system

**H:** Hardness

**h:** Displacement into surface

**HIP:** Hot isostatic pressing

**HOR:** Hydrogen oxidation reaction

**IIT:** Instrumented Indentation Technique

**LDC:** Lanthanium doped ceria

**LDS:** Laser diffraction spectrometry

**LOM:** Laminated object manufacturing

**LSGM:** Lanthanum gallate strontium and magnesium doped

**OCV:** Open circuit voltage

**ORR:** Oxygen reduction reaction

**P:** Applied load

**PBF:** Powder bed fusion

**PEN:** Positive electrode, electrolyte, negative electrode

**PEO:** Polyethylene oxide

**PPO:** Polypropylene oxide

**R:** Indenter radius

UNIVERSITAT POLITÈCNICA DE CATALUNYA
BARCELONATECH
Escola d'Enginyeria de Barcelona Est

**rpm:** Revolution per minute

**RP:** Rapid prototyping

**SE:** Secondary electrons

**SEM:** Scanning electron microscopy

**SLM:** Selective laser melting

**SLS:** Selective laser sintering

**SOE:** Solid oxide electrolysers

**SOFC:** Solid oxide fuel cell

**SR:** Steam reforming

**TPB:** Triple phase boundary

**TT:** Thermal treatment

**UAM:** Ultrasonic additive manufacturing

**XR:** X-ray

**YSZ**: Yttria-stabilised zirconia

**8Y-TZP**: Tetragonal zirconia partial stabilized with 8 molar percentage of yttria

**γ:** Strain

**γ̇:** Shear rate

**η:** Viscosity

**σ:** Stress

**τ:** Shear stress

UNIVERSITAT POLITÈCNICA DE CATALUNYA
BARCELONATECH
Escola d'Enginyeria de Barcelona Est

# Table of contents

UNIVERSITAT POLITÈCNICA DE CATALUNYA
BARCELONATECH
UPC  Escola d'Enginyeria de Barcelona Est

UNIVERSITAT POLITÈCNICA DE CATALUNYA
BARCELONATECH
Escola d'Enginyeria de Barcelona Est

UNIVERSITAT POLITÈCNICA DE CATALUNYA
BARCELONATECH
Escola d'Enginyeria de Barcelona Est

# 1. Preface

This Master's thesis comes out from some previous works done by myself during almost three years in the Structural Integrity, Micromechanics and Reliability of Materials (CIEFMA) research group, one from the Department of Materials Science and Engineering (CEM) from "Universitat Politècnica de Catalunya-BarcelonaTech, UPC".

Because of that, during this chapter some previous projects and results will be commented with the aim to present the context of this work and in consequence the reasons which brings us to follow this line of work.

## 1.1    Origin of the project

In September 2017, I started a research stage during four months in the CIEFMA's group at the Department of Materials Science and Engineering under the supervision of Dr. Joan Josep Roa Rovira. During this period, I was working in the following topic: "*Microstructural and micromechanical correlation of zirconia based ceramic samples produced by Rapid Prototyping*". The main goal of this project was tried to improve the 3D printing process using the Robocasting machine from the group. The used material was ceramic based zirconia with different molar percentage of yttria ($Y_2O_3$); 3Y-TZP, 8Y-TZP and 10Y-TZP, which it means zirconia partial stabilized with 'x' molar percentage of $Y_2O_3$. We were able to produce samples with a relative density higher than 90%, and with mechanical properties, Hardness and elastic modulus, comparable with samples produced by convention processing routes, like cold isostatic pressing (CIP).

In February 2018, my final Bachelor's project starts. Due to the good results obtained during this research stage, we decided to implement the additive manufacturing (AM) technique to create a final product. We decided to go through the energy applications because of the positive collaboration with IREC (Catalan Institute of Research of Energy), which is a centre that one of the groups are been working on SOFC (Solid Oxide Fuel Cells). So the main goal of the project was to print an electrolyte of a SOFC by AM with different shapes. The results were positive; two different geometries, tubular and hexagonal were obtained as depicted in *Figure 1.1*.

UNIVERSITAT POLITÈCNICA DE CATALUNYA
BARCELONA**TECH**
Escola d'Enginyeria de Barcelona Est

*Figure 1.1: Electrolyte geometries from the Bachelor's project. Left: tubular geometry and right: hexagonal one.*

All of them were microstructural and micromechanical characterized giving good final properties, similar than those reported in the literature and obtained by traditional processing routes. The project was complemented with the applying of Dip Coating technique of the material for the cathode, with the aim to study the adhesion between both parts by means of the scratch technique.

During the following year (2018-2019), the idea to create an entire functional SOFC appears due to the results from my bachelor's project. And under the Reserch Start grands from UPC (INIREC-UPC fellowship) I was able to follow with that in CIEFMA. The first step was tried to be able to control and study the internal porosity of the manufactured samples. For that we applied a technique called: Micro-computered tomography, Micro-CT, which is based on X-ray diffraction. This technique was hugely used for hydroxyapatite scaffolds from the biomaterials group of the department, to study the porosity and structure of them. Because of that, we think that this machine would be useful for us. It was applied on three different samples; one fully dense zirconia based ceramic materials, another one printed with the same material but with porosity heterogeneously distributed inside the specimen. And finally, one hard metal (WC-Co) based sample obtained through the Binder Jetting technology and supplied by the Fraunhofer Institute for Manufacturing Technology and Advanced Materials (Dresden, Germany). The first observation was that materials with a high atomic weight, like both studied materials presented problems because of the high reflection. So the conclusions were that the technique can be useful for porous samples and for materials with low atomic number. Also the size of the sample would affect on the final resolution of the tomography, when we talk about materials with a high atomic weight.

The following step was to try to improve one of the comments from my Bachelor's project, the resolution of printed samples. To go through that the needed of use a smaller nozzle was the best way to get it and reduce the subsequent post-processing routes, like polishing. From our experience the particle size needs to be 10 times smaller than the nozzle diameter, to have a good flowability. Within this context, in the first part of this final Master's project talk about these results that were presented on an international Conference; *Shaping 7*, in Aveiro, Portugal, in September 2019.

For this final Master's project and following with this presented previous work, the logical step was try to print the three parts separately of a SOFC, to find the best feedstock composition and to get the most suitable ceramic ink in order to print each part with the desired porosity. The results will be

UNIVERSITAT POLITÈCNICA DE CATALUNYA
BARCELONATECH
Escola d'Enginyeria de Barcelona Est

used in the future, since they represent the previous step for the final long term goal, to print a functional SOFC.

## 1.2 Motivation

One of the main motivations to do this Master's project was to follow with all this previous work done in that field. But the main question to answer is; *why do we want to use additive manufacturing as a technique to fabricate a SOFC?*

Nowadays, the additive manufacturing (AM) is a worldwide methodology widely employed in many fields, e.g. energy, bioengineering, among others. Within this context, the AM methodology presents a growing trend due to it allows develop complex geometries with similar microstructural and mechanical properties for the specimens performed with the conventional processing techniques; e.g. cold and hot isostatic pressing (CIP and HIP, respectively), etc.

A SOFC is a green source of energy widely studied, because it can be a good replacement for the conventional and non-renewable source of energies. One of the main problems is the efficiency of them. This device is based on a redox reaction which it means that it needs to pick up oxygen from one part and hydrogen from the other. The efficiency of a SOFC will come from the capacity of the device to perform the needed reactions. For that as much specific surface it presents, higher probability that the reaction occurs.

One way to generate a high specific surface is through the generation of complex geometries, and here is when AM comes. One of the strong points of AM is the freedom of the final geometry that you can generate. So that is why we decide to combine SOFC with AM, with goal to enhance the efficiency.

Finally, the **motivation** to work specifically on this Master's project is that the final results will represent the previous step to start to print an entire SOFC. Because if we are able to print each part separately with the properly conditions it will mean that each part will be optimized.

# 2. Introduction

## 2.1 Additive Manufacturing

The ISO/ASTM 52900-15, define Additive manufacturing (AM) as; *a process of joining materials to make objects from 3D model data, usually layer upon layer, as opposed to subtractive manufacturing methodologies* [1]*.

Thanks to that the final geometry can be chosen arbitrarily without the need to modify the rest of the manufacturing process, the AM gives rise to the appearance of a great number of opportunities within the scientific and industrial field, being considered one of the great revolutions of the 21$^{st}$ century.

### 2.1.1 Why Additive Manufacturing?

Apart from saving money and time, the following advantages are the main reasons why nowadays the AM is the most popular and suitable technique to design new materials in front of traditional techniques [2]:

1. A physical model that can be delivered quickly from Computer-Aided Design (CAD) documents, can permit form, fit and function tests much prior in the design cycle.
2. Errors from incorrect interpretation of the design are reduced and designs to prototype iterations are faster.
3. It is possible to go from a CAD model to a prototype without using a skilled machinist, a fixture designer.
4. Core/Cavity can be built for plastic moulding, investment casting, and die-casting applications.
5. Apart from directly producing plastic prototype models, some of the parts produced can be used as patterns for investment or sand casting, depending on the technology used.
6. For producing dies and moulds longer lead-time is required. By AM technology, tooling can be produced in a shorter time, is needed a few hours to get the green body sample and after that perform the heat treatment in order to get a dense and mechanically resistant component. This helps in bringing the products to the market in a lesser time.
7. With appropriate materials, the model can be utilized as a part of consequent assembling operations to create the final parts. This also serves as a manufacturing technology.

UNIVERSITAT POLITÈCNICA DE CATALUNYA
BARCELONA**TECH**
Escola d'Enginyeria de Barcelona Est

### 2.1.2 Different production methodologies

There are many techniques depending on the morphology and final properties required for the desired pieces with a complex geometry. According to the standards exists 7 different AM techniques [1]:

**a) Vat photopolymerization**

A vat of liquid photopolymer resin is cured through selective exposure to light (via a laser or projector) which then initiates polymerization and converts the exposed areas to a solid part. This technique presents a high level of accuracy and complexity. The final sample has a smooth surface finish. And it can accommodate large build areas, so the drawback of the size limitation is reduced [1].

*The typical material used is an ultraviolet (UV)-curable photopolymer resin that performs as a binder, and it is usually filed with ceramic powder.* Not all the ceramics can be applied, because one of the key parameters for the success of this technique is the scattering of the emitted light, that it will be influenced by the refractive index of the ceramic particles. It is obvious that a high scattering is not desired, so the used ceramics will have low refractive index [3]. So this fact can be considered as the major drawback of Vat photopolymerization technique. A schematic representation of this technique is shown in *Figure 2.1.*
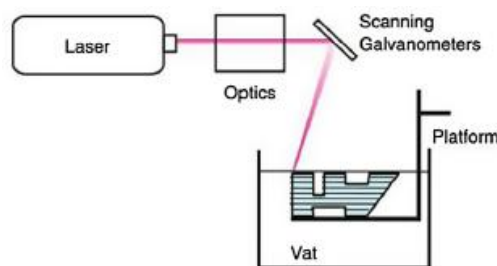


*Figure 2.1: Schematics representation of vat polymerization process with one type of light source* [4].

**b) Powder bed fusion**

Powdered materials are selectively consolidated by melting it together using a heat source such as a laser or electron beam. The infused powder surrounding the consolidated part acts as a support material for overhanging features. The final sample can present a high level of complexity on the geometry. The powder acts as support material, and a wide range of materials can be used [1]. It allows selecting different materials including plastics, glass, metals and its alloys. Recyclable is also a remarkable quality of Powder bed fusion (PBF) process. Powder used

in process can be recycled to produce more parts. **Figure 2.2** shows a picture to represent the PBF process [5].
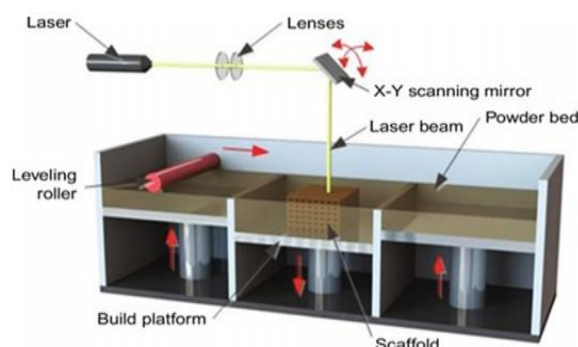
Therefore, some different type of fusion technique are used in PBF process, and they can be sub-divided into; Selective Laser Sintering (SLS), Electron Beam Method (EBM), Selective Laser Melting (SLM) and Direct Laser Metal Sintering (DLMS). In **Table 2.1** a brief description of each technique with some examples of usage is shown.

*Table 2.1: A brief overview of the different PBF sub-groups* [5].

| Technique | Brief description | Applications |
|-----------|-------------------|--------------|
| SLS | A layer of powder is laid down and a $CO_2$ laser sintered at the points selected on 2D cross-section of the model. The platform gradually descends in accordance with the height of the layer defined | This method is highly suited for biomedical applications such as pre-surgical planning, prosthetics and bone scaffolds for tissue engineering |
| EBM | The energy source for the melting processes is an electron beam emitted from a tungsten filament and controlled by coil, it also uses a computer controlled electron gun | Aerospace, medical or orthopedic implant industries and automotive industries |
| SLM | The powder is melted rather than sintering. It is faster than SLS but requires inert gases for laser | Metallic materials, for high quality and precision applications |
| DLMS | An object is developed with the use of metal powders. It is a layer by layer process with computer controlled laser technique | Titanium and its alloys are widely used for various implants in the orthopedic and dental field |

But this technique presents some drawbacks; first this process is very time-consuming process, because it needs pre-heat powder, vacuum generation and the building time is very high.

Structural properties of parts are not very good as compared to other manufacturing techniques. As structural property, surface property is also poor due to layer by layer manufacturing [5].

**c) Binder jetting**

Liquid bonding agents are selectively applied onto thin layers of powdered material to build up parts layer by layer. The binders include organic and inorganic materials. Metal or ceramic powdered parts are typically fired in a furnace after they are printed to achieve the final properties. So a wide range of materials can be applied apart from metals and ceramics. In this sense, also plastic materials can be used. This technique presents a high productivity. Binder jetting allows a full colour printing process [1]. A schematic diagram of this technique is shown in *Figure 2.3*.
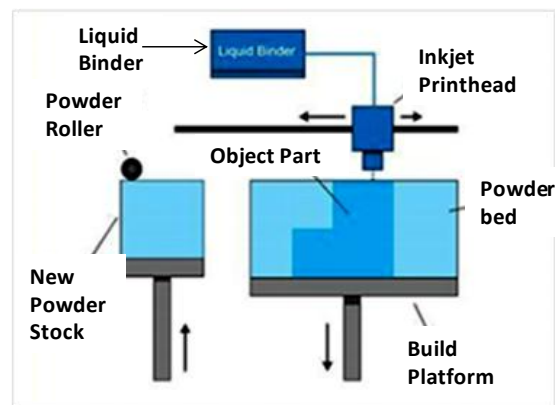


*Figure 2.3: Schematic diagram of a binder jetting machine* [5].

**d) Material jetting**

The concept is the same as an inkjet printer, droplets of material are deposited layer by layer to make parts. Common varieties include jetting a photo curable resin and curing it with UV light, as well as jetting thermally molten materials that then solidify in ambient temperatures. The typical used materials are photopolymers, polymers and waxes [1]. So the limitation of printable materials is the main drawback of this technique. Nevertheless, the final sample presents a high level of accuracy regarding the CAD model. Also during the process different materials can be combined and be printed. Finally, as the technique above it also allows a full colour printing process. A material jetting machine developing some samples is shown in the *Figure 2.4*.

UNIVERSITAT POLITÈCNICA DE CATALUNYA
BARCELONA**TECH**
Escola d'Enginyeria de Barcelona Est

*Figure 2.4: Developed product through Material Jetting in AM process* [5].

### e) Sheet lamination

Sheets of material are stacked and laminated together to form an object. The lamination method can use adhesives or chemical bonding (paper/plastics), ultrasonic welding, or brazing (metals). Unneeded regions are usually cut layer by layer and removed after the object is built. As it is just said the typical materials used in this technique are paper, plastic sheets and metal foil or tapes, *Figure2.5* shows an example of this technique [1]. Sheet lamination included two types of processes Ultrasonic Additive Manufacturing (UAM), which combines ultrasonic metal seam welding and milling in the lamination process. It is capable of construction of metal structures at low temperature. The other type is Laminated Object Manufacturing (LOM) which is based of layer-by-layer cutting and lamination of sheets or rolls of materials. Successive layers are cut precisely using a mechanical cutter or laser and are then bonded together [5].



*Figure 2.5: Sheet laminated process* [5].

As a strength of this methodology allows the fabrication of samples with a high volumetric build rates. It is relatively low cost, except for metallic foils. And it allows for combinations of metal foils, including embedding components [1].

### f)  Material extrusion

Material is extruded through a nozzle or orifice in tracks or beads, which are then combined into multi-layer models. Common varieties include heated thermoplastic extrusion (similar to a hot glue gun) and syringe dispensing. The most typical printable materials are; thermoplastic filaments and pellets. Some types of machines based on this technique use syringe to deposit the printing material, in this case liquids and slurries charged with powders are used. A schematic representation is shown in *Figure 2.6*.
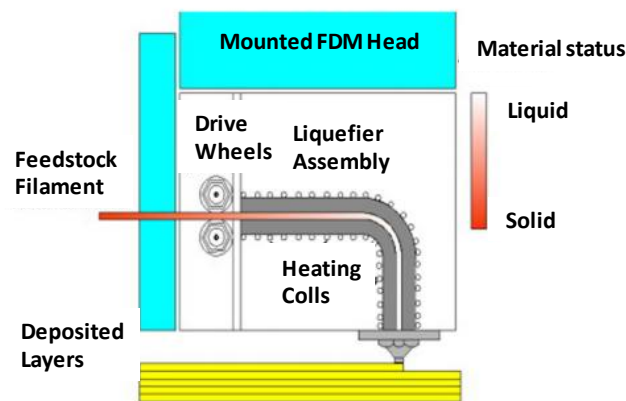


*Figure 2.6: Schematic representation of the fused deposition modelling process. One specific technique from material extrusion [4].*

The main strengths of this process are: (1) it is an economical process, (2) it allows printing in a multiple colours, (3) it can be used in environmental conditions and (4) the final parts have good structural properties [1].

During this Master's project, the robocasting technique is going to be used. This technique is classified in the category of material extrusion, that use syringe as a tool to deposit the material layer by layer. In our case, robocasting is support with a gear system that moves the piston to extrude the material throw the nozzle, this technique will be explained in detail in *chapter 4.3.*

### g)  Direct energy deposition

Direct energy deposition (DED) consists of a nozzle mounted on a multi axis arm which deposited melted material on the surface where it solidifies. Generally, titanium and cobalt chrome materials are used in this process. On the other hand, polymers and ceramic materials are not suitable to be used as a feedstock in this printing technology. This technique has an ability to control grain structure at high degree [5]. A schematic diagram of the DED methodology is shown in *Figure 2.7*.
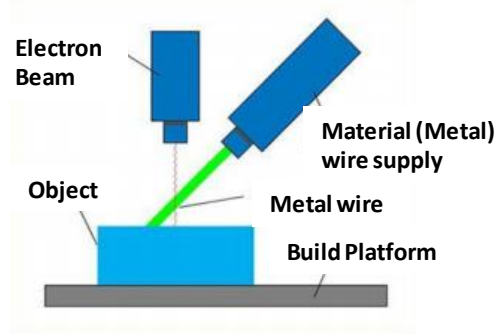
UNIVERSITAT POLITÈCNICA DE CATALUNYA
BARCELONATECH
Escola d'Enginyeria de Barcelona Est

***Figure 2.7****: Schematic representation of the DED process* [5]*.*

This technique presents the following strength: (1) There is no limitation by direction or axis, (2) it is effective for repairs and adding features, (3) multiple materials can be added in a single part and (4) a highest single-point deposition rates exist during the process [1].

Can be considered an eighth category; *Hybrid techniques*. But at the end, it consists on the combination of the seven categories of AM techniques. And try to give a description with some strength and the typical used material is quite complicate. The reason of that is the main idea of this technique, which is try to combine the best parts of some different AM techniques, so at the end this hybrid technology is going to be specific for each application.

### 2.1.3 Advantages and disadvantages

One of the main characteristics of AM that represent strength, in comparison with other techniques, is the versatility of materials to print. All kind of them can be printed; ceramics, metals, polymers, even composites with multilayer of multimaterial systems. The other remarkable characteristic is the possibility to create complex geometries. Apart of these characteristics, the following **<u>advantages</u>** can be found [2]:

1. <u>Material efficiency</u>: Unlike conventional subtractive manufacturing where large amount of materials need to be removed, AM uses raw materials efficiently by building parts layer by layer. Leftover materials can often be reused with minimum processing.
2. <u>Resource efficiency</u>: Conventional manufacturing processes require auxiliary resources such as jigs, fixtures, cutting tools, and coolants in addition to the main machine tool. AM does not require these additional resources. As a result, parts can be made by small manufacturers that are close to customers. This presents an opportunity for improved supply chain dynamics.
3. <u>Part flexibility</u>: Because there are no tooling constraints, parts with complex features can be made in a single piece. In other words, there is no need to sacrifice part functionality for the ease of manufacture. In addition, it is possible to build a single part with varying mechanical

UNIVERSITAT POLITÈCNICA DE CATALUNYA
BARCELONA**TECH**
Escola d'Enginyeria de Barcelona Est

properties (flexible in one part and stiffer in another). This opens up opportunities for design innovation in terms of microstructural and mechanical design only by designing complex microstructures.

4. Flexibility: AM machines do not require costly setups and hence is economical in small batch production. The quality of the parts depends on the process rather than operator skills. As such, production can be easily synchronized with customer demand. In addition, the problems of line balancing and production bottle-necks are virtually eliminated because complex parts are produced in single pieces

Despite this, AM technology still cannot fully competitive with the conventional manufacturing techniques, especially in the mass production field because of the following **drawbacks**:

1. Size limitations: AM processes often use liquid polymers, or a powder comprised of resin or plaster, to build object layers. These materials render AM unable to produce large-sized objects due to lack of material strength. Large-sized objects also often are impractical due to the extended amount of time need to complete the build process [2].

2. Anisotropic mechanical properties: Anisotropic behaviour is one of the main challenges of AM. Because of the nature of layer-by-layer printing, the microstructure of the material inside each layer is different compared to that of at the boundaries between layers. Anisotropic behaviour results in the different mechanical behaviour of the 3D printed part under vertical tension or compression compared to that in the horizontal direction [6].

3. Defects: One of the most typical defects that appear during an AM process are voids. The additional porosity created by AM can be very high and can thereby reduce mechanical performance due to the reduction of interfacial bonding between printed layers. The other one is the surface roughness due to the layer-by-layer appearance. The appearance may not be an important factor if the 3D printed part is hidden in the final application e.g. in scaffolds for tissue engineering. However, in other applications such as buildings, toys and aerospace, a flat surface is preferred compared to the layer-by-layer appearance [6].

4. Divergent from design to execution: CAD software is the main tool to design a part that can be 3D printed. Because of limitations in AM, the printed part can have a few defects that were not expected in the designed element. The CAD system is a combination of solid geometry and boundaries. It typically employs meshing concepts to approximate the model. However, transferring CAD into a 3D printed part often results in inaccuracies and defects particularly in curved surfaces.

   A very fine mesh can potentially resolve this problem to some extent, but the computed processing and printing will be time-consuming and complicated. Therefore post-processing (by heat, laser, chemicals or sanding) to eliminate these defects are sometimes considered [6].

UNIVERSITAT POLITÈCNICA DE CATALUNYA
BARCELONATECH
Escola d'Enginyeria de Barcelona Est

5. <u>Cost</u>: AM equipment is considered an expensive investment. Entry level 3D printers average approximately 2,500€ and can go as high as 25,000€ for higher-end models, not including the cost of accessories and resins or other operational materials [2].

### 2.1.4 Applications

Due to all the advantages presented in ***section 2.1.3,*** this methodology can be applied on different fields with different requirements and final applications. Within this context, the AM technique presents an application in fields like:

- <u>Biomedical:</u> In this field, AM can be used for; orthopedic implants, tissue engineering, medical devices, micro-vasculature networks, biologic chips and bioprinting with the aim to fabricate functional organs. This last application represents the newest one. It has emerged as the most innovative solution to the healthcare catastrophe of organ shortage and transplantation. Bioprinting makes use of rapid prototyping (RP) technology to print cells and biomaterials individually or in tandem, one layer over the other, producing 3D tissue-like structures which can be reorganized and regrouped together to form vascularised organs. 3D bioprinting is based on three principle approaches: *biomimicry, autonomous self-assembly and mini-tissue building blocks* [7]. In ***Figure 2.8*** some examples of these devices are shown.
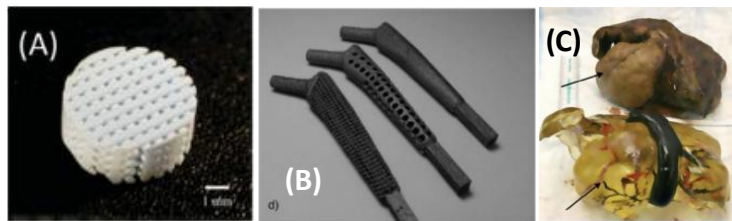


***Figure 2.8:*** *a) Hydroxyapatite scaffold fabricated by robocasting, b) Ti6Al4V hip prosthesis fabricated by electron-beam melting and c) Actual liver of a recipient and 3D printed liver. The arrows in **Figure 2.8.c** indicate a regenerative nodule in both and 3D printed liver and the native liver [4].*

- <u>Aerospace:</u> It has incorporated AM process from concept design to end use parts and repairs. The areas of applications include rapid prototyping (RP) of components in the design phase using plastic and metal followed by making of dies/mould/tools for mass production and direct manufacture of complex shape metal parts, repairing of damaged parts instead of scrapping or replacement of them. In aero engines, the increase in the operating temperature will have direct impact on fuel efficiency. AM has the potential to process higher temperature materials such as nickel alloys and inter metallic materials which are difficult to cast and machine [8]. Additionally, aerospace production is usually small, limited to a maximum of several thousand parts [2], allowing the AM a suitable technique to be employed in this field. An example of an aerospace component is shown in ***Figure 2.9.a.***

- Automotive: To fabricate new products. This process is critical for the automotive industry, due to it is often a very costly and time-consuming process. The automotive industry has been using AM technology as an important tool in the design and development of automotive components because it can shorten the development cycle and reduce manufacturing and product costs. AM processes also have been used to make small quantities of structural and functional parts, such as engine exhausts, drive shafts, gear box components and breaking systems for luxury, low volume vehicles. Unlike passenger cars, vehicles for motorsports usually use light-weight alloys (e.g. titanium, etc.) and have highly complex structures and low production volumes. Companies and research institutes also have successfully applied AM techniques to manufacture functional components and complements for racing vehicles [2], *Figure 2.9.b*.

- Buildings: This sector is in its infancy as it started to use AM for residential structures only from 2014, and has shown great potential since then. Automated building construction with 3D printing technology has gained increasing attention in recent years. It can potentially revolutionize the construction industry and it can offer astronauts easier construction on the moon. It offers a significant reduction in construction time and manpower.

- Energy: This field has an important role on this project, because the technique of AM is a good way to generate complex fuel cells, like the solid oxide fuel cells (SOFCs) that is depicted in *Figure 2.9.d*, which is a good solution to reduce the dependence of fossil energy due to provide great advantages such as high efficiency, high power density, and low emissions. The potential applications include portable power supply, automotive system, and distributed power system compared with the traditional energies [2]. Apart for SOFC application AM technique is used to produce devices for energy absorption, catalytic applications and power storage.
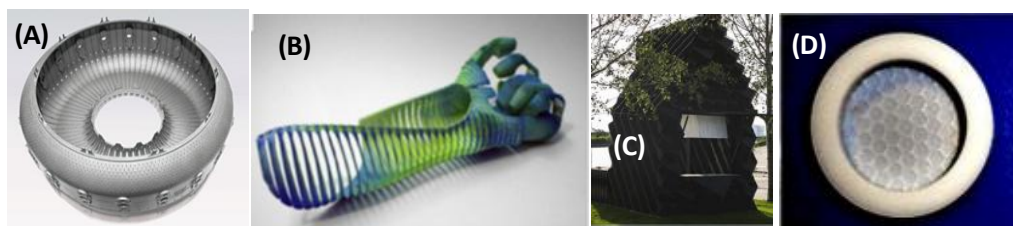


*Figure 2.9*: *a) Jet engine combustor of nickel alloy made with direct metal laser sintering* [9]*, b) 3D printed multi-material motorcycle "glove"* [10] *, c) First 3D printed house by DusArchitects* [6] *and d) an electrolyte 3D printed of 3Y-TZP* [11]*.

In this Master's project, we will centre our attention to develop new devices to be employed in the energy field, concretely; we will focus our attention on SOFC developed through the AM technology. More information about the Fuel Cells and in particular to the SOFC cells can be found in **section 2.2.**

## 2.2    Fuel cells

This Master's project is focused to develop AM components for energy applications, in particular SOFCs. It is a type of fuel cell base on ceramic and cermet materials. It explains why this fuel cell is called solid oxide, because there is one type of ceramic materials which are formed as an oxide of a metal element. It will give special properties and work modes as a fuel cell. During this section we are going to give an overview about SOFC, trying to explain the operation of the device, some characteristics, types of SOFC...

### 2.2.1 Theoretical background of SOFC

The SOFC, like other fuel cells, is an electrochemical device for the conversion of chemical energy of a fuel into electricity and heat. The fuel, for example, hydrogen is not combusted but electro-oxidized at the anode (fuel electrode) by oxygen ions conducted across the electrolyte according to the ***equation 1***.

$$H_{2(g)} + O^{2-} \rightarrow H_2O_{(g)} + 2e-$$ **equation 1**

The liberated electrons pass through an external circuit to arrive at the cathode (air electrode) where they reduce molecular oxygen (present in air) to oxide ions, following the ***equation2***.

$$O_{2(g)} + 2e^- \rightarrow O^{2-}$$ **equation 2**

Water vapour is produced at the anode diluting the fuel. The hydrogen oxidation reaction (*HOR*) and the oxygen reduction reaction (*ORR*) occur at the triple phase boundary (*TPB*) zone where the electrode (electronic phase), electrolyte (ionic phase) and gas phase (hydrogen, air) are in contact. Generally, the *TPB* is viewed as a surface occupying a small finite volume which extends into the electrodes [12].

SOFC usually operates at temperatures ranged between 800 and 1000°C. The SOFC consists of cathode, electrolyte and anode collectively referred to as the *PEN* – positive electrode, electrolyte, negative electrode. A single cell operated with hydrogen and oxygen provides at equilibrium a theoretical reversible (Nernst) or open circuit voltage (*OCV*) of 1.229 V at standard conditions (*T* = 273.15 K, *P* = 1 atm) [12]. ***Figure 2.10*** presents a diagram of electric power generation in a fuel cell with an oxygen ion-conducting electrolyte.
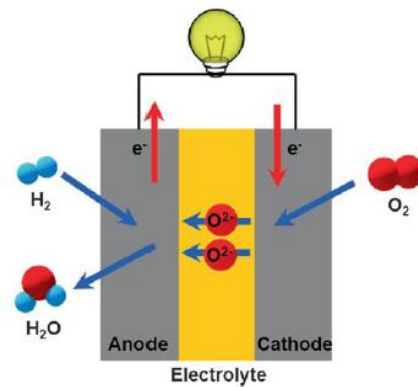
*Figure 2.10: Schematic diagram of electric power generation using a fuel cell with an oxygen ion-conducting electrolyte* [13].

Low emissions and high energy conversion efficiency are two distinguished properties of SOFC technology because the energy generation process described above is not limited by the Carnot cycle. If the power and heat cogeneration mode is considered, an overall efficiency of greater than 80% can be achieved. In addition, the subsequent $CO_2$ sequestration becomes easier because the effluent gas of fuel cells is not diluted by nitrogen, which means that zero $CO_2$ emission is possible during energy utilization using advanced SOFC technology. Furthermore, elevated operation temperatures promote kinetic electrochemical oxidation and chemical oxidation/reforming of the carbonaceous fuel reactions [13]. These high operating temperatures also impose stringent material and processing requirements. For this reason, the present key technological challenge facing ceramic fuel cells is the development of a suitable pair of materials (electrolyte/anode and cathode/electrolyte) with a high adherence under working conditions. Furthermore, produce a pair of materials with a similar dilatation coefficient in order to reduce the residual stresses generated during the thermal fatigue produced under working conditions (cooling-heating and re-cooling process for many years). In this sense, the different constituents of the fuel cells play an important role, for this reason, more information related to each constitutive part is briefly explained in ***section 2.2.3.***

### 2.2.2 Characteristics

In general, all kind of fuel cells present the followings characteristics [14]:

1. High conversion efficiency: The primary feature of a fuel cell is its high fuel-to-electricity conversion efficiency ranged between 45 to 60%. A fuel cell converts the chemical energy of fuel directly into electrical energy. Thus, the usual losses involved in the conversion of fuel to heat, to mechanical energy, and then to electrical energy are avoided. The efficiency of a fuel cell is further improved when the by-product heat is fully utilized (in cogeneration or bottoming cycles).

UNIVERSITAT POLITÈCNICA DE CATALUNYA
BARCELONATECH
Escola d'Enginyeria de Barcelona Est

2. <u>Environmental compatibility</u>: Fuel cells are capable of using practical fuels as an energy source with insignificant environmental impact. Emissions of key pollutants from fuel cells are several orders of magnitude lower than those produced by conventional power generators. Production of undesirable materials such as $NO_x$, $SO_x$, and particulates is either negligible or undetectable for fuel cell systems.

3. <u>Modularity</u>: Fuel cells have the characteristic of modularity, i.e., cells can be made in modular sizes. Thus, fuel cell size can be easily increased or decreased. Since the efficiency of a fuel cell is relatively independent of size, fuel cells can be designed to follow loads with fast response times without significant efficiency loss at part-load operation.

4. <u>Sitting flexibility</u>: Because fuel cells can be made in a variety of sizes, they can be placed at different locations with minimum sitting restrictions. Fuel cell operation is quiet because a fuel cell has no moving parts; the only noises are those from auxiliary equipment. Consequently, fuel cells can be easily located near points of use such as urban residential areas.

5. <u>Multifuel capability</u>: Certain types of fuel cells have multifuel capability. High-temperature fuel cells can process (reform) hydrocarbon fuels internally and do not need expensive subsystems to process conventional fuels into simple forms.

### 2.2.3 SOFC constituents: Cathode, Electrolyte and Anode

A SOFC is typically composed of a porous electrodes and a dense electrolyte. The dense electrolyte separates the anode and the cathode into two gas chambers that are fed with fuel and oxidant gases, respectively. Sometimes, between the electrodes and the electrolyte and interconnectivity layer is added to promote the adhesion between parts.

In *table 2.2*, the main requirements to give stability to the SOFC are exposed.

UNIVERSITAT POLITÈCNICA DE CATALUNYA
BARCELONA**TECH**
Escola d'Enginyeria de Barcelona Est

***Table 2.2:*** *Requirements for ceramic fuel cell component* [14].

| Components | Requirements | | | | |
|---|---|---|---|---|---|
| | **Conductivity** | **Stability** | **Compatibility** | **Porosity** | **Thermal expansion** |
| **Electrolyte** | High ionic conductivity. Negligible electronic conductivity | Chemical, phase, morphological, dimensional, stability in oxidant environments | No damaging chemical interactions or interdiffusion with adjoining cell components | Fully dense | Thermal expansion match with adjoining components |
| **Cathode** | High electronic conductivity | Chemical, phase, morphological, dimensional stability in oxidant environments | No damaging chemical interactions or interdiffusion with adjoining cell components | Porous | Thermal expansion match with adjoining components |
| **Anode** | High electronic conductivity | Chemical, phase, morphological, dimensional stability in fuel environments | No damaging chemical interactions or interdiffusion with adjoining cell components | Porous | Thermal expansion match with adjoining components |
| **Interconnect** | High ionic conductivity. Negligible electronic conductivity | Chemical, phase, morphological, dimensional stability in oxidant and fuel environments | No damaging chemical interactions or interdiffusion with adjoining cell components | Fully dense | Thermal expansion match with adjoining components |

### 2.2.4 Types

A fuel cell electrolyte must ironically conduct one of the elements present in the fuel or oxidant. Thus, a solid electrolyte for SOFCs based on the electrochemical reactions of hydrogen and oxygen must conduct either oxygen ions or hydrogen ions, protons. The present generation of ceramic fuel cells can be classified into two types [14]:

1. **Oxygen-ion-conducting electrolytes***: **Figure 2.11*** exhibits the reaction of this type of electrolyte. It can be considered as an oxygen concentration cell. In this case the water is

UNIVERSITAT POLITÈCNICA DE CATALUNYA
BARCELONA**TECH**
Escola d'Enginyeria de Barcelona Est

produced in the fuel side. This type of SOFC is the one that is going to try to be AM technology during this Master's project.



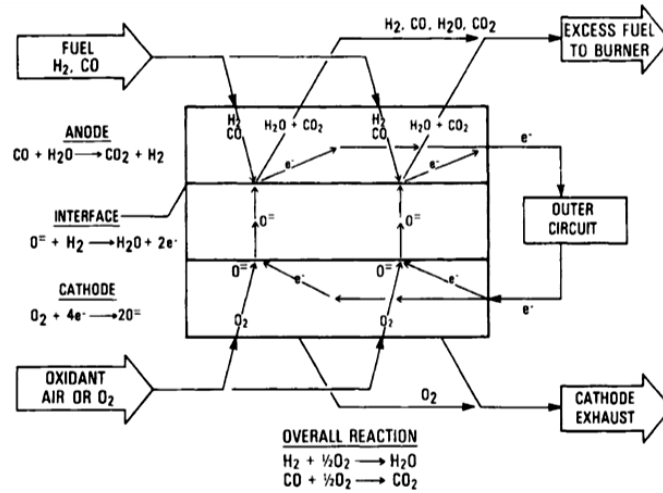**Figure 2.11:** *Diagram of reactions in SOFCs based on oxygen-ion-conduction* [14]*.*

2. **Proton-conducting electrolytes:** *Figure 2.12* presents the reaction of this type of electrolyte. It can be considered as a hydrogen concentration cell. On this type, the water is produced in oxidant side.
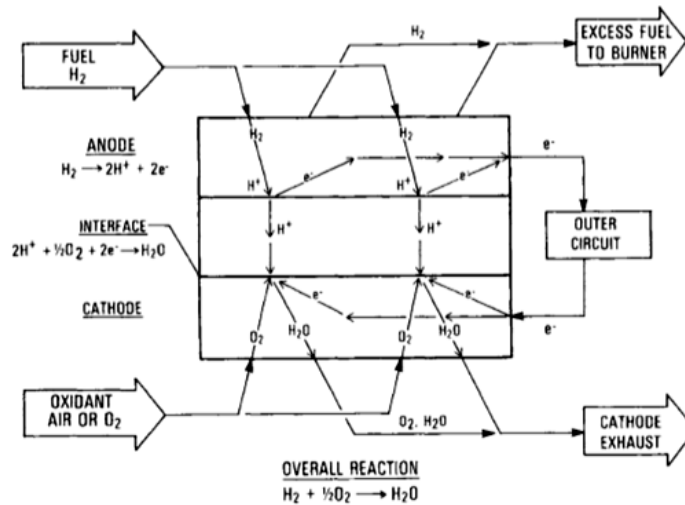


**Figure 2.12:** *Diagram of reactions in SOFCs based on proton-conduction* [14]*.*

### 2.2.5 SOFC stack design

A SOFC single cell consists of an oxide electrolyte sandwiched between an anode and a cathode. Practical SOFCs are not operated as single units; rather, they are connected in electrical series to build voltage. A series of cells is referred to as a stack, as it is presented in *Figure 2.13*, where different SOFCs stack designs are represented.

UNIVERSITAT POLITÈCNICA DE CATALUNYA
BARCELONA**TECH**
Escola d'Enginyeria de Barcelona Est
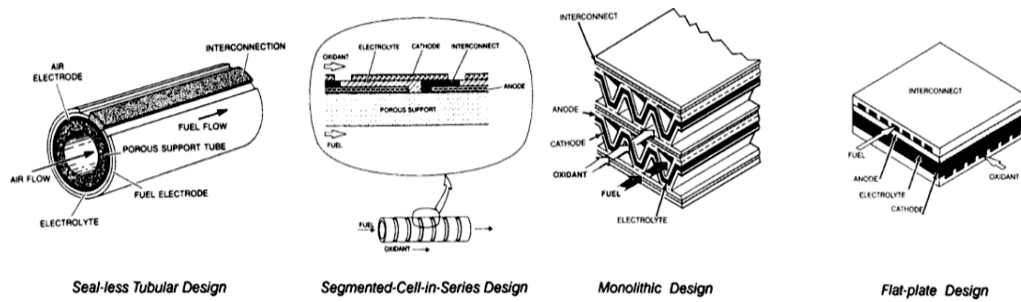
*Figure 2.31: Representation of different SOFCs stack designs* [14].

In general, the larger the surface area is the larger the power generated. However, like all power generating devices, to reduce losses and peripheral costs associated with large units, the smaller units are preferred. This usually translates into higher power density or higher efficiency.
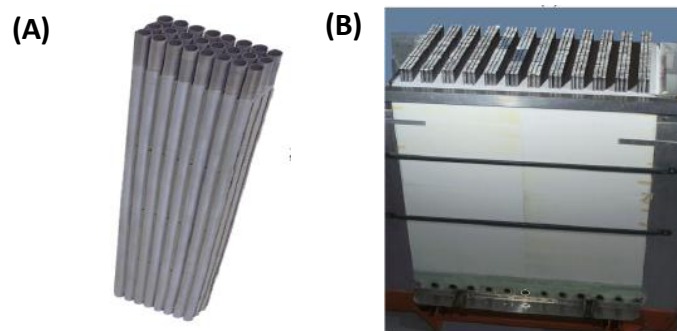
In a real stack, like the one showed in ***Figure 2.14.a***, each cell experiences different electrical, thermal and structural constraints due the neighbouring cells. The interaction between the cells in a stack is through these constraints. Since the bottom and top cells in the stack have only one neighbouring cell, they are different from the other cells in the stack, thus making it difficult to achieve uniformity among the cells. In addition, the inherent asymmetry in the fuel cell operation (different flows on fuel and air side) and inevitable differences in gas flow rates among the cells of the stack render uniform stack operation practically impossible. Thus the voltage and temperatures usually vary from cell to cell in a stack.

SOFC based power unit, several stacks are connected together to form a single module (see ***Figure 2.14.b***). As was in the case of cells in a stack, the stacks in a module also interact with each other through temperature, electric potential and mechanical stresses [15].



*Figure 2.14: a) 24 cell tubular SOFC stack and b) a tubular SOFC module with 48 stacks* [15].

UNIVERSITAT POLITÈCNICA DE CATALUNYA
BARCELONATECH
Escola d'Enginyeria de Barcelona Est

## 2.3   SOFCs materials

### 2.3.1 Electrolyte

In ***Table 2.1*** the needed requirements for an electrolyte are presented. The materials that can be used as electrolyte can be classified in two big groups depending on which ion is being conducted [13].

**Oxygen Ion Conducting**

These oxygen ion electrolyte materials can be classified into fluorite-based systems and perovskite-related intergrowth-structure systems. A general overview is going to be presented with some examples.

a. ***Fluorite-type:*** The fluorite type, generally written as AO2, is the crystal structure exhibited by a majority of conventional fast oxygen ion conducting materials, where A represents a tetravalent cation, as shown in ***Figure 2.15.a.*** The most used materials with this cubic fluorite structure are Zirconia ($ZrO_2$) doped to stabilize the desired phase and also doped-Ceria ($CeO_2$).

   Regarding to zirconia the high ionic conductivity comes from doping the A site apart from stabilizes the cubic structure but also increases the concentration of oxygen vacancies and thus introduces this high ionic conductivity. Some examples of these doping oxides are: calcium oxide (CaO), scandium oxide ($Sc_2O_3$) or yttrium oxide ($Y_2O_3$).

   If we talk about $CeO_2$, the oxygen vacancies are a result from the replacement of $Ce^{4+}$ with trivalent rare-earth ions. Typical systems are gadolinium-doped ceria (GDC) or samaria-doped ceria (SDC).

b. ***Perovskite-type:*** Many materials in the perovskite family, structure represented in ***Figure 2.15.b*** have been studied as electrolyte materials with high ionic conductivity at intermediated temperatures. Doped lanthanum gallate ($LaGaO_3$) is one of the widely studied perovskite-structured oxides that can be applied in intermediate-temperature SOFC. This material exhibited high ionic conductivity and long-term stability in both fuel and air environments in an intermediate-temperature range. However, it is difficult to synthesize a pure Lanthanum gallate strontium and magnesium doped (LSGM) phase. A majority of reports on LSGM demonstrates that it contains a few secondary phases which can reduce the conductivity.

   The simultaneous doping of Sr and Mg resulted in a reduction of the lean degree of $GaO_6$ octahedra and facilitated greater promotion of oxide ion conductivity compared with the

parent compound. Vacancies between oxygen sites along the $GaO_6$ octahedron edge cause the migration of oxide ions, as it is represented in **Figure 2.15.c.**
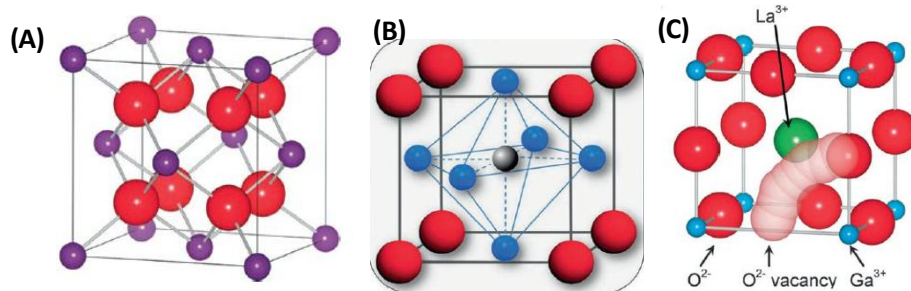


**Figure 2.15:** *a) Cubic fluorite structure. b) Perovskite crystal structure (ABO3). Red spheres represent A cations, the gray sphere represents the B cation, and blue spheres represent oxygen ions and c) Schematic presentation of the curved path for oxygen vacancy migration in the [Ga–O] plane of $LaGaO_3$ [13].*

**Proton Conducting**

Protonic conductors are desirable alternatives to oxygen ionic conductors when SOFCs are operated at intermediate temperatures, around 600$^o$C. The perovskite type, **Figure 2.15.b,** is the basic crystal structure of these materials. The cation in the *B* site with a valence of +4 is usually a transition metal or a rare-earth metal and presents a six-coordinated octahedron formation with itself in the center surrounded by its neighbouring oxygen ions. The *B* site used to be doped with trivalent elements, such as Ce, Zr, Y, In, Nd, Pr, Sm, Yb, Eu, and Gd.

$AB_{1-x}M_xO_{3-\delta}$ is treated as the common formula of the high-temperature proton-conducting perovskite-type oxides in which *M* is a trivalent dopant and $\delta$ represents the oxygen deficiency per unit cell. The introduction of *M* to the *B* site generates oxygen vacancies and thus proton conductivity. The incorporation of the mobile protons into the perovskite structure generates hydrogen defects in environments containing water vapor and hydrogen.

### 2.3.2 Cathode

In **Table 2.1** the main needed requirements for the cathode are presented. The materials that can be used for this part can be classified in two big groups depending on which ion is being conducted [13].

**Cathodes for Oxygen Ion-Conducting**

a. **Novel-Metal-Based:** Noble metals have long been applied as cathodes in SOFCs. However, their high price and low oxygen reduction activity at reduced temperatures make noble metals in the pure phase impractical for use as cathodes. Instead, the most studied noble-metal-based cathodes are composites created by mixing noble metals with a second ionic conductor. The formation of the composite creates better catalytic activity (due to the introduction of mixed conductivity into the electrode), a lower electrode cost, and an

UNIVERSITAT POLITÈCNICA DE CATALUNYA
BARCELONATECH
Escola d'Enginyeria de Barcelona Est

improved morphological stability. Among the noble metals, silver and platinum are the two most popular electronic conductors, and they also show good chemical compatibility with the selected ionic conductors.

The Ag and $Bi_2V_{0.9}Cu_{0.1}O_{5.35}$ (BVC) mixture is a well-known composite cathode due to its high electrocatalytic activity at reduced temperature and relatively low price compared with Pt.

b.  *Perovskite-Based:* The transport properties of perovskite-type oxides are dependent mainly on the *B*-site cations. Among them, Mn-based perovskites and Co/Fe-based perovskites are most frequently used for high-temperature (800-1000°C) and intermediate temperature (around 600°C) SOFCs.

   The lanthanum strontium manganite ($La_{1-x} Sr_xMnO_3$) perovskite materials are still the most popular material for cathodes in current commercialization-oriented SOFCs operating at temperatures usually higher than 850°C. This popularity is due to the good performance and structural stability of $La_{1-x}Sr_xMnO_3$ as well as the good chemical compatibility with the widely used zirconia-based electrolyte at high SOFC operating temperatures. However, the electrochemical activity was not satisfactory at intermediate temperatures; the introduction of a second ionic conducting phase is a simple and effective strategy to improve this chemical activity.

c.  *Layered Perovskite-Based:* A typical perovskite has a form like $ABO_3$. In layered perovskite the *A* cation or the *B* cation is duplicated. Depending on which cation is duplicated the oxygen vacancy is generated in a different way. It was proved that the oxygen transport in double perovskite occurred in a highly anisotropic direction and only in the A–O and adjacent B–O layers.

   *A*-site cation-ordered double perovskite oxides have the general formula $AA'B_2O_5$, where *A'* = Ba, *A* = Y or a trivalent lanthanide ion, and *B* is a first row transition metal ion. The cations tend to adopt an order due to the significant size difference between the two *A*-site cations. Moreover, the oxygen vacancies are primarily located in the rare-earth planes.

   In the $A_2B'B''O_6$ -type double perovskite structure, the arrangement of the *B*-cation sub-lattice is controlled primarily by the charge difference and secondarily by the size difference relative to a given *A* site.

d.  *Spinel Oxide:* The spinel structure is formulated $MM'_2X_4$, where *M* and *M'* are tetrahedral and octahedral coordinated metallic cations, respectively, and *X* is an anion (typically Oxygen). Compared with the traditional perovskite oxides, spinel oxides as the electrodes do not react with neighbour layers to yield high resistance phases, because the spinel oxides do not consist of rare-earth or alkaline-earth elements. Therefore, the chemical capability is good between the spinel electrode and its neighbour layers. The electric conductivities of some spinel oxides are up to dozens of Siemens per centimetre in the operation temperature range of intermediate-temperature SOFCs.

UNIVERSITAT POLITÈCNICA DE CATALUNYA
BARCELONATECH
Escola d'Enginyeria de Barcelona Est

One of the most used Spinel Oxide is the one doped with Mn, Co, Cu. In this type of materials show a phase transition from tetragonal (*t-*) to cubic (*c-*) phase when the doping amount of the metal element increases. Their electric conductivities increase with the metal content. Furthermore, they are good catalysts towards oxygen reduction reactions [16].

e. **Doped Ceria:** The flexible thermal reduction of $Ce^{x+}$ at high temperature can deliver improved electronic conductivity, and the doped ceria might potentially display mixed ionic conductivity. Selected elements with variable valence states have been doped into ceria. Praseodymium (Pr) with mixed trivalent and tetravalent states could simultaneously increase the oxygen vacancies and the electronic conductivity of ceria.

Depending on the Pr percentage and using the appropriate ion doping, Pr-doped ceria could be used as an oxygen reduction electrode in SOFCs. For example, an improved total conductivity (most likely due to enhanced electronic conductivity) was obtained by adding 2 mol. % $CoO_x$ into a $Ce_{0.9}Pr_{0.1}O_{2-\delta}$ phase. It was concluded that the Co species acted as a sintering aid that increased the grain size and also acted as a reduction promoter that increased the proportion of $Pr^{3+}$ versus $Pr^{4+}$ at high oxygen partial pressure.

**Cathodes for Proton-Conducting**

a. **Perovskite-Based Cathodes:** The BSCF material, which was proved to possess superior oxygen reduction activity for SOFCs based on an oxygen ion-conducting electrolyte, was also applied as a cathode for the proton-conducting for $BaCe_{0.9}Y_{0.1}O_{2.95}$ -electrolyte-based fuel cell. The results showed that obvious phase interactions occurred, because Ba was able to diffuse from the electrolyte to the cathode. Such phase interactions increased the ohmic resistance of the cell. With the oxygen ion-conducting material as the cathode, the active sites for oxygen reduction are most likely limited to the interface between the proton-conducting electrolyte and cathode. As a result, the electrode performances are inferior to those on an oxygen ion-conducting electrolyte and are inadequate for practical applications.

To improve that try to introduce a proton-conducting phase into the electrode can be done by the development of mixed conducting materials with intrinsic proton/electron/oxygen ion conducting ability is an alternative approach. The material exploration is also primarily based on the $BaCeO_3$ matrix.

b. **Layered Oxides:** Two structures of layered oxides can be presented to be applied as cathode for protonic conduction.

The first one is the Double Perovskite Material like $GdBaCo_2O_5$, $SmBaCo_2O_5$ or $PrBaCo_2O_5$, where the amount of oxygen vacancies was the most influential parameter that determined the oxygen reduction reaction activity of the compounds. Because of that the oxygen vacancies allow the hydration of them and the formation of protonic defects, which induce protonic diffusivity.

UNIVERSITAT POLITÈCNICA DE CATALUNYA
BARCELONATECH
UPC  Escola d'Enginyeria de Barcelona Est

Exist another type Cathode which is based on rare earth with a metal oxide. Among the $LnNi_2O_4$ (*Ln* = La, Pr, Nd) series, $Pr_2NiO_4$ showed the highest activity for the proton-conducting electrolytes. Moreover, the polarization resistance was reduced by introducing water into air. This result revealed that the $Pr_2NiO_4$ material also possessed good proton-conducting ability because the low-frequency resistance mainly reflected the oxygen dissociation and water formation processes.

### 2.3.3 Anode

In *Table 2.1* the needed requirements for anode are presented. The materials that can be employed in this part can be classified in two big groups; if the anode is a nickel-based cermet or if the materials are exclusively oxides [13].

**Nickel-Based Cermet**

In the cermet anode, nickel (Ni) creates an electronic conduction path and catalytic activity for the electrochemical and chemical oxidation of fuels, and the ceramic part offers a thermal expansion match with the ceramic electrolyte as well as an ionic conduction path to extend the reaction zone in the anode.

Ni-based cermet materials meet **most of the requirements** for a SOFC anode, such as high electronic conductivity, high ionic conductivity, low cost, high stability at high operating temperatures and in reducing atmospheres, good thermal and chemical compatibility, and high activity for $H_2$ electrochemical oxidation.

The **disadvantages** of these Ni-based materials are poor redox stability, poor sulphur tolerance, and poor coking resistance when operated under sulphur-containing hydrocarbon fuels. Another issue is Ni particle agglomeration after long-term operation, which leads to insufficient catalytic activity for fuel reforming at intermediate.

**Oxide Anodes**

Compared with a metallic Ni catalyst, oxide catalysts show much higher coking resistance due to their different electronic structures. In addition, many oxide materials also show much higher redox stability than Ni. Poor electronic conductivity under a reducing atmosphere and relatively poor catalytic and electrocatalytic activity for hydrocarbon oxidation at reduced temperatures are a few of the major limitations of oxide anodes.

a. ***Fluorite-type Ceria-Based Oxides:*** $CeO_2$ with high oxygen storage capability can be partially reduced in a fuel atmosphere to introduce oxygen vacancies and provide the $Ce^{4+}/Ce^{3+}$

UNIVERSITAT POLITÈCNICA DE CATALUNYA
BARCELONATECH
Escola d'Enginyeria de Barcelona Est

redox couple. In addition, doping of ceria with certain other mixed-valence transition elements can introduce additional redox couples and oxygen vacancies that are beneficial for electrochemical fuel oxidation, making them potential anode materials for SOFCs.

One typical structure is $Ce_{0.8}M_{0.2}O_{2-\delta}$ where *M* are metals like: Mn, Fe, Ni, Cu.

b. ***Perovskite Oxides:*** Compared with fluorite oxides, perovskite-type $ABO_3$-based oxides are much more widely investigated as anodes of SOFCs. Perovskite oxides are a large family of oxides with the same phase structure and have been widely used as cathode. Due to their versatility in material composition, a wide range of properties can be created using tailored *A*- and *B*-site cations in perovskite.

In general, the specific constraints for the development of perovskite anodes are listed as follows. First, the *B*-site element can only be partially reduced to ensure electronic conductivity. Second, the active redox couple should have a strong ability for dissociation of the fuel on the anode surface. Third, sufficient catalytic activity is required to release the oxidized products from the surface. Fourth, sufficient oxygen vacancies for oxygen ion conduction must not be ordered. Because the anodes are operated in a reduced atmosphere, the *B*-site cations should have a stable oxidation state to avoid deep reduction, which could cause collapse of the perovskite lattice structure. Therefore, most perovskite anode materials contain Cr, V, and Ti as the main cations in their *B* sites.

## 2.4 State of the art

On this Master's project the following topics will be covered; particle size analysis of the feedstock as well as modification of each used material (Y-$ZrO_2$, Lanthanum gallate strontium and magnesium doped (LSM), Gadolinium III used as electrolyte, cathode and anode respectively*).* Then try to control de porosity of each part, because it represents a key parameter, by means of feedstock modification. Finally, the idea is tried to evaluate the microstructural and mechanical properties of each part with the optimized particle size and feedstock composition. All of these small goals will represent small pieces to complete the main topic of all the work done along this Master's project: ***The generation of a SOFC by means of AM methodology.***

Making some research about the topics the last 20 years some interesting trends are observed as depicted in ***Figure 2.16***, which represents the amount of articles published during this period talking about the main topics of this Master's project. In ***Figure 2.16.a*** the represented trend is about SOFC articles, we can see that the research of SOFC in the last 20 years presents a significantly increase during the first 10 years, that it can be explain with by the desire to find alternative energy sources, after 2010 the research on this topic was stabilized. On the other hand, in ***Figure 2.16.b*** the evolution of the AM publications is shown, in this case an exponential increase of publications related about this topic is observed. This trend is typical of hot topics, which it means that the investment during

these last 7 or 8 years has considerably grown. Finally, in **Figure 2.16.c** we can see the publications talking about SOFC produced by any AM technique. In total we have found less than 20 publications combining these two topics, which it means that for us represents a good opportunity to develop some research about this field.
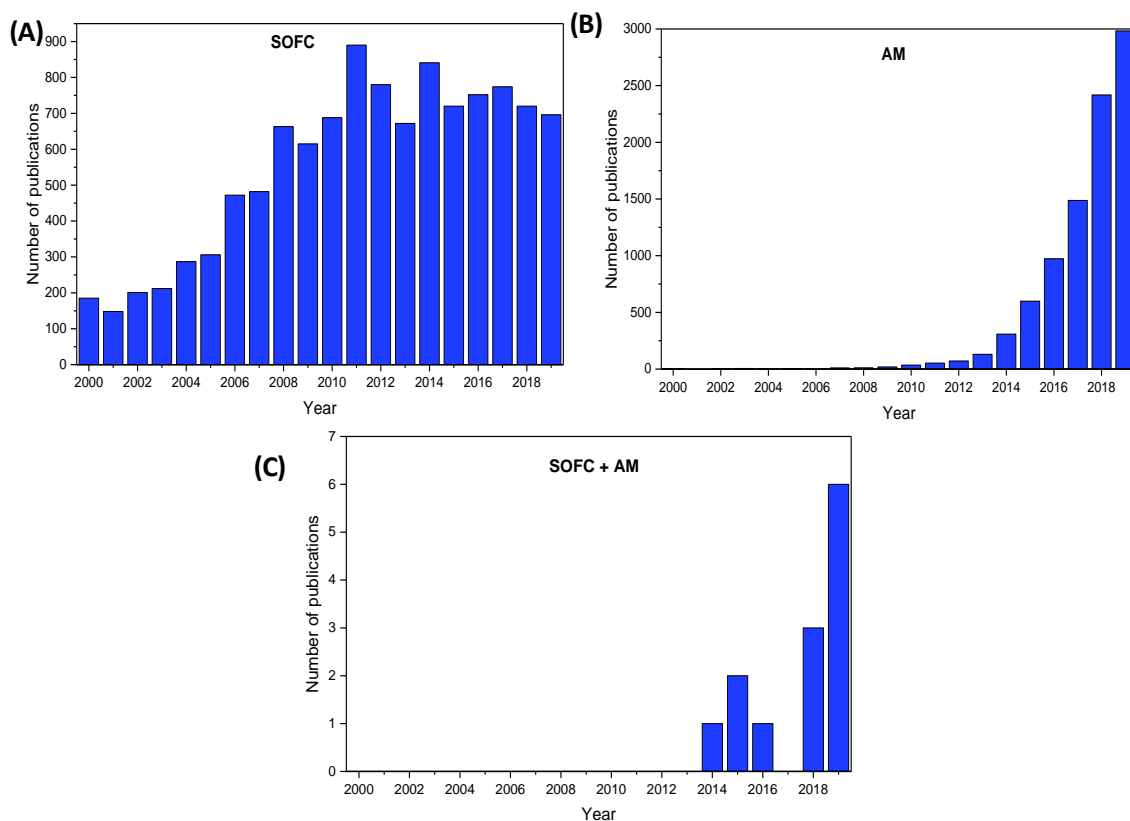


*Figure 2.16: Histogram representation as a function of the publication years for the following topics: a) SOFC, b) AM and c) SOFC produced by AM.*

In this section some examples of articles covering some of these topics are presented. It is important to remark that exist scarce information about SOFC produced by AM technology, as it is shown in *figure 2.16.c*. But here we only try to show some papers about each used material during this Master's project, in the corresponding part, as well as some mechanical characterization of SOFC produced by traditional manufacturing routes. Only the last two referenced article talks about the production of an electrolyte by means of the AM technique.

**M. Morales, J. J. Roa, J. M. Perez-Falcón, A. Moure, J. Tartaj, F. Espiell, M. Segarra, *Correlation between electrical and mechanical properties in $La_{1-x}Sr_xGa_{1-y}Mg_yO_{3-\delta}$ ceramics used as electrolytes for solid oxide fuel cells,* Journal of Power Sources, vol. 246, pp. 918-925, 2014.**

On this paper a correlation between mechanical and electrical properties of electrolytes for SOFCs has been done. The material used to produce the electrolyte in this case was Sr and Mg doped

UNIVERSITAT POLITÈCNICA DE CATALUNYA
BARCELONA**TECH**
Escola d'Enginyeria de Barcelona Est

LaGaO$_3$ ceramic. In the paper they get the samples to analyse by isostatic pressing followed by a sintering process applying temperatures between 1300 and 1450 $^oC$.

This paper will be so useful because they found a clear relation between hardness and ion conductivity. Both properties, mechanical and electrical, are strongly controlled by the electrolyte microstructure like the relative density. So it would be so interesting if this kind of relation remains stable with 8Y-TZP.

**M. Morales, J. J. Roa, J. Tartaj, M. Segarra,** *A review of doped lanthanum gallates as electrolytes for intermediate temperature solid oxides fuel cells: From materials processing to electrical and thermo-mechanical properties.* **Journal of the European Ceramic Society, vol. 36, pp.1-16, 2016.**

On this paper a review of SrO- and MgO-doped lanthanum gallates (LSGMs), focused on the implementation as electrolyte for SOFCs at intermediate temperature, is done. The manufacturing design, the sintering routes to lower the sintering temperatures, a chemical compatibility between electrolyte and electrodes and a study of mechanical and thermal properties, are the topics that have been covered along this review paper.

They found that with the following routes they can fabricate different cell designs without the formation of secondary phases during sintering process. Is known that the use of interlayers between electrolyte and electrode/s increases both the complexity of cell manufacturing and the electrolyte thickness, so they get the highest performances of cells have been achieved with La-doped ceria (LDC) interlayers. The LDC interlayers act as effective barrier layers to the inter-diffusion of La and Ni between the electrolyte and anode.

Finally, this paper will be useful because a mechanical characterisation of LSGM is done, giving Hardness and Elastic modulus values.

**D. P. Tarragó, B. Moreno, E. Chinarro, C. Malfatti, V. Caldas de Sousa,** *Deposition of nanostructured LSM perovskite thin film on dense YSZ substrate by airbushed solution combustion (ASC) for application in SOFC cathodes***, International Journal of Hydrogen Energy, vol. 45, pp. 11749-11760, 2020.**

On this paper the airbrushed solution combustion (ASC) method was used to fabricate an LSM thin film on a dense YSZ substrate. The aim to apply this new technique is to produce a single phase LSM perovskite with very thin and interconnected porosity, with the idea to make SOFC high efficiency energy generation devices. For that thin ceramic films are proposed as their main components. The rate of the oxygen reduction reaction is relevant for the overall performance of the SOFC, hence a lot of attention is given to the cathodes and their interfaces.

UNIVERSITAT POLITÈCNICA DE CATALUNYA
BARCELONATECH
Escola d'Enginyeria de Barcelona Est

In this article they use the same materials for the electrolyte and the cathode as the ones that are going to be used during this Master's project. They show the enhanced morphological structure obtained by this new processing technique, ASC. The benefits of have an orthorhombic perovskite LSM are an interconnected porosity and nanometric grain size which would lead to improvements in the SOFC performance. So for our project would be interesting try to copy this morphology.

**L. O. O. De Costa, A. M. da Silva, F. B. Noronha, L. V. Mattos,** *The study of the performance of Ni supported on gadolinium doped ceria SOFC anode on the steam reforming of etanol*, **International Journal of Hydrogen Energy, vol. 37, pp. 5930-5939, 2012.**

On this paper the catalytic performance of Ni/CeGd SOFC anodes prepared by co-precipitation for steam reforming of ethanol at different reaction temperatures was evaluated. The SOFC anode calcined at 1073 K exhibited the highest activity and the lowest by-products formation rates during steam reforming (SR) at 773 K, it was associated with the formation of carbon filaments. It was also observed that the increase of reaction temperature from 773 to 1073 K decreased coke formation, which was no longer detected at 1073 K. This result was attributed to the reverse of the Boudouard reaction and the promoting effect of the support on carbon gasification. So as a conclusion Ni/CeGd composite is a promising material to be used as an anode in SOFC systems running directly on ethanol. It exhibited the highest stability and the lowest rate of by-products formation during SR at 773 K.

It will be useful for our project to explain the need of use Ceria with Gd, and the typicall performing values of this anode material in a SOFC.

**J. J. Roa, J. C. Ruiz-Morales, J. Canales-Vásquez, M. Morales, X. G. Capdevila, P. Nuñez, M. Segarra,** *Mechanical Characterisation at Nanometric Scale of a New Design of SOFCs*, **Fuel Cells, vol. 11, 2011.**

In this experimental work, the mechanical properties (hardness, *H* and Young's modulus, *E*) at different applied loads have been studied using the nanoindentation technique and the equivalent indenter method. On the other hand, the different fracture mechanisms have been determined using atomic force microscopy (AFM), observing the plastic behaviour that takes place during the indentation process. The final results were the following; *H* value for YSZ (20-21 GPa) is higher than that for NiO-YSZ (6-7 GPa), while *E* values for YSZ and NiO-YSZ are 260 ± 15 and 205 ± 20 GPa, respectively. Talking about fracture mechanism; only YSZ samples present several radial cracks at the corners nucleated by sharp indentation, thus indicating that H values have been underestimated.

UNIVERSITAT POLITÈCNICA DE CATALUNYA
BARCELONATECH
Escola d'Enginyeria de Barcelona Est

This Master's project will cover a part of mechanical properties and fracture mechanism for each printed part, so this experimental work will be useful for the nanoindentation conditions to apply as well as the YSZ results will give us an idea of experimental values to compare with.

**J. Wei, T. Osipova, J. Malzbender, M. Krüger¸** *Mechanical characterization of SOFC/SOEC cells*, **Ceramics International, vol. 44, pp. 11094-11100, 2018.**

This paper provides parameters for determination of failure probability and lifetime prediction of a commercial SOFC and commercial SOEC supported on the anode substrate. So a mechanical characterization is performed for cells in oxidized and reduced state. In particular, fracture strength, elastic modulus and residual stress for half-cells were assessed. With respect to fracture strength, also subcritical crack growth at different temperatures has been analyzed, being the basis of a derived strength-probability-time plot.

The studied half-cells were based on 8Y-TZP, so the mechanical results will be useful to know the behaviour of a commercial SOFC, and try to compare some of the mechanical features with the manufactured samples for this Master's project.

**G. Lin, O. Kwon, Y. Narendar (2012),** *Solid Oxide Fuel Cell interconnects including a ceramic interconnect material and partially stabilized zirconia,* **European patent. No. EP 2 795 708 B1.**

This patent claims different fabrication process to produce interlayers part of a multi-stack SOFC. Usually a planar SOFC is not presented as a layer of anode material, cathode material and electrolyte. The typical configuration is a multilayered stacking of; anode, electrolyte and cathode, multiple times.

This patent presents the fabrication process of two different configurations of SOFC produce of ceramic based materials, typically 8Y-TZP among others. So this work will be useful to know the situation of SOFC in the industry as well as the ceramic used materials for each part.

**S. Masciandaro, M. Torrell, P. Leone, A. Tarancón,** *Three-dimensional printed yttria-stabilized zirconia self-supported electrolytes for solid oxide fuel cell applications,* **Journal of the European Ceramic Society vol. 39, pp. 9-16, 2019.**

On this article a specific AM technique has been applied, stereolithography, to get the electrolyte. They printed cells with honeycomb geometries, using 3Y-TZP as a ceramic material for the electrolyte. After that cells were fabricated and completed with cathode and anode layers of LSM- and Ni-YSZ composites, respectively, were electrochemical characterized showing full functionality. In addition, more complex configurations of the electrolyte have been printed yielding an increase of the performance entirely based on geometrical aspects.

UNIVERSITAT POLITÈCNICA DE CATALUNYA
BARCELONATECH
UPC    Escola d'Enginyeria de Barcelona Est

Basically, this paper has a main goal similar to the long term goal presented for this Master's project, the fabrication of a SOFC using an AM technique. It will give us some electrochemical values for the future. But for this Master's project it gives us the certainty that the combination of both techniques has future, as well as some information about materials and processing parameters although the AM techniques are different.

**L. Wei, J. Zhang, F. Yu, W. Zhang, X. Meng, N. Yang, S. Liu,** *A novel fabrication of yttria-stabilized-zirconia dense electrolyte for solid oxide fuel cells by 3D printing technique,* **International Journal of Hydrogen Energy, vol. 44, pp. 6182-6191, 2019.**

This work is focusing on dense 8 mol.% yttria-stabilized-zirconia (8YSZ) electrolyte fabrication via digital light processing (DLP)-Stereolithography-based 3D printing technique. Multiple 8YSZ electrolyte green bodies are printed, together with an optimized debinding and sintering procedure, the 8YSZ green body changes into a dense electrolyte. The symmetric cell fabricated of silver-$Ce_{0.8}Gd_{0.2}O_{1.9}$ (Ag-GDC) as cathode/anode with the dense 8YSZ electrolyte. Some tests were done to study the electrochemical performance, giving good results. Such success will encourage the application of 3D printing technology for one step direct fabrication of the complex-shaped SOFC stack overcoming the conventional time-consuming procedure.

# 3. Goal

This Master's work fits in a bigger project where the **long term goal** is to be able to develop a systematic protocol to print solid oxide fuel cells (SOFC) with complex shapes with at least the same microstructural and mechanical properties as for the manufactured SOFC by the conventional processing routes. So this work will represent the next natural step of my final Master's project.

If we focus on this study, it is divided in <u>four different parts:</u>

    (i)   To analysis of the powder size, an optimisation of it to be able to reduce the nozzle size.

    (ii)   To study of different compositions of Pluronic F-127® and ceramic inks with the aim to be able to control the final porosity, and find the optimal feedstock composition for each part.

    (iii)   To study the rheological properties of optimal feedstocks.

    (iv)   Evaluation of the microstructural and mechanical properties of printed samples using the optimal ceramic inks.

In general terms, the ***main scope of this Master's project*** is ***to improve the resolution of the SOFC, and determine the best composition for each part to achieve the specific porosity, by optimizing the powder and the composition of feedstocks***.

To try to understand better from these goals come, in ***Figure 3.1*** is shown all the features that we found that is important to control during an AM process to fabricate a SOFC. In this schematic representation we just mark all the features studied during my Bachelor's project and previous works before this Master's project. Also, we remark the work that is needed to do during this Master's project and finally some future work after to achieve the goals of this presented project.
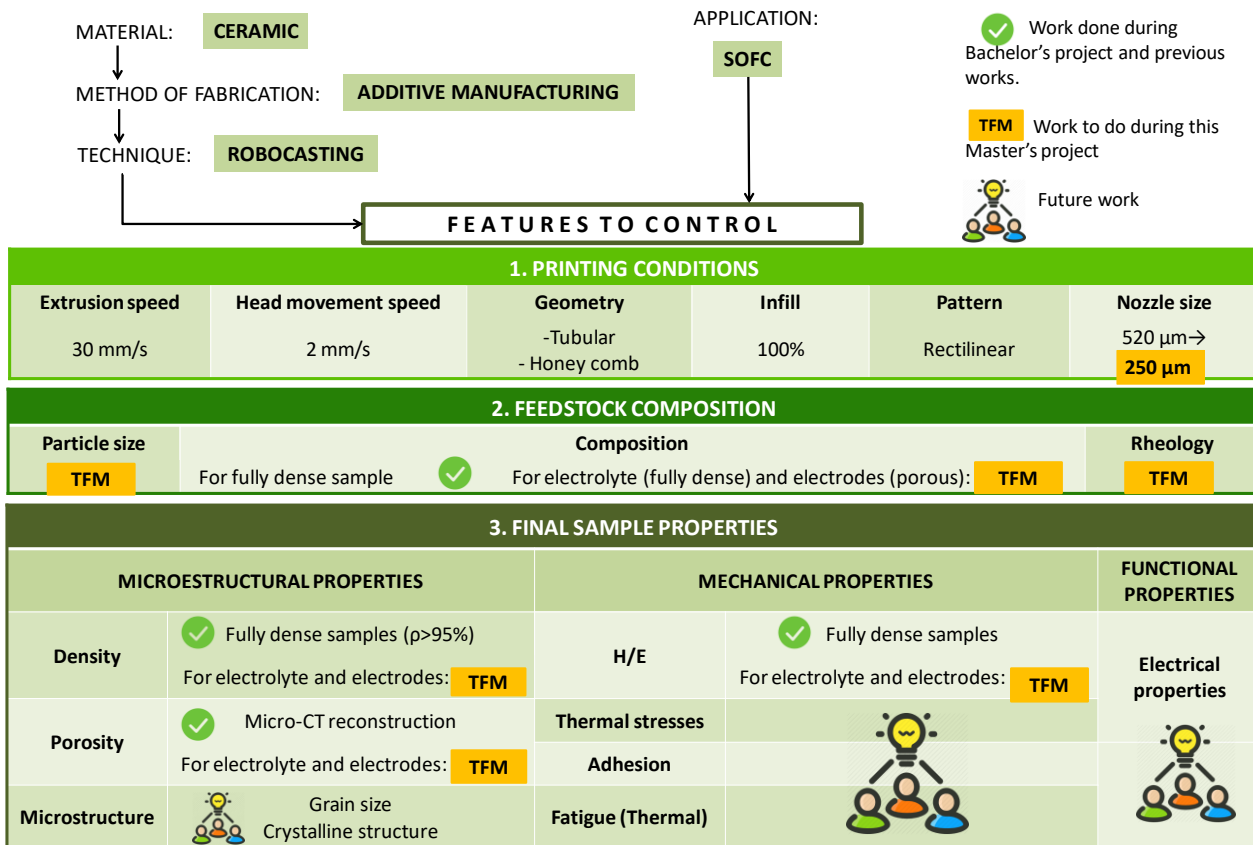
MATERIAL: **CERAMIC**

↓

METHOD OF FABRICATION: **ADDITIVE MANUFACTURING**

↓

TECHNIQUE: **ROBOCASTING**

APPLICATION:

**SOFC**

✓ Work done during Bachelor's project and previous works.

**TFM** Work to do during this Master's project

Future work

**F E A T U R E S   T O   C O N T R O L**

| 1. PRINTING CONDITIONS | | | | | |
|---|---|---|---|---|---|
| **Extrusion speed** | **Head movement speed** | **Geometry** | **Infill** | **Pattern** | **Nozzle size** |
| 30 mm/s | 2 mm/s | -Tubular<br>- Honey comb | 100% | Rectilinear | 520 µm → **250 µm** |

| 2. FEEDSTOCK COMPOSITION | | | |
|---|---|---|---|
| **Particle size**<br>**TFM** | **Composition** | | **Rheology**<br>**TFM** |
| | For fully dense sample ✓ | For electrolyte (fully dense) and electrodes (porous): **TFM** | |

| 3. FINAL SAMPLE PROPERTIES | | | | |
|---|---|---|---|---|
| **MICROESTRUCTURAL PROPERTIES** | | **MECHANICAL PROPERTIES** | | **FUNCTIONAL PROPERTIES** |
| **Density** | ✓ Fully dense samples (ρ>95%)<br>For electrolyte and electrodes: **TFM** | **H/E** | ✓ Fully dense samples<br>For electrolyte and electrodes: **TFM** | **Electrical properties** |
| **Porosity** | ✓ Micro-CT reconstruction<br>For electrolyte and electrodes: **TFM** | **Thermal stresses** | | |
| | | **Adhesion** | | |
| **Microstructure** | Grain size<br>Crystalline structure | **Fatigue (Thermal)** | | |

***Figure 3.1:*** *Schematic representation of all the features to control during AM process to fabricate SOFC.*

34

UNIVERSITAT POLITÈCNICA DE CATALUNYA
BARCELONA**TECH**
UPC
Escola d'Enginyeria de Barcelona Est

# 4. Experimental procedure

## 4.1 Materials

On this part the two principal materials employed to produce the ceramic inks will be explained. Polymeric matrix which act as a gelling agent (Pluronic F-127® from *Sigma Aldrich)*, and the ceramic particles zirconia stabilized with yttria; 8% molar, 8Y-TZP from *TOSOH; the datasheet for each material is available in **Annexes A.1** and **A.2**, respectively.* The main information for each material is briefly described below in detail:

### a. Polymeric matrix: Pluronic F-127®

The Pluronic F-127® from *Sigma Aldrich*, the datasheet is available in **Annexe A.1**, is a copolymer used to do hydrogels, basically for medical applications.

Pluronics F-127® [17] are amphylic copolymers comprised of two external blocks of polyethylene oxide (PEO) and a central block of polypropylene oxide (PPO), comprising a global formula (PEO-PPO-PEO) as it is shown in **Figure 4.1**. These copolymers present a thermal inverse mechanical behaviour in aqueous dissolution due to the gelling process that they suffer with the temperature; in particular when the temperature increases. This behaviour is manly originated by the difference in the critical dissolution temperature. The gelling temperature and mechanical strength of the gel depends on the concentration of polymer and the chain length of PEO and PPO.
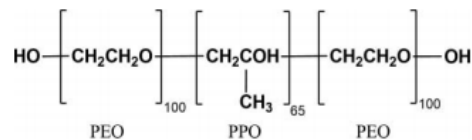


**Figure 4.1:** *Structural formula of Pluronic F127® block copolymer, where PEO and PPO means Polyethylene oxide and Polypropylene oxide, respectively* [18]*.*

The behaviour of these solutions is complex, since they exhibit a liquid behaviour below the sol-gel transition temperature, which varies with the percentage of Pluronic F-127® powder as it is shown in **Figure 4.2**, while at temperatures equal to or above this transition, their shear/viscosity module ratio undergoes an increase of several orders of magnitude in a very narrow temperature range. This nature favours its use for the Robocasting process [19]. On the other hand, in order to increase the efficiency of this gelling material, a good dispersion and homogenisation of the samples in the liquid state is required in order to obtain a stable paste suitable for the printed process.
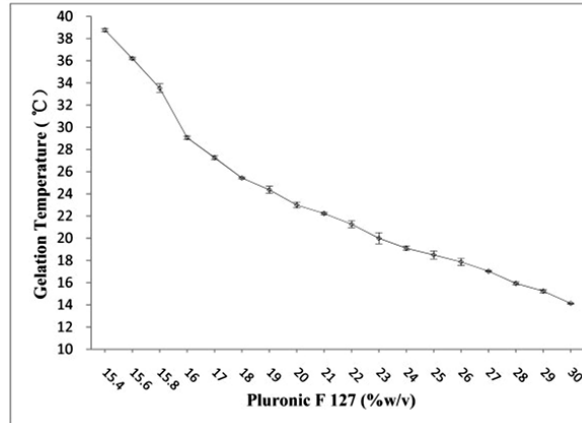
*Figure 4.2: Gelation temperature and thermoreversible behavior of Pluronic F-127® gel* [17].

## b. Ceramic Charge for the electrolyte:

On this Master's project the material used for the electrolyte part was zirconium oxide ($ZrO_2$). This is commonly known as zircona, it is a material with a long history of application in various industrial sectors. The wide variety of uses of this material ranges from its application as an abrasive material when its purity is limited, to its use in structural elements in highly aggressive processes due to its relevant toughness and resistance to wear. Recently, this ceramic material has been widely employed as a biomaterial due to its chemical nature, inertness, etc.

This ceramic material presents three allotropic phases, as it is depicted in **Figure 4.3**. The monoclinic (*m-*) phase is stable at room temperature till 1170 °C, between 1170 and 2370 °C the stable phase is the tetragonal (*t-*), and above 2370 °C the stable phase is cubic (*c-*). The transformation from tetragonal to monoclinic phase ($t \rightarrow m$) is a martensitic transformation and is accompanied by a volume variation of around 4-5%, if unconstrained. Upon cooling the volume expansion may lead to severe cracking of the material, compromising the integrity and causing premature failure [20]. However, this situation can be reversed by the use of stabilizing oxides such as magnesia (MgO), calcium (CaO), ceria ($CeO_2$) or yttrium ($Y_2O_3$), which allow the stabilization of high temperature phases at room temperature.
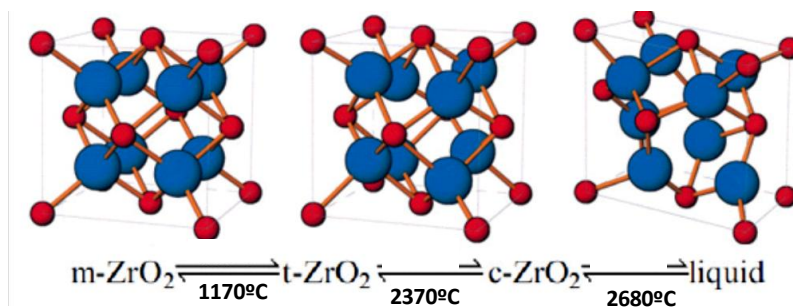


*Figure 4.3: Crystalline structures of zirconium oxide and their transition temperatures* [21]*.*

During this Master's project the used zirconia will present as stabilizing oxide, Yttrium. This ceramic is called; yttria stabilized tetragonal zirconia polycrystalline (Y-TZP). It has been regarded as a potential structural material. The unique combination of high strength (700–1200MPa), fracture toughness (2–10MPa·m$^{1/2}$) and chemical inertness makes them indispensable for many applications. The high toughness of Y-TZP ceramics is attributed to stress induced martensitic transformation in the stress field of propagating cracks, a phenomenon popularly known as *'Transformation Toughening', Figure 4.4* shows a schematic representation of this mechanism [22].
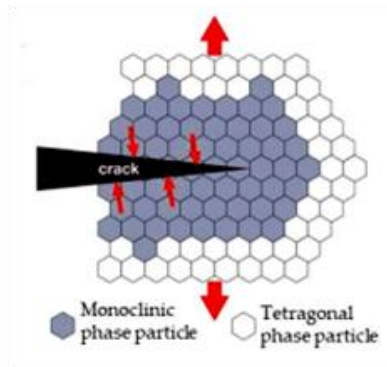


*Figure 4.4: Schematic representation of Transformation toughening phenomenon* [23]*.*

Specifically, during this work, the used Y-TZP will present an 8% molar of Yttrium. This 8Y-TZP will be supplied from Tosoh, ***Annex A.2.***

The reason to use this ceramic as electrolyte material, can be explained for two reasons. As it was explained in ***section 2.2.1***, a good ionic conductor is needed for this SOFC part. 8Y-TZP from the typically used 3Y-TZP, presents an increase in the stabilizing oxide content and interconnected presence of the *c*-phase result in a significant increase in the activation energy of bulk conductivity. The presented dependences of the energy on the chemical composition of the material are in good agreement with the model description of ionic conductivity in compounds with fluorite structure [24]. So due to 8Y-TZP presents this *c*-phase that is presented as fluorite structure can explain this good ionic conductivity.

**c.   Ceramic load for the cathode:**

The used material for the cathode will be Lanthanum gallate doped strontium and magnesium (LSM). It is considered as an exotic material due to it is form of rare earth metals basis and for this project LSM will be used mixed with 8Y-TZP to increase the electrochemical reaction site.

This material could have different stoichiometric relation; in general, the chemical composition is presented on the following way: $La_{1-x}Sr_xGa_{1-y}Mg_yO_{3-\delta}$. And with the variation of *x, y and δ,*

different types of LSM are produced depending on the desired application. The LSM used during this Master's project has a *x = 0.2; y = 0.2; δ = 0*, so the final composition is the following: $La_{0.8}Sr_{0.2}Ga_{0.8}Mg_{0.2}O_3$. The LSM used is from *Sigma-Aldrich,* the data sheet is available in **Annex A.3.**

The cathode material needs to be a good electronic conductor among other requirements, as explained in **section 2.2.1.** Here bellow we are going to try to explain why LSM is the proper materials.

The electronic conductivity of (Ln, RE)MO$_3$ (*RE* and *M* are rare earth ions and transition metal ions, respectively) perovskite is mainly dependent on the *B*-site cation. Among the third period transition metals, Mn, Co, and Fe are investigated for cathodes. Manganese-based perovskites are widely recognized as the materials best suited for the cathode of a high-temperature SOFC that uses a zirconia-based electrolyte and operates at temperatures higher than 800$^0$C. In the case studied, (La, Sr)MnO$_3$ (LSM) is the chosen one. Because over the other transition metal perovskites is the one that presents compatibility with a YSZ-based electrolyte. The thermal expansion coefficient matches well, and moreover it can make a stable interface with YSZ [25]. So, because of this morphological situation and it perovskite structure, LSM is the chosen material.

### d. Ceramic load for the anode:

For the anode the idea was used Gadolinium III (Gd). It is a lanthanide element as well as lanthanum, so Gd it is also considered a rare an exotic earth metal. It potential is under study so there is scare information about functional SOFC using this element as anode. Nevertheless, it is known that Gadolinium needs to be doped with Ceria for energetic applications. Usually this Gadolinium doped Ceria is combined with Ni or Cu and YSZ, to improve the affinity between electrolyte and anode and improve the electronic conductivity.

Gadolinium doped Ceria is a good candidate to be used as an anode because cubic fluorite-structured cerium oxide is formed using this type of material. It plays a major role in reducing the operational temperature of SOFC. Cermet anodes behave like mixtures of electronic and ionic conductors as the $Ce^{4+}$ phase is reduced to the $Ce^{3+}$ phase in a reduced atmosphere. This reduction results in an irreversible formation of oxygen ion vacancy and the migration of ions, which are associated with the transformation of $CeO_2$ into $Ce_2O_3$. These $CeO_2$-based materials exhibit excellent catalytic activities [26]. The added metallic element like, Ni or Cu, is the one that is going to improve the electronic conductivity.

UNIVERSITAT POLITÈCNICA DE CATALUNYA
BARCELONA**TECH**
Escola d'Enginyeria de Barcelona Est

During this Master's project Gadolinium presents some problems during sintering process because we try to print and sinter it without add Ceria. Due to the lack of time we were not able to process the new powder with Ceria and 8Y-TZP to solve this problem. Due to that Gadolinium would only be studied in the first part of this project; the study of the ceramic powder to reduce the particle size with the aim to improve the resolution of the printed samples, and the study of rheological properties of the optimal feedstock.

## 4.2    Powder processing

One of the most important goals for this Master's project is the step to process the powder that comprise two parts; the first to prepare the mix between the electrode material, LSGM for the cathode and Gd for the anode, with zirconia. The second part comprises the step to reduce particle size by using a sieve.

Two ways to prepare mix powders can be considered; one mechanical way through mechanical milling or the chemical way, the one used for this Master's project.

This process starts preparing ethanol dissolution with the ceramic powder and mill-balls of Alumina, with a size of 2.5 μm. 50g of ceramic powder, in the case of the mixed powder for electrode parts 60% on weight (wt. %) of the electrode material and 40 wt. % of 8Y-TZP [27] were blended, with 200g of mill-balls were prepared adding ethanol in the mixing container until it is completely full. This mixture is shaken during 24h in a Turbula®, ***Figure 4.5***.



***Figure 4.5:*** *Image of Turbula® machine used during this Master's project.*

After this 24h, the mixture was poured through a Büchner funnel, ***Figure 4.6.a***, to separate the mill-balls and deposit the dissolution in a round-bottom flask. This flask was used to put the mixture in a machine called steam rotavapor, ***Figure 4.6.b***.

UNIVERSITAT POLITÈCNICA DE CATALUNYA
BARCELONA**TECH**
Escola d'Enginyeria de Barcelona Est

The rotavapor applies vacuum to the flask and heat the mixture through a heating bath that heats up 60 °C, with that ethanol is evaporated and we are able to separate it from the ceramic powder. The evaporated ethanol can be retrieved and reuse to clean.

As a final step, the ceramic powder separated from ethanol is deposited in a crucible and put in a stove, *Figure 4.6.c*, at 90 °C for 48 hours. This last step is done to make sure that all the ethanol is eliminated, and the powder is enough dried to do not generate agglomerations.



*Figure 4.6: a) Büchner funnel to detach the alumina mill-balls from the mixture, b) steam rotavapor used to separate the ethanol from the ceramic powder and c) stove to dry the final mixture powder.*

The second part comprises the sieve step. When the powder is dried, it is grinded up with a mortar and a pestle of agate, *Figure 4.7.a*. After that we introduce the mixture in the sieve machine, *Figure 4.7.b*. Three different sieve were applied; 250, 100 and 45 µm. The powder was sieved for 1h; after that the sieved powder was separated and the one that was not enough small to pass through 45 µm sieve was grinded up again. This process was repeated till all the power was enough small.
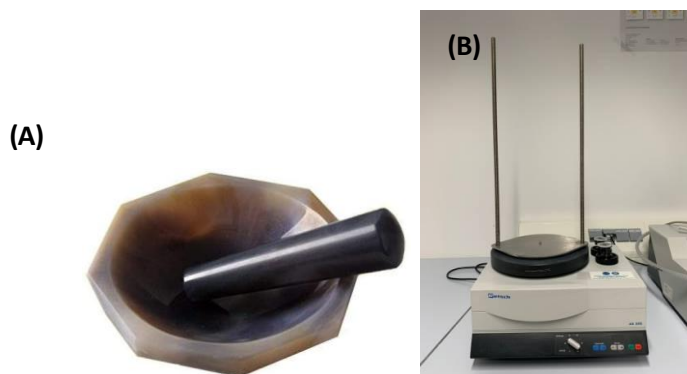


*Figure 4.7: a) Agate mortar to grind up the ceramic powder and b) sieve machine.*

The reduction of the powder size will help us to be able to reduce the nozzle diameter and improve the resolution of the SOFC. In addition, this modification represents the first modification that we are going to conduct on the feedstock and see the affectation on the final sample.

UNIVERSITAT POLITÈCNICA DE CATALUNYA
BARCELONATECH
UPC Escola d'Enginyeria de Barcelona Est

## 4.3    Ceramic inks

On this section, two different things will be explained in detail: *(i)* the fabrication procedure as well as *(ii)* the composition of the ceramic inks that will be employed. This consists on a mixture between three different elements: distilled water, the gelling agent (Pluronic F-127®, see **section 4.1a**) and ceramic powder (see **section 4.1b, c and d**).

To prepare the mixture, the compositions are based on the study conducted by Feilden *et al.* [28] and entitled ***Robocasting of structural ceramic parts with hydrogel inks***, complemented with the results of my Bachelor's project entitled "*3D printing of Solid Oxide Fuel Cell*".

So, to get the printing ceramic material, two steps are important to take into account:

(i)     To make the hydrogel, which consists of a mixture between the polymeric material (Pluronic F-127®) and distilled water.

(ii)    To mix the hydrogel (step *i* explained above) with the desired ceramic material and get the required ceramic paste ready to print.

In order to reach the desired ceramic printable paste, first of all it is required to prepare the hydrogel; Pluronic F-127® mixed with distilled water, during 5 min. at maximum speed, 3500 rpm. This mixture is performed by using a SpeedMixer, **Figure 4.8**.



***Figure 4.8***: *SpeedMixer, the machine used to mix the hydrogel and ceramic pastes.*

On this Master's project several compositions of Pluronic F-127® and ceramic charge were prepared. It was all because one of the main goals of this project was to modify the ceramic ink in order to get the final piece with the desired porosity. **Table 4.1** shows the compositions prepared for this Master's project. Remark that all of them were tried with the processed zirconia powder, as explained in **section 4.2**. After that with the best composition for each part the final feedstocks using 8Y-TZP and the mix of 8Y-TZP + LSGM, were prepared.

UNIVERSITAT POLITÈCNICA DE CATALUNYA
BARCELONA**TECH**
Escola d'Enginyeria de Barcelona Est

Table 4.1: *Different compositions used during this Master's project (the composition presented in this table are in wt. %). In blue colour are represented the composition which were too fluid to print. In orange are represented the inks which were to viscous to print.*

| | Pluronic F-127® (% wt.) | | | | | | | |
|---|---|---|---|---|---|---|---|---|
| | **Powder Charge** | **20** | **25** | **30** | **35** | **40** | **45** | **50** |
| **8Y-TZP** **(% wt.)** | **75** | F1 | F2 | F3 | | | | |
| | **70** | | F4 | F5 | F6 | | | |
| | **65** | | F7 | F8 | F9 | | | |
| | **60** | | F10 | F11 | F12 | F13 | F14 | F15 |
| | **55** | | | | | F16 | F17 | F18 |
| | **50** | | | | | F19 | F20 | F21 |
| | **45** | | | | | F22 | F23 | F24 |
| | **40** | | | | | F25 | F26 | F27 |

As it is shown in ***Table 4.1,*** not all the compositions were able to print. In blue are represented the compositions that were to fluid to print. In green are represented the compositions used during the project, which were numbered as; *F* (feedstock) and a number. Finally, the orange compositions represent the ones that were too dense to print with the printer used on this Master's project.

Once the mixture between the polymeric agent and distilled water is ready it is necessary to store the mixture inside the fridge at a constant temperature (around 4⁰C) for 24 h in order to eliminate the bubbles generated during the mixing process. After that, the gelling agent is ready to prepare the ceramic pastes, following the next steps:

(1) Deposit the desired amount of the gelling agent inside of a plastic container and add the desired amount of ceramic powder. The different amounts of powder are summarized in ***Table 4.1***.

(2) Once the ceramic powder is included with the polymeric mixture it is necessary to mix with the SpeedMixer during 1 min. at 3500 rpm. Afterwards, with a spatula mix the ceramic paste in order to homogenize the desired product and mix again in the SpeedMixer with the same conditions explained above. This process may be repeated until a homogeneous mixture without agglomeration is obtained.

UNIVERSITAT POLITÈCNICA DE CATALUNYA
BARCELONATECH
Escola d'Enginyeria de Barcelona Est

## 4.4    Additive Manufacturing technique

The additive manufacturing (AM) technique that will be used during this Master's project is the Robocasting technique.

### 4.4.1 Machine: set-up

To carry out the Robocasting process, a RepRap BCN 3D+ printer supplied by the "Fundació centre CIM-Universitat Politècnica de Catalunya-BarcelonaTECH" with dual paste head was used. This printing machine was, adapted to print ceramic pastes as it is shown in, *Figure 4.9*.
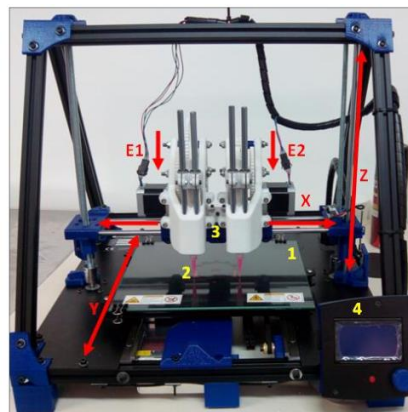


*Figure 4.9: RepRap BCN 3D+ printer used during this Master's project.*

The three axes of the system are shown in red. The head moves on the *X*- and *Z*-axes, while the print bed moves on the *Y*-axis. The complete system consists of the following parts:

1.  <u>Printing bed</u>: The place where the sample is printed. To minimise the adhesion of the sample to the bed, the bed is coated with Parafilm®, to make easier the step to remove the sample from printing bed.
2.  <u>Printing syringe</u>: It acts as a printing head, and is the part of the system where the ceramic paste is loaded.
3.  <u>Print heads</u>: These are made up of *two parts*:
    -   **Base:** Attached to the printer frame. It consists of an eight-gear train that applies the force to the printing piston. The syringe fits into a hole drilled in this base.
    -   **Piston:** It is coupled to the gear train by a toothed face and to the syringe by a male-female system. It is responsible for converting the rotational movement of the gears into uniaxial printing force on the ceramic paste.
4.  <u>Control knob</u>: From where the printer functions are controlled. It contains an SD slot for loading the *GCode* files that will be selected later from the program.

UNIVERSITAT POLITÈCNICA DE CATALUNYA
BARCELONATECH
Escola d'Enginyeria de Barcelona Est

### 4.4.2 Working conditions

The process of AM will be done at the laboratory conditions as summarized below:

- **Temperature:** 21⁰C.
- **Humidity:** 70%.
- **Room pressure:** 1 atm.

Before start to printing is so important to temperate the ceramic paste. With this the temperature of the mix increases, getting the correct viscosity. And we can avoid that the paste might precipitate before the printing process. There are different ways to do that (like heating the mixture), but the best way is to introduce the mixture in the SpeedMixer during 1 min. reaching afterwards the desired viscosity.

### 4.4.3 Printing conditions

To do the AM process there are many conditions to take into consideration and control. Apart from the conditions of the difference percentage of ceramic ink mentioned in **section 4.3,** and the time between the fabrication of the paste and the use of it, and the time between the printing process and the heat treatment, these are the following conditions that you may control in the AM process: *the velocity of the movements, the infill of the sample, the printing pattern, among others.* All these parameters can be controlled by the *Slic3r,* see **Annexe B.2**, programme that transforms the files to the *GCode*. mode, that the machine can read.

During the printing process in this Master's project, the following printing conditions were employed, see **Table 4.2**:

*Table 4.2: Printing process conditions.*

| SOFC geometry | Infill (Figure 4.6) | Pattern (Figure4.7) | Speed for print moves | Speed for non-print moves |
|---|---|---|---|---|
| Tubular | 100% | rectilinear | 2 mm/s | 25 mm/s |

**Figure 4.10.a** exhibits the different infills available. This printing parameter may be defined as the filling of the piece and its value goes from 0 to 100%. In the other hand the different geometries available in the printing software are summarized in **Figure 4.10.b**, being the rectilinear the pattern employed in this Master's project in order to print the tubular geometry.

UNIVERSITAT POLITÈCNICA DE CATALUNYA
BARCELONATECH
Escola d'Enginyeria de Barcelona Est
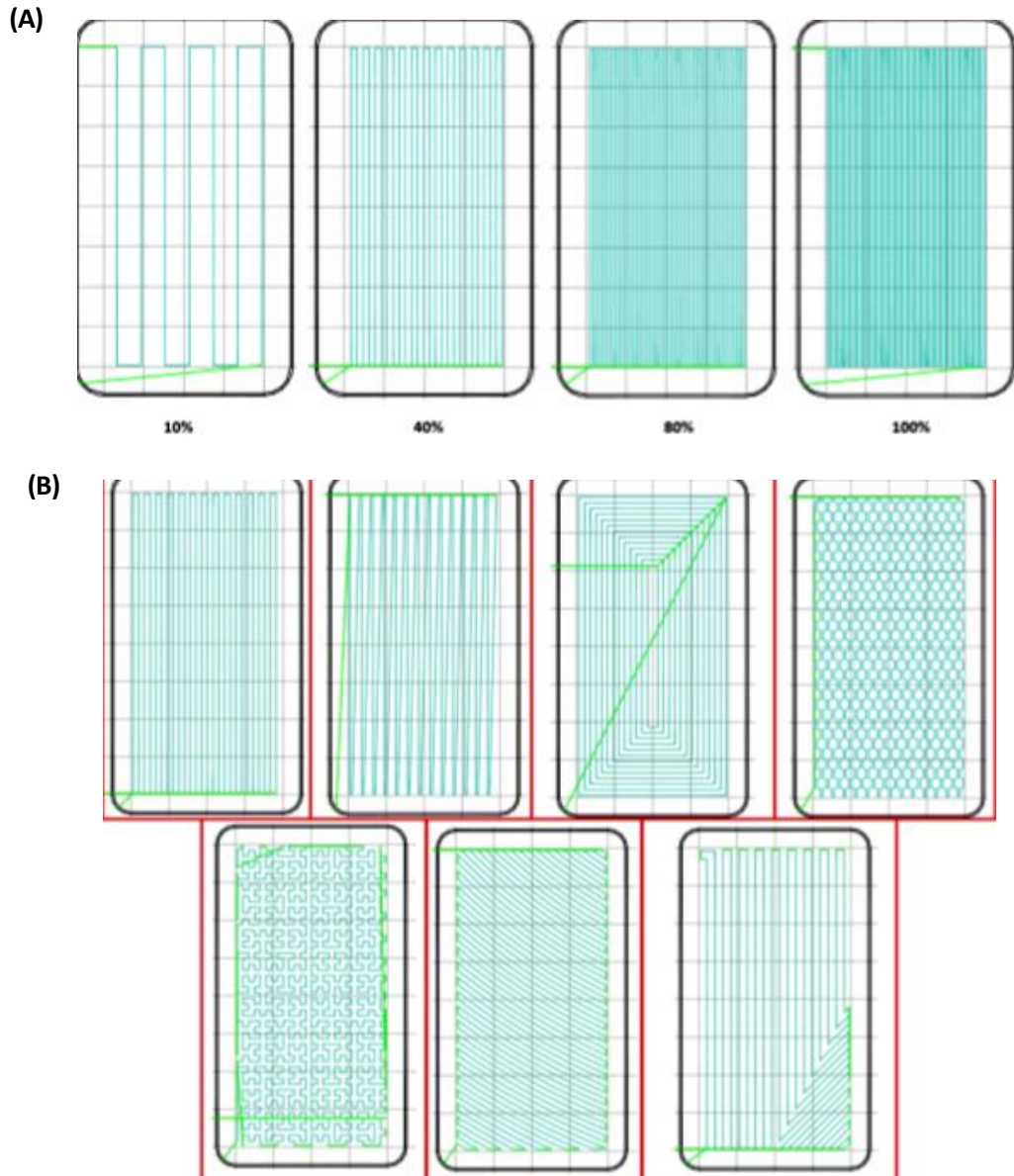
**Figure 4.10:** *a) Examples of different infills for print the samples* [29]*, and b) from left to right and top to bottom: Rectilinear, line, concentric, honeycomb, hilbertcurve, archimedeanchords, octagramspiral* [29].

Apart from the mentioned parameters there is on that play an important role in this project the nozzle diameter size. The used nozzles were distributed from *Nordson*, from the catalogue (**Annex C**), the nozzle type was: *Smoothflow tapered tips* with diameter of 0.25 mm, colour red.

Thus far the used types were the ones with a nozzle diameter of 0.58 mm. But one of the goals of this project was tried to reduce this diameter to improve the resolution of the SOFC. At first sight, we thought that to halve the nozzle diameter would be a good beginning. The final decision was to use this nozzle with a diameter of 0.25 mm for this Master's project.

UNIVERSITAT POLITÈCNICA DE CATALUNYA
BARCELONA**TECH**
Escola d'Enginyeria de Barcelona Est

## 4.5 Sintering process

This step becomes relevant during the process of obtaining the final specimen. In this type of manufacturing process, the parts cannot be compact due to the complex shapes and/or geometries. Within this context, the sintering process is a key step in order to densify the green bodies and reach the desired microstructure and mechanical properties. The sintering process of the different specimens was made on a *Nabethern* furnace, see **Figure 4.11.**



*Figure 4.11: Furnace where the printed specimens were sintered.*

During this Master's project two different thermal treatments (TT) were applied. The TTA was the one applied to zirconia samples. The TTB was the LSGM + 8Y-TZP samples. This sintering process represents an important step during the manufacturing process. It will mark the final crystalline structure which will mark the final conductivity properties of each part.

Talking about 8Y-TZP desired structure was the cubic one, see **section 4.1.b**. **Figure 4.12** shows a phase diagram, where we can see the evolution of the different zirconia allotropic forms as a function of yttria molar percentage in relation of the sintering temperature. An YTZP doped with an 8% molar of yttria was the used material.
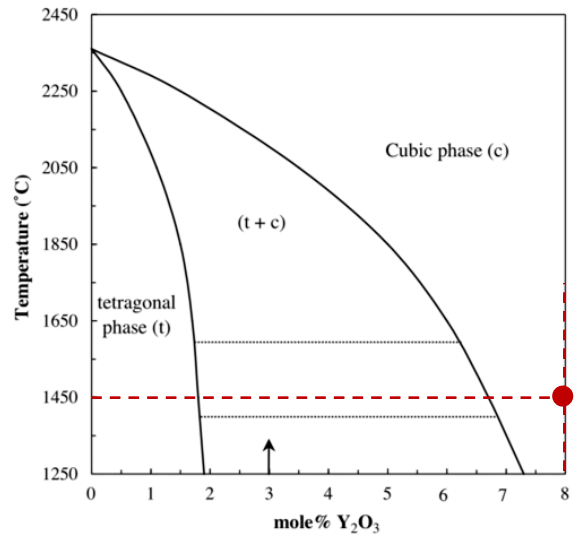
**Figure 4.12**: *Selected region of the ZrO$_2$–Y$_2$O$_3$ equilibrium phase diagram* [30]*.*

TTA applied during this Master's project was the typical one used to sinter the cold isostatic pressing zirconia samples. It features of one first heating ramp till 700$^o$C, as a debinding process. After that another heating ramp to sintering temperature of 1450 $^o$C was applied. After that a holding time of 2h at sintering temperature was done. Finally, the TT ends with a cooling step. All of the applied ramps were of 3$^o$C/min. This TT is represented in **Figure 4.13.**

Regarding LSGM a perovskite structure was the desired one, as it is explained in **section 4.1.c**. As Raghvendra *et. al.* explained in the paper entitled: **Electrical conductivity of LSGM–YSZ composite materials synthesized via coprecipitation route** [31], that a TT under a temperature of 1400 $^o$C for 12h applying a heating rate of 4$^o$C/min, gives us a perovskite orthorhombic LSGM.

TTB features of one first heat ramp till 700 $^o$C as debinding process to eliminate the polimeric agent. 1 h was the holding time at 700 $^o$C. After that another heating ramp to the sintering temperature of 1400 $^o$C was done. The holding time at this temperature was 12h. The TT ended with a cooling step to room temperature. All the applied ramps had a heating rate of 4$^o$C/min [31]. This TT is represented in **Figure 4.13.**
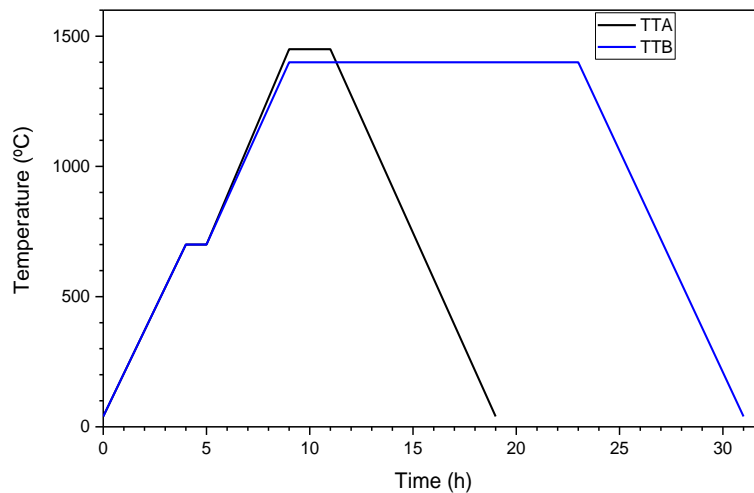
*Figure 4.13: TT applied in this Master's project. In black the TTA for the 8Y-TZP. In blue the TTB for the LSGM + 8YTZP.*

Prior to microstructural and mechanical properties determination, the specimens were carefully polishing following the process described in ***section 4.6***.

## 4.6    Polishing process

The polishing method is an experimental procedure, done with frequency prior to the microstructural and mechanical characterization. In this Master's project, this process is required in order to get a smooth surface in order to evaluate their micromechanical properties by using the Nanoindentation technique, mainly the Hardness (*H*) and elastic modulus (*E*), as well as to evaluate their microstructure and defectology produced during the printing process present in the printed samples by using advanced characterization techniques, like the field emission scanning electron microscopy (FESEM), or Focused Ion Beam (FIB) among other advanced characterization techniques described along the experimental part section.

During this step, two different requirements are necessary to be reached: (1) Planarity of the specimen as well as (2) to get a like-mirror surface.

This part can be summarized in two different steps:

a)  **Sample preparation:** In order to be able to easily prepare the specimen (decrease the roughness) and reach the planarity of the printed sample, they were embedded in an epoxy resin, (the data sheet is available in ***Annexe A.5***), as it is shown in ***Figure 4.14***.

*Figure 4.14: Zirconia samples embedded inside the resin to polish them.*

b) **Polishing process:** The polishing process was done in a conventional polishing machine from Struers (LAboPol-5), see *Figure 4.15.a*. Also, different polishing papers with different grid size of SiC, and diamond suspensions with different particle size were used; all of them shown in *Figure 4.15.b*. *Table 4.3* summarize the main parameters employed in the polishing process.

*Table 4.3: Summary of the different parameters employed during the polishing process, where V means the polishing speed in rpm.*

| Step | 1 | 2 | 3 | 4 | 5 | 6 | 7 |
|---|---|---|---|---|---|---|---|
| V (rpm) | 200 | 200 | 200 | 200 | 200 | 200 | 200 |
| Polishing paper | Sandpaper P:120 | Sandpaper P:320 | Sandpaper P:600 | Sandpaper P:1200 | Polishing cloth | Polishing cloth | Polishing cloth |
| Suspension | Tape Water | Tape Water | Tape Water | Tape Water | 6µm | 3µm | $SiO_2$ colloidal |
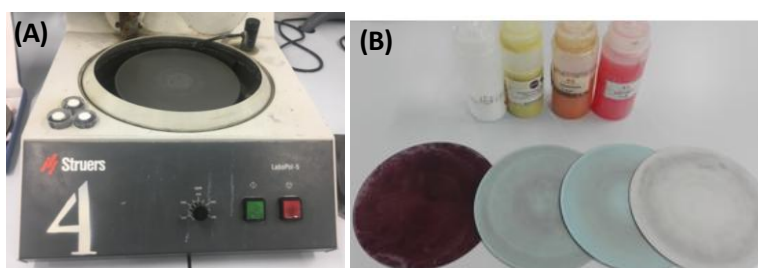


*Figure 4.15: a) Polishing machine of the brand Struers, model LaboPol-5 and b) polishing clothes and suspensions used during the polishing process.*

## 4.7    Characterisation techniques

The main techniques employed to characterise the ceramic printed specimens are briefly explained along this section. They can be divided in three different parts.

### 4.7.1 Feedstock and ceramic ink

#### 4.7.1.1    Particle size

To know the particle size of the ceramic powder before and after two different characterization techniques were used; the first one a particle sizing instrument, laser diffraction particle size by using a *Mastersizer* and some SEM micrographies to check the results from *Mastersizer*.

***Laser diffraction particle size: Mastersizer***

This Mastersizer is particle sizing instrument based in a laser diffraction spectrometry (LDS). In LDS measurement a laser beam passes through a dispersed particulate sample and the angular variation in intensity of the scattered light is measured. Large particles scatter light at small angles relative to the laser beam and small particles scatter light at large angles, ***Figure 4.16.a***. The angular scattering intensity data is then analyzed to calculate the size distribution of the particles that created the scattering pattern using the Mie theory of light scattering. The particle size is reported as a volume equivalent sphere diameter [32].

The Mie theory, describing the interaction between small particles and light is called Lorenz-Mie theory. It starts from Maxwell's equations for an electromagnetic field and results in an exact description of the field when an interaction takes place. If the particles are large relative to the wavelength of the light, the interaction may be interpreted in terms of diffraction. Further, if the distances of the light-source and detection plane from the point of intersection of the scattering object, are large compared to the wavelength of light, the interaction is described by Fraunhofer diffraction theory (FD). When particles suspended in a liquid are analysed, the application of FD theory is questionable, in particular if the particles are small compared to the wavelength of light and the refractive indices are similar [33]. This last affirmation explains the reason why an extra essay is needed to check the results. In addition these theories do not take in account the formation of agglomerations.

The machine used was the Mastersizer 3000 from *Malvern,* ***Figure 4.16.b.*** To make the measurement, solution with the powder to analyze and a solvent must be prepared. The two typical solvents are distilled water or ethanol. Although all the analyzed powders were much agglomerated and ethanol could be help, we decide to use water, because the ceramic is prepared with water instead of ethanol. Another important parameter that you can control is the use of ultrasounds. In this case high percentage of ultrasound was applied which together with a high agitation speed, 2500rpm, helped to avoid the agglomerations. For each solution 10 measurements every 10 seconds were done, the average between these 10 sizes distributions were taken as a reference distribution.

**(A)** Incident light

Small angle scattering

Incident light

Large angle scattering

**(B)**
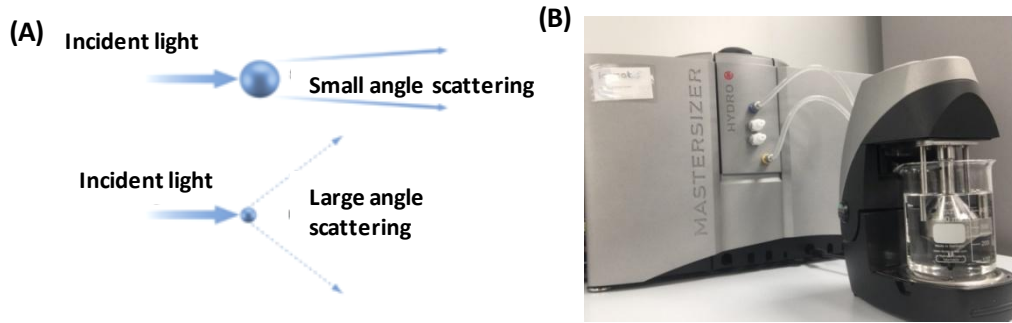
***Figure 4.16:*** *a) Schematic representation of the scattering generated when laser lights interacts with a particle* [32] *and b) Mastersizer 3000 used for this Master's project.*

***Field Emission Scanning Electron Microscope***

Field Emission Scanning Electron Microscope (FESEM) is a Scanning Electron Microscope (SEM) based technique. SEM uses a focused beam of high-energy electrons to generate a variety of signals at the surface of solid specimens. The image is formed in the SEM by an electron beam that crossing the sample scans it and collects the signals that derive from electron-sample interactions.

Secondary electrons (SE), backscattered electrons (BSE), Auger electrons (AE) and x-ray (XR) are the four responses from the interaction between an electron beam and the material to analyze. SE are created when inelastic scattering of the beam electrons ejects weakly bound valence electrons, the information that we can obtain is the topography of the sample. The BSE signal can convey information on the specimen composition, topography, mass thickness, and crystallography. The critical condition for generating characteristic X-rays is that the energy of the beam electron must exceed the electron binding energy, the basic information that you can obtain is a chemical analysis. The AE is generated when inner shell ionization by inelastic scattering of an energetic beam electron that leaves the atom in an elevated energy state which it can lower by the transition of an L-shell electron to another L-shell electron, which is ejected with a characteristic energy, so in fact AE it is not specifically an electron but it is a photoelectron [34].

Theses interactions reveal important microstructural information like: texture, chemical composition, crystalline structure and orientation of materials. FESEM also employs a beam of highly energetic electrons and the concept field appears by the generation of an electric field, because the surface of the samples is conductor. For this process, the equipment requires an extreme vacuum in the column of the microscope (around $10^{-6}$ Pa). FESEM involves an electron emission cathode and anodes, see ***Figure 4.17***. The acceleration voltage between these electrodes is commonly in the range of 0.5 to 30 kV [35].

An electron detector perceived the secondary electrons emitted, and the image is created by comparing the intensity of secondary electrons to the scanning primary electron beam [36].

UNIVERSITAT POLITÈCNICA DE CATALUNYA
BARCELONA**TECH**
Escola d'Enginyeria de Barcelona Est
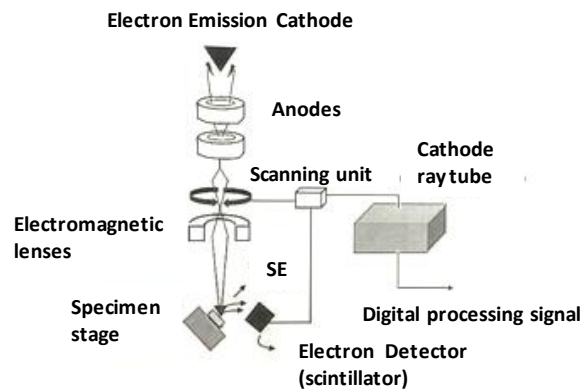
**Figure 4.17:** *FESEM schematic representation* [36] *.*

In this Master's project a FESEM, **Figure 4.18.a,** and a Phenom XL Desktop SEM, **Figure 4.18.b,** were used. The first SEM was used to observe the plastic deformation as well as the damage induced during the indentation process in the sample and the biphasic materials generate in cathode part. The other one was applied to measure the particle size of the commercial powder and post-processing powder.
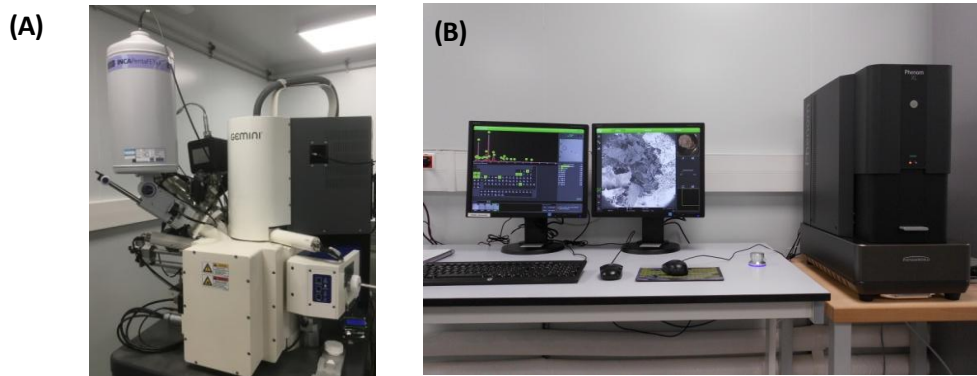


**Figure 4.18:** *a) FESEM model used for this Master's project and b) Phenom XL Desktop SEM.*

### 4.7.1.2    Rheology

In the robocasting technique, as the object is built the extruded filament impinges on the printed part and fuses with it due to surface tension. This means there are no thermal gradients involved in robocasting. Here comes the main reason that the rheological study in robocasting technique is fundamental.

Rheology as a definition is the science of deformation and flow of matter when a force is applied. When a stress (σ) is applied to a solid it deforms elastically according to Hooke's law, **equation 3**:

$$\sigma = G \cdot \gamma \hspace{8cm} \textbf{\textit{equation 3}}$$

Where $G$ is the elastic modulus and γ is the strain. When the strain falls to zero the sample recovers its original shape. This is commonly illustrated by a spring. If the shear is large then the structure of the sample can break and hence it not only deforms but starts to flow. In the simplest case the response follows Newton's law, *equation 4:*

$$\sigma = \eta \cdot \dot{\gamma} \hspace{6cm} \textbf{\textit{equation 4}}$$

Where $\dot{\gamma}$ is the velocity gradient (also known as the shear rate) and η is a coefficient of viscosity (or simply the viscosity). By definition Newtonian behaviour is when the viscosity is independent of shear rate and does not depend on the shear history. Most simple liquids like water, acetone, or oils are Newtonian. Liquids showing any variation from this behaviour are referred to as non-Newtonian. *Figure 4.19* illustrates the different types of rheological response by plots of shear stress vs. Shear rate; these are also known as flow curves [37]. Pluronic presents behaviour like a shear-thickening material.
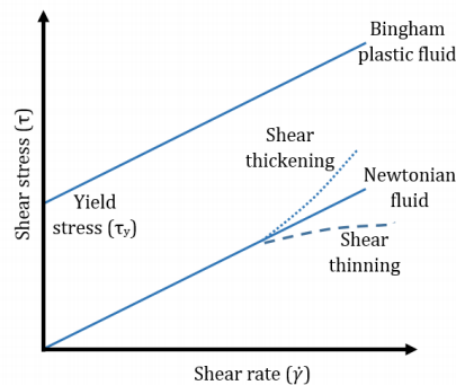


*Figure 4.19: Classification of fluids, based on relationship between shear stress and shear rate* [38]*.*

To measure this behaviour exist two types of rheometer; the drag flow type or the rotational flow type. The first one is based on the time that the material needs to flow through a receptacle when a uniaxial stress is applied the most typical ones are; capillary rheometer or the plastometer. In the second type of rheometers a shear stress is applied due to the rotational movement of the machine and a torque is registered.

For this Master's project a rotational rheometer with a plate-plate, *Figure 4.20.a,* was used, because small amount of material is needed and is the most useful rheometer for high viscosity materials. A sample is sheared while sandwiched between two plates, with the upper plate moving, under a frequency of 1Hz and the lower plate remaining stationary. The oscillation shear stress mode was used. In these cases Hooke's law can be represented by *equation 5* [39]*:*

$$G^* = \tau/\gamma = |G' + G''| \hspace{5cm} \textbf{\textit{equation 5}}$$

With complex shear modulus $G^*$, shear-stress amplitude $\tau$, and strain amplitude $\gamma$. $G^*$ describes the entire viscoelastic behaviour of a sample and is called the complex shear modulus $G^*$. Also, this complex modulus can be expressed as the modulus of the sum of storage component which is related to the elastic part of the material ($G'$, storage modulus) and the loss component which told how the material dissipates energy ($G''$, loss modulus). In **Figure 4.20.b**, the relationship between $G^*$, $G'$ and $G''$ is shown, where the x-axis represents the elastic portion of the behaviour and the y-axis represents the viscous portion.

The stress applied went from 100 to 10000Pa. All the essay was done under a constant temperature of 25ºC the one used during the printing process. The gap between the top and bottom plate was 1mm. The results obtained were the $G'$ and $G''$ function of the shear stress ($\tau$), useful to know the yield stress of the ceramic ink which represent the stress value when the material loss the properties, breakage of the ceramic paste.
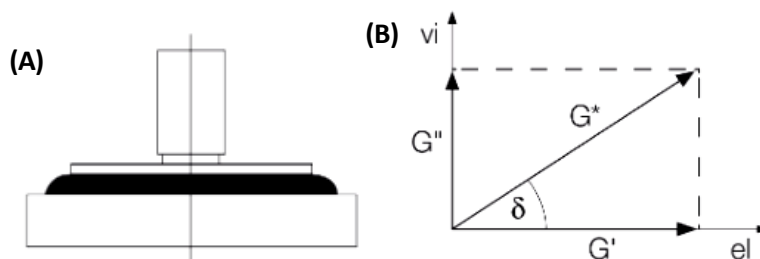


*Figure 4.20:* a) Schematic representation of a plate-plate measuring system and b) vector diagram illustrating the relationship between G*, G' and G''. The elastic portion of the viscoelastic behavior is presented on the x-axis and the viscous portion on the y-axis. [39].

### 4.7.2 Microstructural characterization

#### 4.7.2.1    Density

The study of the density of the printed part is decisive for the analysis of the results; since it indirectly gives the percentage of internal porosity as well as this parameter will lead to compare the quality of the printed specimens with the specimens manufactured by using the conventional ceramic processing routes.

The aim of the study is seen the importance of the adhesion between layers on 3D printed ceramic samples, studying samples with different induced porosity.

The density of the pieces has been determined by the Archimedes method by using the equipment presented in **Figure 4.21**, which is based on the Archimedes principle. It says that by submerging a body into a fluid it receives an upward thrust proportional to the density of the fluid, the volume of

UNIVERSITAT POLITÈCNICA DE CATALUNYA
BARCELONATECH
Escola d'Enginyeria de Barcelona Est

the submerged body and the gravity of the earth. In this sense, measuring the relative mass of the body when submerged in distilled water and the mass of the body in air, the thrust force can be determined.

All the measures were made in a balance from *Mettler Toledo*, model xs3035, as it is depicted in *Figure 4.21*. With the *equation 6*, the density value can be determined.

$$\rho = \frac{A}{A-B} \cdot (\rho_o - \rho_L) + \rho_l \,, with \, \rho_o = 1 \frac{g}{cm^3} \;\; (auxiliary \; fluid); \; \rho_L = 0.0012 \frac{g}{cm^3} \qquad \textbf{\textit{equation 6}}$$

where *A* and *B* in this equation represents the weight of the specimen in air and in the fluid employed (distilled water), respectively.
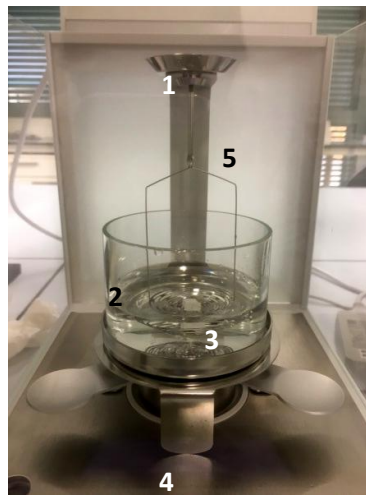


*Figure 4.21: Archimedes method set-up.*

In the *Figure 4.21*, the difference parts of the balance are shown:

1. *Platform to locate the sample to calculate the weight of the sample in the air.*
2. *Recipient to fill the fluid (distilled water) to submerge the sample.*
3. *Platform to place the sample to calculate the weight of the sample in the water.*
4. *Zone to support the recipient of the water.*
5. *Support to join the part 1 and 2.*

Furthermore, it is necessary to highlight that the environmental conditions may take into consideration, being these:

- **Temperature:** 22 ⁰C
- **Auxiliary fluid:** distilled water
- **Principal fluid:** air

UNIVERSITAT POLITÈCNICA DE CATALUNYA
BARCELONATECH
Escola d'Enginyeria de Barcelona Est

#### 4.7.2.2 Dimensions

Due to the idea of study the porosity of the samples by the modification of the feedstock, the contraction of the samples is needed to study. For that reason, the use of magnifying glass was needed to measure the transversal section and the high of the samples to know the volumetric shrinkage.

The magnifying glass used during this project was an Olympus SZX16, see *Figure 4.22.* It was used a magnification of **x0.7** to be able to measure all the section.



*Figure 4.22:* Magnify lent used during this project.

### 4.7.3 Micromechanical characterization

Although a SOFC stack is not a structural component, it is important to assure a minimum structural integrity because without stack integrity there would not present functionality in the future SOFC. Due to that this mechanical characterization is a necessary step to do.

#### 4.7.3.1 Nanoindentation

Hardness (*H*) has been defined as "material's resistance to plastic deformation". The term *H* may also refer to resistance to bending, scratching, abrasion or cutting. The usual method to achieve *H* value is to measure the area of an indentation left by an indenter of specific shape, with a specific force applied for a specific time.

The results of this test are dependent on the scale and the test method. So, depending on the characteristics of the indentation (mainly in terms of applied load) and the strain field, mechanical testing methods can be classified as macro-, micro-, nano- and pico-indentations.

UNIVERSITAT POLITÈCNICA DE CATALUNYA
BARCELONATECH
UPC   Escola d'Enginyeria de Barcelona Est

Macro-indentation tests are characterized by indentations loads L in the range of 2N < L < 30kN. The main macroscale tests used by the industry and research communities are: *Brinell, Meyer, Vickers, Rockwell, Shore Durometer, and the International Rubber Hardness Degree.* Micro-indentation tests are characterized by indentations loads L in the range of L\2 N and penetrations h>0.2 μm. There are two main tests used at this scale: *Vickers* and *Knoop*. In both cases, macro and micro-indentation, the hardness is correlated with the depth which such indenter will sink into the material, under a given load, within a specific period of time [40].

In the nanoindentation test, the indenter is pushed into the surface of the sample producing both elastic and plastic deformation of the material. The first difference with macro- or micro-indentation tests is that, in the nanoindentation machines, the displacement h and the load L are continuously monitored with high precision. During the nanoindentation process, the indenter will penetrate the sample until a predetermined maximum load $P_{max}$ is reached, where the corresponding penetration depth is $h_{max}$. When the indenter is withdrawn from the sample, the unloading displacement is also continuously monitored until the zero load is reached and a final or residual penetration depth $h_f$ is measured [40]. So thanks to Oliver and Pharr method Hardness (*H*) and Elastic modulus (*E*) can be calculated [41] [42].

One of the most influencing parameters in the micromechanical testing of materials by Instrumented Indentation Technique  (IIT) is the geometry of the used tip indenter. Depending on their geometry different properties can be determined. There are mainly two different families of indenter tips:

- **Sharp tips**, they present self-similar geometries with a stress singularity at the tip of its tip, theoretically in the tip the contact area is 0 and the stress tends to infinite values. This fact always assures an elasto-plastic contact from the first moment of contact. Normally this type of indenters are those used to determine *hardness, fracture toughness, yield strength, etc.*
- **Blunt tips**, with geometries that enable elastic contact at the beginning of the loading. This fact makes possible the determination and study of the elastic modulus as well as the extraction of the indentation stress-strain curve. Due to the fact that they do not have self-similar geometries there is difficulty in estimating contact area at larger depths.

In this Master's project, the nanoindentations were applied in order to determine the mechanical properties (hardness and elastic modulus) of both materials to compare them with the literature. To do that a Berkovich tip was used, see ***Figure 4.23***.
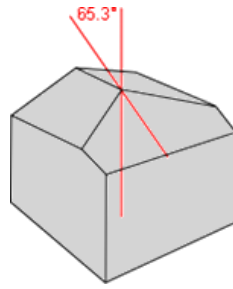
*Figure 4.23: Berkovich tip* [43]*.*

The Berkovich Diamond tip is a three-sided pyramid. The angle between the centreline and the three faces is 65.3⁰. The three face design allows grinding the tip to a sharp point. It is suitable for bulk materials, thin films, polymers, scratch testing and wear testing [43].

Hardness (*H*) and elastic modulus (*E*) are the most commonly measured properties as a function of the displacement into the surface (*h*) determined during a nano-indentation essay. The method of Oliver and Pharr [41] [42] is used to directly determine the micromechanical properties through the loading-unloading (*P-h*) curve. This methodology allows determining on a direct way both mechanical properties. This method can obtain these information thanks of the data obtained during one cycle of loading and unloading, from an indentation of the material.

In particular, to get the values of these properties the procedure is based on the unloading process shown schematically in *Figure 4.24*, in which it is assumed that the behaviour of the Berkovich indenter can be modelled by a conical indenter [44].
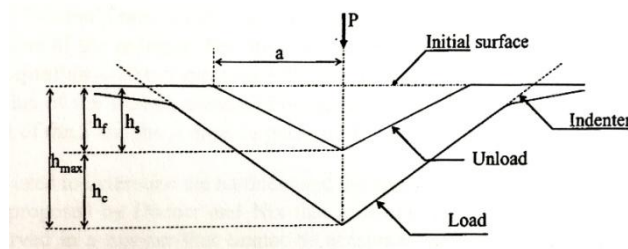


*Figure 4.24: Schematic illustration of the unloading process showing parameters characterizing the contact geometry* [45].

Three are the principal conditions that you can control: the number of indentations per test, the distance between each indentation and the depth of the print. These two last one are really important, because we must avoid the influence of the plastic deformation region, generated during the indentation process, of one indentation regarding the neighbouring prints, which could influence in the final results. So depending on the depth print, the plastic region generated is modified and the distance between the each indentation is going to be different for each case.

**Contact mechanisms**

*Elastic contact*

Due to the bluntless inherent to spherical tips, spherical indentation tests have traditionally been invoked for the study of elastic contact mechanisms as well as of the elasto-plastic transition of different materials using the Hertz theory. The elastic regime of spherical indentation may be writeen as:

$$P = \frac{3}{4} \cdot E_{eff} \cdot \sqrt{R} \cdot h_{max}^{3/2} \qquad\qquad \textbf{\textit{equation 7}}$$

The Hertz theory is derived from the analysis of the well-known scenario of the contact between a rigid sphere and a flat surface, which is mainly governed by the contact point (*a*). This parameter is a function of the indenter load (*P*), the indenter radius (*R*) and the elastic properties of the material as seen in the following expression :

$$a = \sqrt[3]{\frac{3}{4}\frac{P \cdot R}{E_{eff}}} \qquad\qquad \textbf{\textit{equation 8}}$$

where $E_{eff}$ is the effective modulus and determined through the following expression:

$$E_{eff} = \frac{1}{\beta} \cdot \frac{\sqrt{\pi}}{2} \cdot \frac{S}{\sqrt{A(h_c)}} \qquad\qquad \textbf{\textit{equation 9}}$$

Then, the elastic modulus (*E*) can be extracted using the following expression:

$$\frac{1}{E_{eff}} = \frac{1-v^2}{E} + \frac{1-v_i^2}{E_i} \qquad\qquad \textbf{\textit{equation 10}}$$

where *E* and $v$ are the elastic modulus and the Poisson's ratio for the material tested and the other terms with the subindex *i* correspond to the mechanical properties of the indenter. For a diamond tip indenter these values are 1141 GPa and 0.07, respectively as reported in Ref [41] [42].

Moreover, for a spherical indenter, the radius of the circle of contact is given by *equation 9* where the first part of the equation can be approximated to the second expression due to in small deformations the contact depth ($h_c$) is small enough in comparison to the indenter radius:

$$a = \sqrt{2 \cdot R \cdot h_c - h_c^2} \sim \sqrt{2 \cdot R \cdot h_c} \qquad\qquad \textbf{\textit{equation 11}}$$

UNIVERSITAT POLITÈCNICA DE CATALUNYA
BARCELONATECH
Escola d'Enginyeria de Barcelona Est

The typical indentation stress-strain curve, determined at macroscopic length scale by using conventional tensile tests, can be extracted by means of spherical indentation plotting the mean contact pressure or the indentation stress ($p_m$) against the indentation strain ($a/R$) as follows:

$$p_m = \frac{P}{\pi \cdot a^2} = \left(\frac{4 \cdot E_{eff}}{3 \cdot \pi}\right)\left(a/R\right)$$  *equation 12*

Moreover, by representing the indentation stress-strain curve and correctly determine the $p_m$, it is possible to characterize other mechanical parameters of the material, such as yield stress ($\sigma_{ys}$), maximum tensile stress ($\sigma_{tm}$), and the maximum shear stress ($\tau_{max}$). In this sense, the $\sigma_{ys}$ is determined through the following expression:

$$\sigma_{ys} = p_m/\vartheta$$  *equation 13*

where $\theta$ is called constrained factor and depends on the geometry of the indenter and friction at the interface, being the parameter equals to 1.1. The $\sigma_{tm}$ is produced along the contact perimeter, and determined as follows:

$$\sigma_{tm} = 1/2 \cdot (1 - 2 \cdot v) \cdot p_m$$  *equation 14*

The $\tau_{max}$ is produced beneath the indentation axis at a depth equals to 0.46 times the contact point (0.46·a), and equals to:

$$\tau_{max} = 0.46 \cdot p_m$$  *equation 15*

### Elasto-plastic contact

When the applied load is higher that required to reach the yield strenth, the experimental values in the loading curve cannot be fitted with the Hertz equations, see *equation 7*. In this case, the load-displacement relationship can be written as:

$$P = C \cdot h^2$$  *equation 16*

Where *C* is a constant. Furthermore, with the Oliver and Pharr method [41] [42], the constant depth can be obtained as follows:

$$h_c = h_{max} - \varepsilon \cdot P_{max}/S$$  *equation 17*

where $h_{max}$ is the maximum indentation depth, $\varepsilon$ is a constant (0.75 for a Berkovich indenter), $P_{max}$ is the maximum indentation load and *S* is the contact stiffness calculated from the linear part in the unloading curve. The contact area ($A(h_c)$) is calculated using the following expresion:

UNIVERSITAT POLITÈCNICA DE CATALUNYA
BARCELONATECH
Escola d'Enginyeria de Barcelona Est

$$A(h_c) = 24.5 \cdot h_c^2 \qquad\qquad \textbf{equation 18}$$

The indentation hardness (*H*) value can be defined as:

$$H = \frac{P_{max}}{A(h_c)} = \frac{P_{max}}{24.5 \cdot h_c^2} \qquad\qquad \textbf{equation 19}$$

During an indentation essay, the print that generates the tip has a zone with an elastic deformation and when the applied stress is higher than the yield strength of the material the plastic deformation zone appears. The elastic deformation zone is near 20 times the $h_{max}$, while the plastic zone has a rate of 7 to 10 times the maximum penetration depth. For this reason, to avoid the influence of the plastic zone to other indentation and slightly modify the hardness value, the distance between imprints at least may be keep constant and equals to 7-10 times the displacement into surface.

To make this essay on this Master's project and attempting to evaluate the composite hardness and elastic modulus for the printed specimens, a homogeneous array of 16 imprints (4 by 4), shown in **Figure 4.25.a**, was performed by using the Berkovich Diamond tip indenter. This array was performed at 2000 nm of maximum displacement into surface or until reaching a maximum applied load of 650 mN by using a nanoindenter XP (MTS, see **Figure 4.25.b**) equipped with a continuous stiffness measurement (CSM) module, the later allowing a dynamic determination of the mechanical properties during the indentation process. A constant distance around 50 $\mu$m was held between each imprint in order to avoid any overlapping effect. Along the indentation process, the indentation strain rate was held at 0.05 s$^{-1}$.
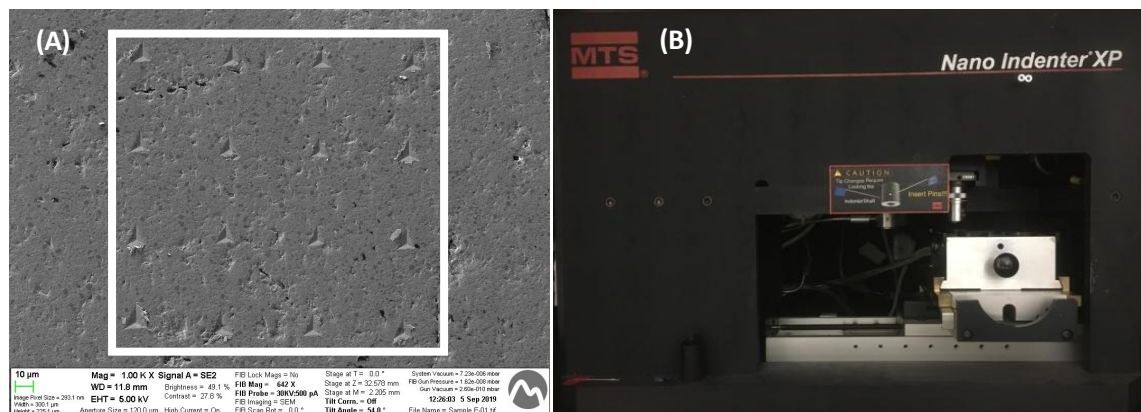


*Figure 4.25: a) Array of 16 imprints (4 by 4) on the zirconia sample, and b) Nanoidenter set-up used during this Master's project.*

### 4.7.3.2    Atomic Force Microscope

To make an accurate study of the topography of the sample as well as the main deformation mechanisms induced during the indentation process an atomic force microscopy (AFM) was used. It measures forces between a sharp probe (with a tip diameter < 10nm) and surface at very short distance, 0.2 – 10 nm probe-sample separation, providing a 3D profile of the surface of the sample even at nano-lenght scale. A flexible Si cantilever supports the probe and the AFM tip touches the sample surface and simultaneously registers the force between the probe and the surface [46].

The movement of the probe is typically measured by a "beam bounce". A semiconductor diode laser is bounced off the back of the cantilever against a position sensitive photodiode detector. This detector measures the bending of the cantilever resulting from the tip scanning over the sample. The deflections measured by the cantilever, are used to generate a map of the surface topography [47]. A schematic figure of an AFM is represented in *Figure 4.26.a.*

The AFM has normally three operation modes:

i.   **Contact mode:** The tip is in contact with the surface and the separation between the probe and surface is less than 0.5 nm, it experiences repulsive Van der Wals forces.

ii.  **Tapping mode:** The tip zooms in and out in a probe-surface separation of 0.5 to 2 nm. In this project this was the working operation mode.

iii. **Non-contact mode:** In this case the probe-surface separation is around 0.1 to 10 nm.

For this Master's project the Dimension D3100 (Veeco), see *Figure 4.26.b,* was used to study the residual indentation imprints.
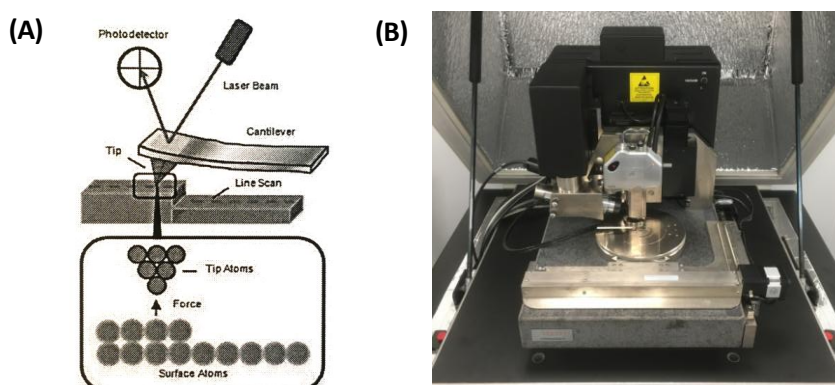


*Figure 4.26:* a) Schematic representation of AFM equipment [46] and b) AFM set-up used during this Master's  project.

### 4.7.3.3    Focused ion beam

Focused ion beam (FIB), in a simple definition is an instrument that resembles a FESEM. FESEM uses a focused beam of electrons to image the sample while FIB setup uses a focused beam of ions instead. The *Figure 4.27* shows a schematic image of the specimen chamber of the equipment, the dual system FIB/FESEM.

The operation principle of the FIB microscope consists of sputtering atoms onto a target material, with a high energetic Gallium ion beam, $Ga^+$. Ions are generated from a Ga liquid metal ion source composed of a Ga reservoir mounted above of a tungsten needle. Ga source is heated up to its melting point and then it flows to the tip of the needle. An intense electric field is produced at the source tip that ionizes the gallium, draws the liquid metal into the fine tip, of about 2-5nm in diameter, and extract ions from narrow tip. The $Ga^+$, are accelerated down the column in an electrical field of about 30 KV and sputtered over the region of interest [48].

This FIB system must be equipped with a Gas Injection System (GIS, see *Figure 4.27*) that can handle up to five different gases. This GIS will have a different function depending on the application of FIB [49]:

i. **Ion milling:**  Milling is actually an atomic collision process that ends up in the removal of the material from the ion–sample interaction volume. It can be used to create both simple structures, such as lines, rectangles, or circles in the material, and complex patterns, bitmaps, and streamline files. This process is similar to lithography; however, the advantage here is that it does not require the use of masks. Local assisting gases exposed by GIS that are integrated into dual-beam platforms can help in enhancing the removal of atoms from the material surfaces.

ii. **Deposition:** The ion or electron beams can be used in a deposition system, allowing the addition of material instead of removing the material. Deposit materials are often supplied by an internal gas delivery system that locally exposes a chemical compound close to the surface impact point via GIS. The chemical gas compound is usually in the precursor form and consists of organometallic molecules. When this compound is exposed to the region of interest, beams decompose the molecules locally and deposit almost-pure material onto the surface.

UNIVERSITAT POLITÈCNICA DE CATALUNYA
BARCELONA**TECH**
Escola d'Enginyeria de Barcelona Est
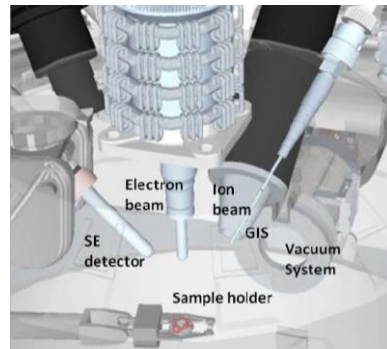
*Figure 4.27*: *Illustration of the specimen chamber of a dual-beam (FIB/FESEM) platform* [49].

In this Master's project the subsurface damage generate by a Berkovich indentation were inspected by means of FIB. Cross-sectioning and microscopy were conducted using a dual beam Workstation (Zeiss Neon 40) with an ion beam current of 500 pA.

# 5. Results and discussion

## 5.1    Feedstock particle size characterization

One of the goals of this Master's project is try to reduce the particle size to reduce the nozzle diameter and improve the SOFC resolution during the printing process. The results obtained during this part are obtained using the Mastersizer and SEM (***Section 4.7.1***). In ***Figure 5.1.a, 5.2.a*** and ***5.3.a*** the size distribution of commercial feedstock powder (black) and post-processing powder (blue) determined by using the laser diffraction technique are shown for the 8Y-TZP, LSGM and Gd, respectively. On the other hand, **figures 5.1, 5.2** and **5.3.c** and **d** show the SEM micrographs for the commercial and post-processed powder, respectively.

Regarding the powder the first thing to achieve is the reduction of the powder size to a diameter 10 times less than the nozzle diameter, so at least we are going to try to search a particle size of 25 µm. Apart from that in general a non-monomodal distribution with spherical particle shape is preferable in order to enhance the sintering step and be able to obtain the desired sintering density. In this sense, as it is depicted in the particle size distribution, the post-processing trend exhibits a bi-modal distribution for the 8Y-TZP and tri-modal distribution for the LSGM and Gd.
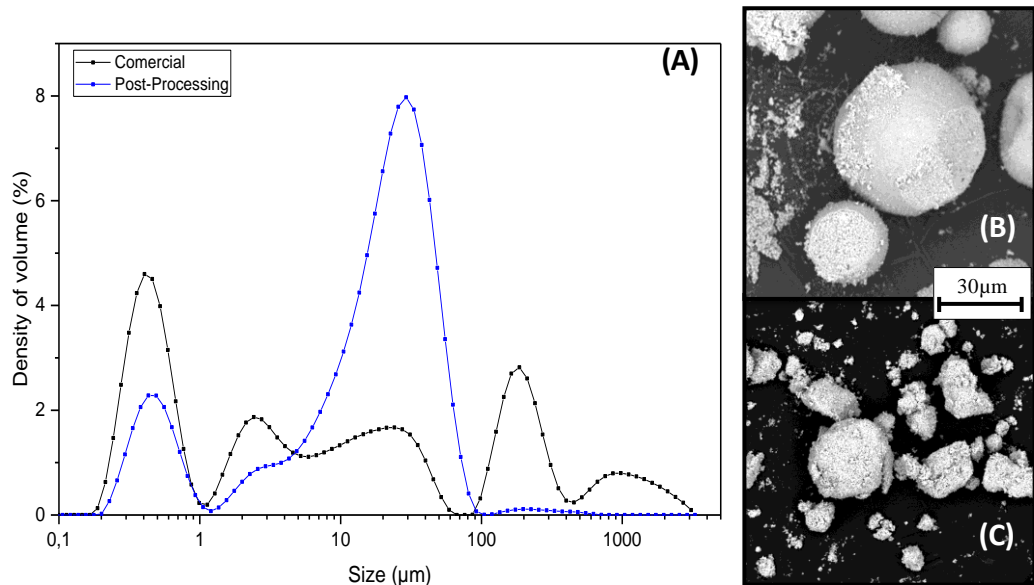


***Figure 5.1:*** *a) Particle size distribution of 8Y-TZP powder, in black the comercial one and in blue the post-processed, b) SEM micrograph of commercial powder and c) SEM micrograph of post-processed powder.*
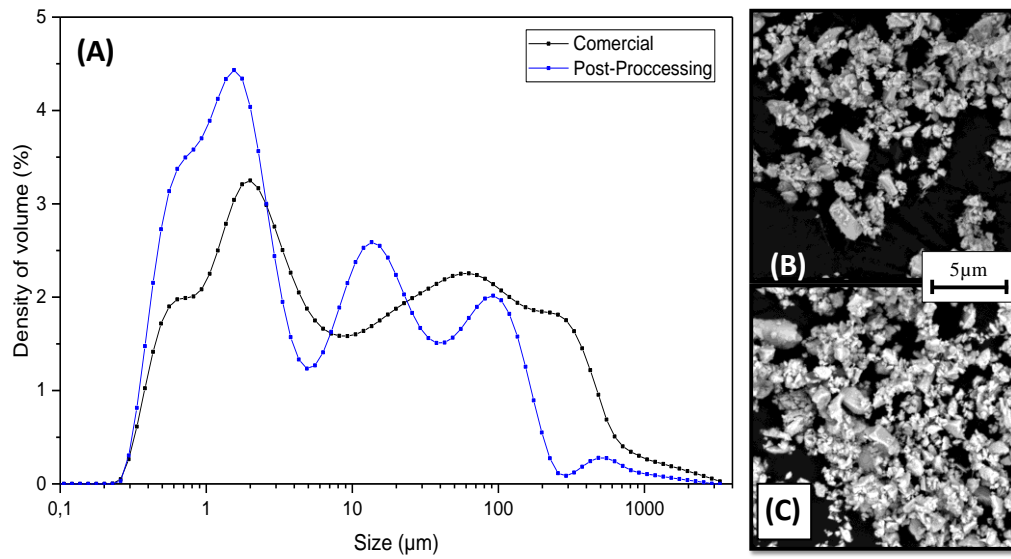
**Figure 5.2:** *a) Particle size distribution of LSGM powder, in black the comercial one and in blue the post-processed, b)SEM micrograph of commercial powder and c) SEM micrograph of post-processed powder.*
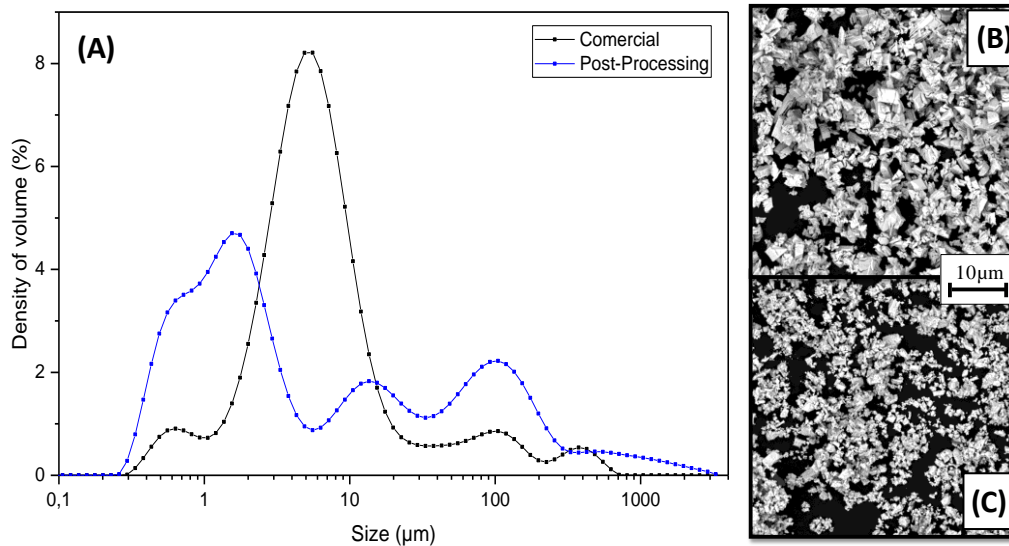


**Figure 5.3:** *a) Particle size distribution of Gd powder, in black the comercial one and in blue the post-processed, b)SEM micrograph of commercial powder and c) SEM micrograph of post-processed powder.*

In **FIgure 5.1.a** we can observe that the processing step gives a high density of particles with a bi-modal particle size distribution, ranged between 20 and 30 µm (coarse particles) and another one with an average size of around 0.5 µm (fine particles). This distribution is preferred that the comercial one because with the post-processing disolves partially the feedstock aglomerates, with an average dimension arround 200 µm. This fact is confirmed in **Figure 5.1.b**, where we can observe an aglomerate with a magnitud arround 100 µm, while in **Figure 5.1.c** the particles shown there have an average size less than 30 µm.

UNIVERSITAT POLITÈCNICA DE CATALUNYA
BARCELONA**TECH**
Escola d'Enginyeria de Barcelona Est

In LSGM case we can see in ***Figure 5.2.a*** that the comercial powder presents a bimodal size distribution with a peak in particle dimension of arround 2 µm and another with a particle size distribution ranged between 50 to 150 µm. Thanks to processing step, we are able to homogeneize the feedstock and mantain the bimodal distribution of the feedstock to magnituds lowers than 1 µm. The second peak is modified and presents two marked peaks, fine and coarse particle size distribution of around 10 and 100 µm, respectively.

Regarding Gadolinium, ***Figure 5.3.a*** shows us that comercial powder presents monomodal particle size distribution with an average peak centered at around 6 µm. With processing step the monomodal distribution desapears and the new one presents three peaks, the first one with an average particle size of 1 µm, the following peak appears at around 10 µm and the last one in a dimension of 100 µm. It is true that post-processing powder presents some particles with a huge particle size, but it has a non-monomodal distribution which represents a benefit respect comercial powder.

In both cases LSGM and Gd, the SEM micrographs presented in ***Figures 5.2.b-c*** and ***Figure 5.3.b-c***, show that the particles do not exhibit a spherical shape. It can be explain by the perovskite cristaline structure that present both materials as well as the post-processing powder has not been sprayied. Even so during printing process it does not represent a big issue because we do not use directly these powders, a mixture with zirconia is the printable one.

After to see that the chemical processing of powder with a following step of sieve, gives us a sustantial reduction of the powder size with a better particle size distribution (not monomodal) as well as a reduction of the agglomeration formation. Within this context, we decide to apply this feedstock modification to the corresponding ceramic powder mixed with 8Y-TZP for each part, ***section 4.2***. After that some SEM micrographs were taken to asure that the final mixture presented the relevant features. In ***Figures 5.4*** and **5.5** a SEM micrographs showing the final feedstock is presented for the LSGM+8Y-TZP and Gd+8Y-TZP, respectively.
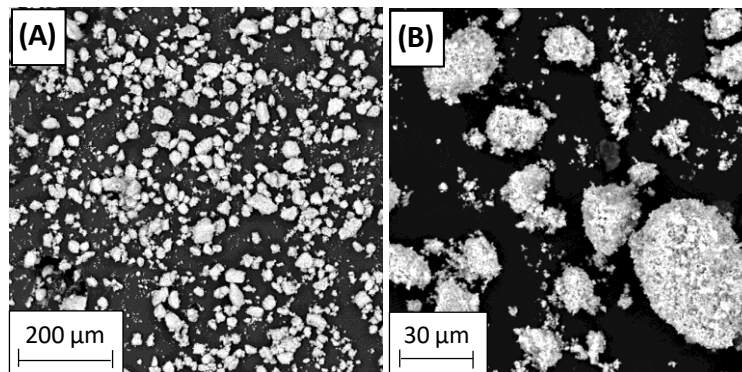


*Figure 5.4: SEM micrographs of powder mixture between LSGM and 8Y-TZP; a) low and  b) high magnification.*
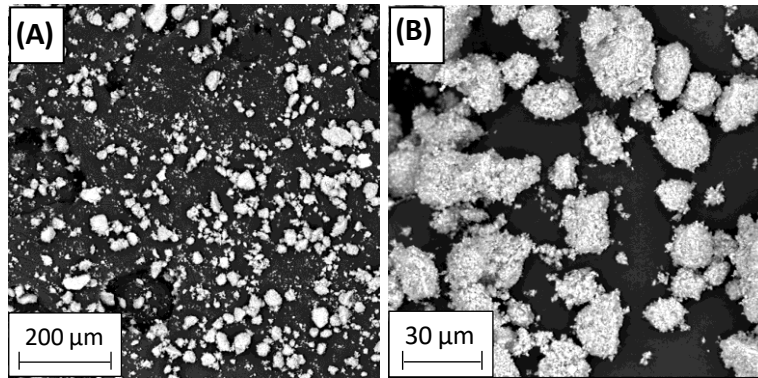
*Figure 5.5: SEM micrographs of powder mixture between Gd and 8Y-TZP; a) low and b) high magnification.*

Regarding the final mixtures between 8Y-TZP with LSGM and Gd, **Figures 5.4.a** and **5.5.a** show that in both cases a shape near spherical one is obtained, so thanks to mix the electrode material with 8Y-TZP helps to solve the problem presented with the powder shape shown in **Figures 5.2.b-c** and **5.3.b-c**. Concerning the powder size distribution (**Figures 5.4.b** and **5.5.b**) show that both mixtures posses an average size distribution smallers than 30 µm.

## 5.2    Optimal ceramic ink

### 5.2.1 Composition of the feedstock

In this section, the results of the best feedstock composition for each part will be presented. As it is presented in **Table 2.2** regarding porosity, each part needs to present a specific value. For the electrolyte part a fully dense part is demanded. So, for this Master's project we decided that a relative density of 95% would be the minimum required value. Concerning the electrodes part, cathode and anode, in **Table 2.2** is summarized that they must present a porous microstructure, ranged between 20 to 40% as shown in Ref. [50].

As it is depicted in **Figures 5.6.a** and **5.7.a** the distribution of density and porosity are represented respectively as a function of the Pluronic and 8Y-TZP content, in wt. %. The feedstock compositions used to print each sample are presented in **Table 4.1**. The density percentage is plotted in **Figure 5.6.b** as a function of the Pluronic content and as a function of the ceramic charge in **Figure 5.6.c**. The same case is presented in **Figure 5.7.b** and **5.7.c** but in this case as a function of the porosity percentage.

Even though we cannot exactly be considered the porosity percentage values as the difference of relative density to 100% of full density, which is a good approach. Maybe as a future work the use of the helium pycnometer or even Micro-CT reconstruction, should be considered to achieve more

UNIVERSITAT POLITÈCNICA DE CATALUNYA
BARCELONATECH
Escola d'Enginyeria de Barcelona Est

accurate study of porosity; percentage, distribution and interconnection between the porous and these representations will be more accurate.
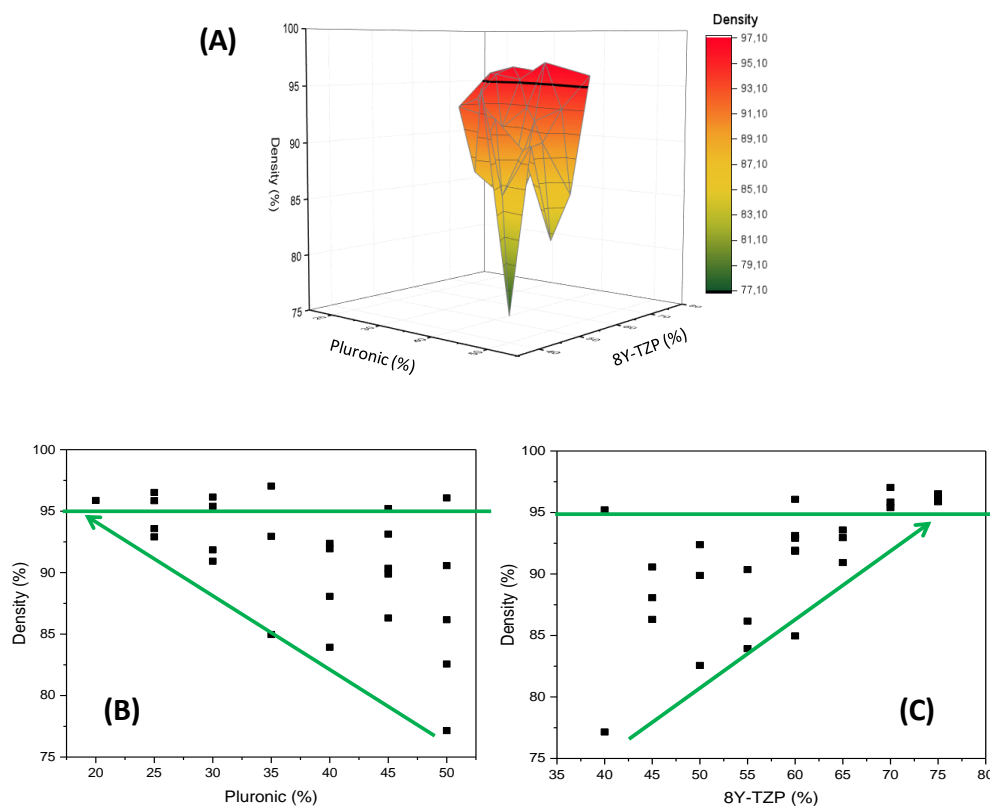


***Figure 5.6:*** *a) 3D representation of the different 3D printed specimens; in it shown the density as a function of Pluronic and ceramic charge, b) plot of density values as a function of the Pluronic content and c) density percentage representation as a function of the 8Y-TZP content.*

For dense samples, the optimal feedstocks were the ones that gave a printed sample with a relative density higher than 95%. As it is depicted in ***Figure 5.6.a***, all the compositions above the black line that represents the reddish zone of compositions are the one which accomplish the requirement in terms of density. In ***Figure 5.6.b*** is possible to observe that the optimal feedstocks presents a Pluronic charge ranged between 20 to 35 wt. %. In this sense, the sample with a 50 wt. % of Pluronic is discarded because this high load of Pluronic may not assure the integrity of the sample because at the end this polymer is burned during the TT, so the external appearance of the sample could be one but that a huge part of the starting material was burned and it will not present a good integrity.

In the case of ceramic charge, ***Figure 5.6.c***, loads of 70 and 75 wt. % of zirconia give relative densities inside the desired range. In this sense, combining both results the best feedstocks compositions are: F1 (20 wt. % Pluronic-75 wt. % 8Y-TZP), F2 (25 wt.% Pluronic-75 wt. % 8Y-TZP), F4 (25 wt. % Pluronic-70 wt. % 8Y-TZP), F5 (30 wt. % Pluronic-70 wt. % 8Y-TZP) and F6 (35 wt. % Pluronic-70 wt. % 8Y-TZP).

In the end two feedstock compositions were selected, F2 and F6 to be investigated in more detail. In both cases, they presented the highest relative densities of the selected compositions, also F2 was the feedstock composition used during my Bachelor's project as a result of some previous studies of composition.
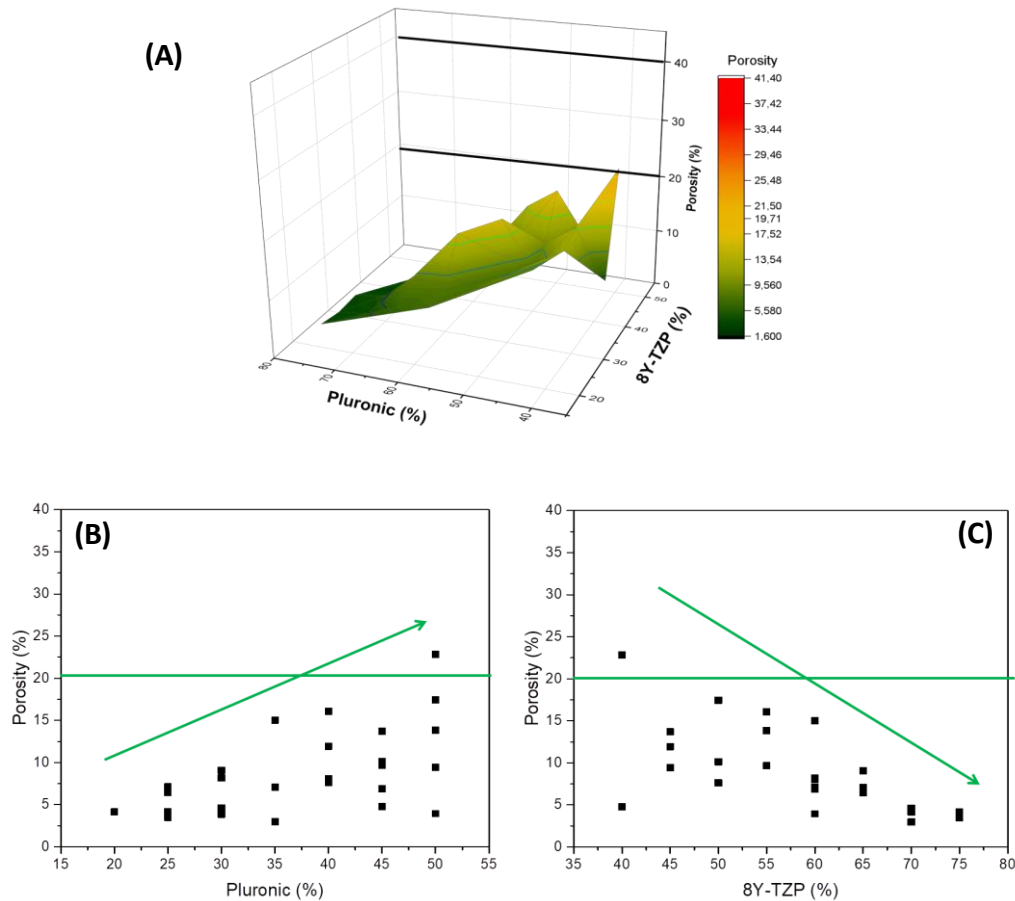


*Figure 5.7: a) Graph of the samples showing the density as a function of the Pluronic and ceramic charge content. B) Representation of the density values as a function of the Pluronic content and c) Plot representation of density values function of the 8Y-TZP content.*

Concerning porosity, the desired values for the anode and cathode may range between 20 to 40%. As shown In *Figure 5.7.a* exists a small region that accomplished this restriction. *Figures 5.7.b* and *c* clearly shows that exist a composition that presents porosity ranged between 20 and 40% (see red circle). This feedstock is composed by 50 wt. of Pluronic with 40 wt. % of ceramic load (composition F27 shown in *Table 4.1*).

To conclude this section, there is an interesting feature to comment about the density and/or porosity behaviour regarding the amount of Pluronic and ceramic charge.

***Figure 5.6.b*** is possible to observe that as much Pluronic load we add on our feedstock less relative density we achieve. By contrast in ***Figure 5.6.c*** with a higher ceramic content higher relative density value is presented. In fact, both behaviours were expected; in the case of Pluronic due to it was burned during the TT is obvious that the specimen will present higher amount of porosity. Concerning ceramic charge as much ceramic content is present in the feedstock more probability to suffer a sintering step generating good bounding between ceramic particles, again an expected behaviour.

### 5.2.2 Reology of the optimal ceramic ink

In this section the rheological properties of the different ceramics inks with the optimal compositions will be studied. ***Figure 5.8*** presents the representation of the storage modulus (G') and loss modulus (G'') as a function of the shear stress (τ). In red is represented the composition F2, in green F6 and in blue and orange F27. The difference between these two last curves is the ceramic powder used. The ink produced by Gd+8Y-TZP mixture is presented in blue, while the ceramic paste with LSGM+8Y-TZP mixture as a ceramic charge is shown in orange.
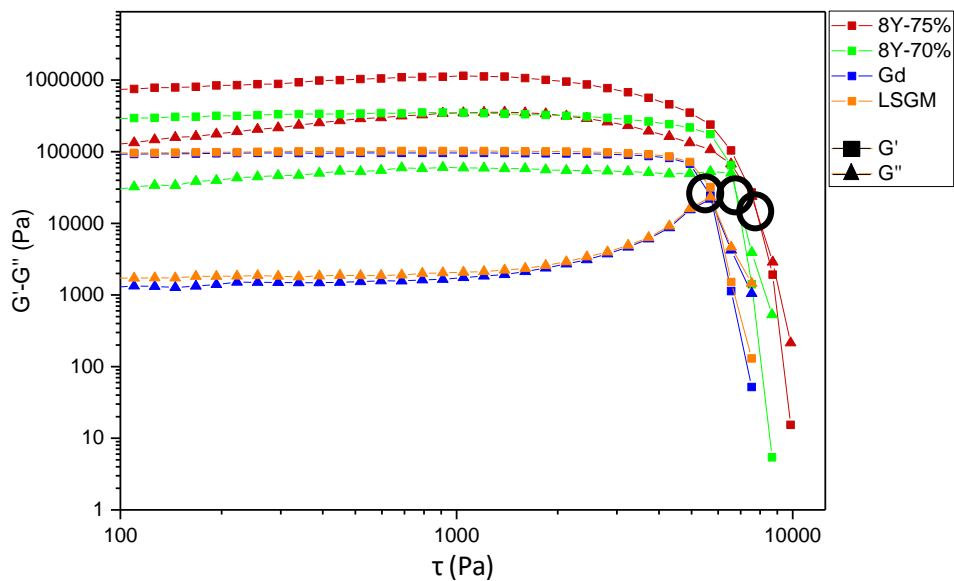


*Figure 5.8: G'-G'' representation as a function of the shear stress applied for the optimized ceramic inks. In this representation, it can be observed: in red ceramic ink with 75 wt. % of 8Y-TZP, in green ceramic ink with 70 on wt. % of 8Y-TZP, in blue ceramic ink with the mixture of Gd+8Y-TZP and finally in orange ceramic paste compound with the mixture of LSGM+8Y-TZP.*

The point where G' and G'' intersect is also called yield stress which represent the maximum shear stress to apply to ceramic ink before the properties lost. ***Table 5.1*** summarize the intersection between the *G'* and *G''* (*G' = G''*) for each ceramic paste tested.

UNIVERSITAT POLITÈCNICA DE CATALUNYA
BARCELONA**TECH**
Escola d'Enginyeria de Barcelona Est

*Table 5.1: Yield stress values for each ceramic ink with optimal composition.*

| Composition | Yield stress |
|---|---|
| **8Y – 75 wt. %** | 7794 Pa |
| **8Y – 70 wt. %** | 6758 Pa |
| **Gd – 8Y** | 5765 Pa |
| **LSGM – 8Y** | 5890 Pa |

All the ceramic pastes present the same behaviour regarding the relationship between G' and G''. The storage modulus is higher than loss modulus till both modulus cross each one with the other producing the lost of properties of the ceramic inks. Pluronic provides this behaviour, typical from shear-thickening materials as previously described in *section 4.7.1.2*.

A remarkable feature from these rheological properties is that the type of ceramic material has no any influence on these properties. We can observe that from LSGM+8Y-TZP and Gd+8Y-TZP ink, both pastes present the same amount of Pluronic and ceramic charge, with the only difference on the mixture material added to 8Y-TZP. As a result, of that an overlap of the curves and a similar yield stress values are presented as summarized in *Table 5.1*. So, the differences between feedstocks are the ones that mark the rheological properties.

It was known that with a higher amount of ceramic charge, with the same Pluronic composition, the ceramic ink presented greater values of G', G'' and as a consequence yield stress, which is traduced to more viscose materials. The same trend was presented for ceramic ink with higher Pluronic amount under the same ceramic charge. This feature is shown in *Figure 5.8* where the composition for the specimen F2, which presents the greater values. This ink is the one with the higher ceramic charge. From that an interesting conclusion can be comment; the ceramic load factor has a higher influence on rheological properties than Pluronic load. It can be seen between feedstock compositions F2 and F6. F2 has a 5% more amount of ceramic charge regarding F6, 75 wt. % in relation to 70 wt. % of 8Y-TZP. But F6 presents a 10% more of Pluronic load than F2, 35% on wt. concerning 25% on wt of Pluronic. Even so the feedstock with greater rheological properties is feedstock 2.

**UNIVERSITAT POLITÈCNICA DE CATALUNYA**
BARCELONA**TECH**
Escola d'Enginyeria de Barcelona Est

## 5.3    3D printed specimens with the optimal composition

### 5.3.1 Microstructural properties

In this section some microstructural features like density, shrinkage of the tubular samples or microstructure. In **Table 5.2** the presented compositions for each sample are referred to **Table 4.1**. Regarding the calculated relative densities, the theoretical densities were the following; 8Y-TZP = 5.9 g/cm$^3$ [51]; LSGM+8YTZP = 6.08 g/cm$^3$, value calculated from the *Law of mixtures,* **equation 20**

$X = \sum ph_i \cdot X_i, where\ X\ is\ the\ property\ to\ be\ calculated.$ 　　　　　**Equation20**

$\rho = \sum ph_i \cdot \rho_i \rightarrow \rho_{LSGM+8Y-TZP} = 0.6 \cdot 6.2 + 0.4 \cdot 5.9 = 6.08\ g/cm^3$), LSGM density [52] .

Finally, the shrinkage was calculated from the shrinkage that the diameter of tubular samples suffers during the TT. The initial value of the outer and inner diameter were held constant and equals to 10 and 5 mm, respectively.

*Table 5.2: Summary of the main microstructural properties (optimal composition, density values and shrinkage).*

| Sample | Material | Composition | ρ (g/cm$^3$) | ρ/ρ$_T$ (%) | Shrinkage |
|--------|----------|-------------|-----------|-----------|-----------|
| **A** | 8Y-TZP | F2 | 5.82 | 98.78 % | 43.25% |
| **B** | 8Y-TZP | F2 | 5.83 | 98.76 % | 40.30% |
| **C** | 8Y-TZP | F6 | 5.75 | 97.44 % | 46.38% |
| **D** | 8Y-TZP | F6 | 5.70 | 96.61 % | 48.58% |
| **E** | LSGM+8Y-TZP | F27 | 5.32 | 87.50 % | 64.13% |
| **F** | LSGM+8Y-TZP | F27 | 5.21 | 85.69 % | 62.27% |

Samples A, B, C and D, present relative densities higher than 95%, minimum value fixed to decide if the feedstock composition is correct for the desired application. Regarding shrinkage all of them suffer shrinkages between 40-50%, expected values for samples manufactured by robocasting and then sintered.  In **table 5.2** we can see that the higher amount of Pluronic load in samples C and D results in a reduction of density which it means a higher shrinkage. This feature is due to the fact that Pluronic is burned during thermal treatment.

Samples E and F present a relative density a bit higher than the one expected for these samples. The idea was to generated samples with porosity of 20 to 40%, which results in relative density between

80 to 60%. It is important to remark that the density values calculated from *Archimedes' test* does not take in account internal and closed porosity and this feature can generate a difference between density and porosity. With regard to shrinkage this samples suffer a greater shrinkage, because of the same reason explained for samples C and D and related to the amount of Pluronic.

In **Figure 5.9**, some FESEM micrographies of sample A and E are shown, with the aim to compare the microstructure of the monophasic 8Y-TZP regarding to a biphasic microstructure, LSGM+8YTZP. From **Figure 5.9.b** highlights that exist 2 phases one light gray and the other one dark. Probably the light coloured one is the LSGM, because is the one with the greater amount of powder with respect to 8Y-TZP. Also, it is clearly evident that in **Figure 5.9.b** a homogenous microstructure is evident.
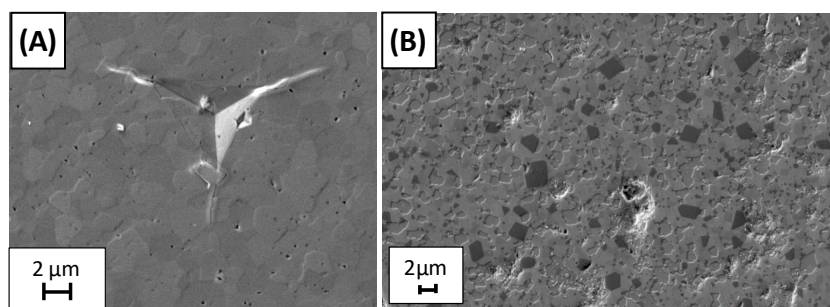


*Figure 5.9: FESEM micrograph a) 8Y-TZP sample with a 75 wt. % of ceramic charge, sample A and b) LSGM+8Y-TZP microstructure from sample E.*

### 5.3.2 Micromechanical properties

In this part the micromechanical behaviour of the 3D printed samples with the optimal feedstock composition will be shown. It is important to remark that although SOFCs do not suffer external mechanical stresses during their life in service, it is important to ensure the mechanical integrity of the stack. It is for this reason that an evaluation of the mechanical properties is a mandatory step to do.

The experimental results will be compared with the literature values from **Table 5.3**. The values of 8Y-TZP were reported from Ref. [53]. On the other hand, the LSGM values were directly extracted Ref. [52]. The last values of $H$ and $E$ were found from apply the *Law of Mixtures*, presented in **equation 20**.

In **Figure 5.10** the results of nanoindentations are presented. The plot of Hardness, in black, and Elastic modulus, in blue, as a function of the displacement into the surface are represented. **Figure 5.10.a, b** and **c** are referred to sample A, C and E, respectively.

***Table 5.3:*** *Reference values of mechanical properties, H and E, from each material of printed samples.*

| Material | Elastic modulus | Hardness |
|---|---|---|
| **8Y-TZP [53]** | 269 GPa | 18.5 GPa |
| **LSGM [52]** | 249 GPa | 12.3 GPa |
| **LSGM + 8Y-TZP** | 264 GPa | 14.8 GPa |
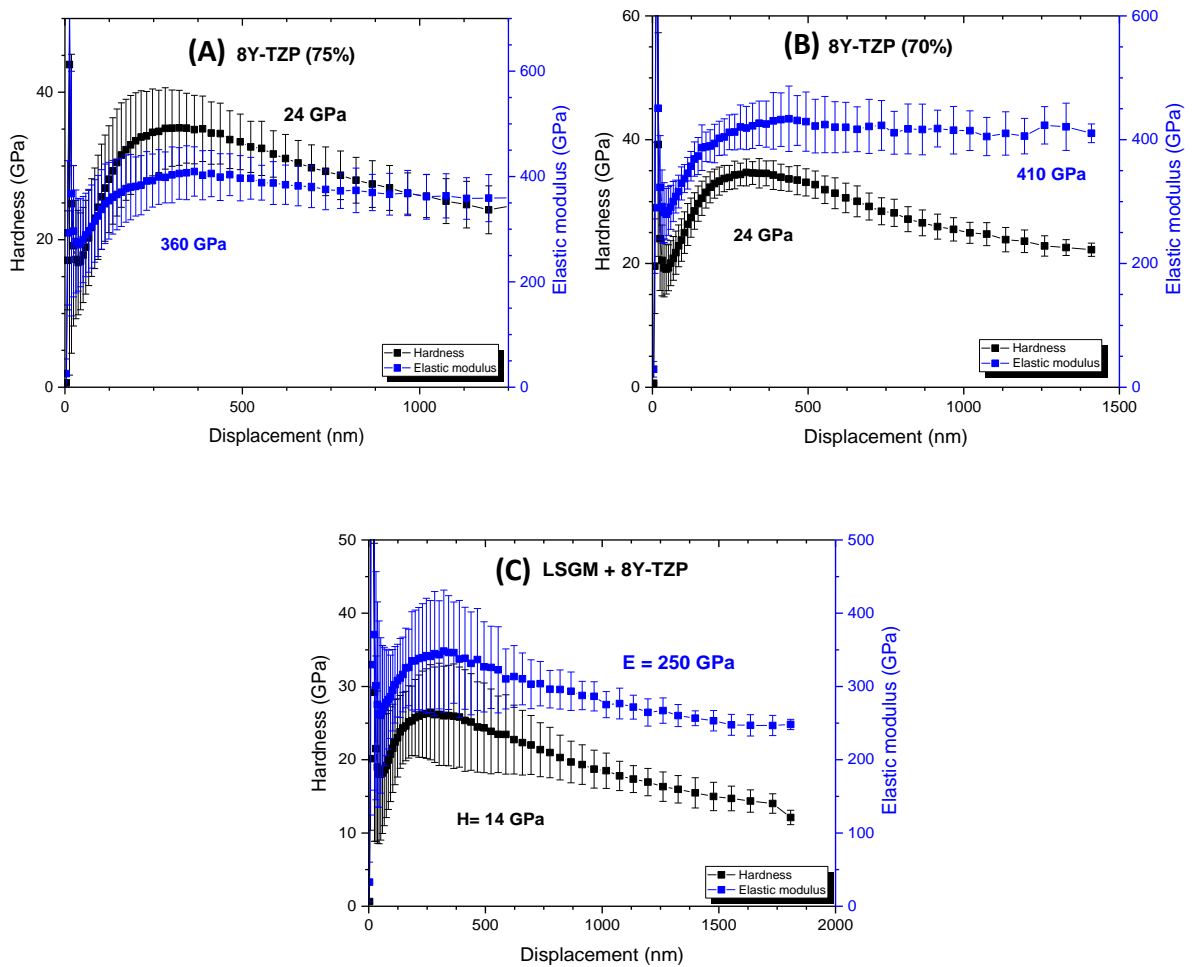


***Figure 5.10:*** *Nanoindentation results, Hardness and Elastic modulus representation as a function of the displacement into the surface. a) Sample A, b) Sample C and c) Sample E.*

Regarding zirconia samples there is not much difference between both feedstock compositions. In both cases they present a hardness of around 24 GPa for penetration depths higher than 1000 nm, where this parameters remains stable. Regarding the elastic modulus; sample A, ***Figure 5.10.a,*** shows a value of 360 GPa. For sample C, ***Figure 5.10.b***, the elastic modulus value is around 410 GPa. If we

compare these results with the ones of the literature, **Table 5.3**, both mechanical properties are quit high.

Concerning the elastic modulus this discrepancy could be attributed to the fact that Oliver and Pharr's original method based on Sneddon's analysis of elastic contact, as employed here, does not take into account the lateral stresses generated during the indentation process, which leads to an overestimation of the Young's modulus through the β parameter [54], **equation 9**.

On the other hand, the discrepancy between experimental and literature values of hardness can be explained by two reasons. The first one involes the deformation mechanism of *c*-phase which implies the nucleation and movement of dislocations. In this case if the indentation generates enough dislocations the material can be saturated of them producing an increase of the hardness [55]. The other reason cames from the anysotropy that zirconia *c*-phase presents as found in Ref. [56], where this anisotropic behavior is demostrated, showing that depending of deformation behaviour, elastic or elasto-plastic, and the direction of the *c*- grains, both hardness and elastic modulus present sustantial differences.

These results show us that a deeper study of the mechanical behaviour, regarding dislocation nucleation and movement with the anistropic affectation is needed. Even though the application pressented in this Matser's project is not in regard with a mechanical application. SOFC parts only need to assure a minimal mechanical integrity to avoid the failure of the stack due to this reason.

### 5.3.3 Damage mechanisms

During this section the damage mechanisms generated during the nanoindentation process will be presented. **Figure 5.11.a-b** show the residual print of the indentation result of the elasto-plastic deformation, for sample A and E respectively.
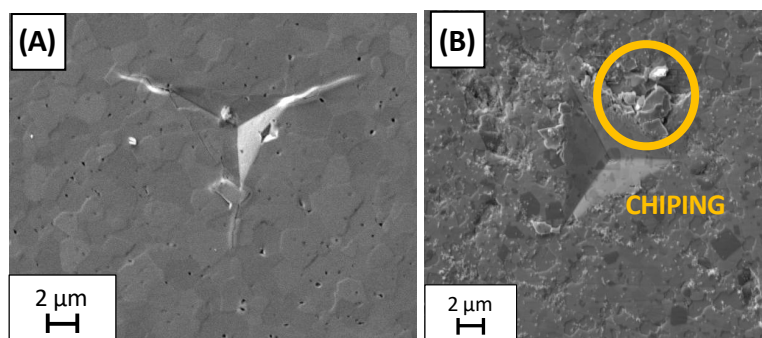


*Figure 5.11: FESEM micrographs of nanoindentation imprints for a) Sample A and b) Sample E.*

8Y-TZP is a fragile material which it means that during the nanoindentation process will present an imprint with some radial cracks at the corners of the residual print and pile-ups around the residual

UNIVERSITAT POLITÈCNICA DE CATALUNYA
BARCELONA**TECH**
Escola d'Enginyeria de Barcelona Est

imprint. It can be explained because *c-* zirconia phase, the one presented with the 8Y-TZP, impedes the martensitic phase transformation, the typical deformation process of *t-* zirconia phase, so in this case the deformation of this *c*-phase is governed by dislocation nucleation and movement. This generation of cracks and pile-up is explained by the deformation field induced by all the pile-up of dislocations present under the residual imprint [55]. In ***Figure 5.11.a*** some cracks at the corner of the residual imprint can be clearly observed. On the other hand, no pile-up effect is evident. Due to the use of Berkovich tip, lower stresses were generated which it means lower dislocation densities is available at the vicinity of the residual imprint, yielding less opportunity to reach the surface.

Regarding LSGM with 8Y-TZP, this majority phase of LSGM makes the resulting material softer than 8Y-TZP, fact that can be observed in ***Table 5.3***. Concerning damage generated during nanoindentation process the use of a Berkovich tip indenter is enough to generate damage in the sample creating some pile-up as a result of the dislocation activation and propagation until reaching the surface, ***Figure 5.11.b***.

In order to quantify the pile-up effect induced in sample E, an AFM observation was done. ***Figure 5.12.a*** shows the 3D representation of the residual imprint, where a clearly pile-up is evident at the vicinity of the residual imprint. In order to quantify the height of this pile-up a topographic profile of the residual imprint was conducted yielding a maximum pile-up of around 200 nm as shown in ***Figure 5.12.b***. A FIB cross-section of the observed zone by AFM is conducted in order to get a deeper knowledge about the fracture mechanisms, ***Figure 5.12.c***.
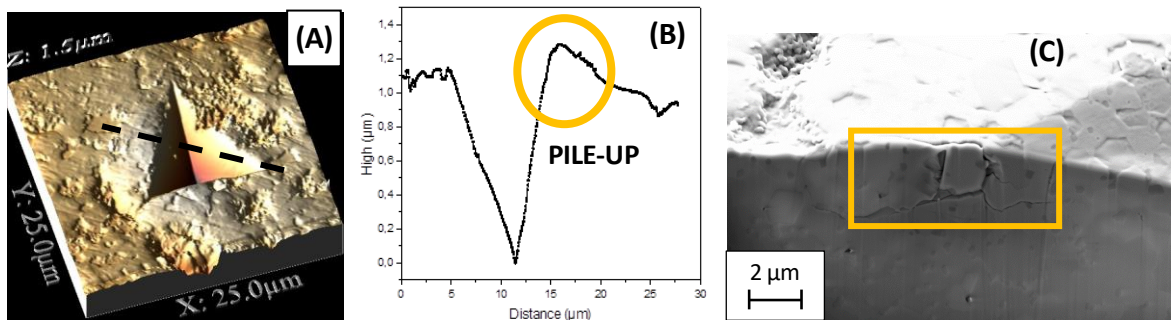


*Figure 5.12: a) 3D-representation of the AFM topographic image of an imprint conducted under displacement control mode from sample E. b) Topographic profile of the nanoindentation imprint (see white line dash in **Figure 5.12.a**) and c) FIB cross-section image of the section part of the pile generated during the nanoindentation process.*

A pile-up is generated when during the indentation processes the stress that feels the material is higher and any crack achieve the critical crack size to start to propagate through the material. This crack usually is generated on the sample surface and the way it propagates inside the material an creating a pile-up; if this crack emerges until reaching the surface a chipping phenomenon takes

place. This can be observed on a SEM micrograph and studied by AFM technique which leads to generatea topographic profile of the residual indentation where the pile-up can be clearly identify as a pick with reference of surface level, *Figure 5.12.b*.

Thanks to FIB cross-section we can define if the crack induced during the indentation process is intergranular, which it means that it is propagated inside the grains or the crack is transgranular which it means that it is moved through the grains by the grain boundary. *Figure 5.12.c* shows that the crack is intergranular. It makes sense the *c*-phase is a phase with a really high values of hardness, which it means that for the crack propagation implies less energy the movement through grain boundary instead of try to move above a really hard crystalline structure.

# 6. Environmental impact analysis

In general terms, in this Master's project, the environmental impact is related to the materials used to prepare the sample and during the processing process as well as the energy associated to perform the T.T., the powder processing step, polishing the specimens and the different machines employed to microstructural and mechanically characterize the material.

If we talk about the materials used during the process zirconia do not have a high harm for the environment, but LSGM and Gd are hazard for water, due to they are rare earth.  During the powder processing step, there were a lost of 5% of powder, inherent effect of the process. Nevertheless, we try to carry out the correct separation and management of waste, such as ethanol with ceramic particles or particles adhered to the sieve, to reduce as much as possible the environmental impact of the ceramic powder that is lost during processing. Referred to ceramic pastes preparation, all the material was try to be used in order to avoid the generation of waste and leftover products, always trying to make small amounts of ceramic paste.

As far as the processing process, the printing material; syringe, piston and nozzle, during all the process was reused as far as possible, instead of using it as a disposable material. One of the environmental problems was the use of the furnace that has huge energy consumption. Another one was the powder processing step. Apart from generated wastes, talked previously, consuming time of the machines are relative high, which means a high consumption rate of energy. The polishing process also presents an environmental impact. During it many water was used, and the grind paper to polish was to use and throw away. It was generated some waste products, but they were recycled on the correct way.

Finally, when we talk about the characterization process, electrical energy was consumed, but in comparison with the energy used for preparation sample steps, it is not comparable in terms of consume

UNIVERSITAT POLITÈCNICA DE CATALUNYA
BARCELONA**TECH**
Escola d'Enginyeria de Barcelona Est

# Conclusions

The results of this Matser's project draw the following conclusions:

**(1) In terms of feedstock properties:**

Regarding **powder size** we observed that thanks to apply the processing process (chemical processing + sieve) we are able to reduce the particle size to be able to use a nozzle with a *diameter of 250 µm*, which implies an improvement of the resolution of the stack.
All of the ceramic powder for each part, 8Y-TZP, LSGM and Gd, for electrolyte, cathode and anode respectively, suffer a reduction of the size presenting a size distribution peak below *45 µm*, sieve size. In addition, seeing the SEM micrographs, all the powders used present a spherical shape, in the case of LSGM and Gd, we achieve that thanks to process the powder on a chemical way with 8Y-TZP.

From **composition** point of view, 27 different compositions were tried, at the end only 3 optimal compositions were selected to study rheological properties and to try to print each part of a SOFC separately.
- For electrolyte part, two compositions were selected as the optimal ones: F2 with a 25 wt. % of Pluronic with 75 wt. % of 8Y-TZP and F6 with a 35 wt. % with a ceramic charge of 70 wt. % of 8Y-TZP.
- For electrodes parts only one composition was in the limitation marked, a porosity between 20 to 40%. This feedstock composition was F27 with a 50 wt. % of Pluronic added 40 wt. % of ceramic charge.

With the optimal composition the **rheological properties** were studied. From these results it is possible to conclude that the material has not have an affectation on rheology behaviour, because LSGM ink and Gd ink that present the same feedstock composition has the same *G'* and *G''* curves. Another thing to highlight is that as much Pluronic and ceramic load is added to ceramic ink higher yield stress and values of *G'* and *G''* are presented. Even though the affectation of Pluronic load is less influent than the amount of ceramic powder added. Finally, we observed for all the ceramic ink a shear thickening behaviour something expected due to the use of Pluronic as the polymer to prepare the hydrogel.

**(2) Final samples properties:**

UNIVERSITAT POLITÈCNICA DE CATALUNYA
BARCELONATECH
Escola d'Enginyeria de Barcelona Est

Two samples were printed for each optimal composition. Concerning Gd samples we were not able to print them due to some issues during sintering step, so at the end were only studied 6 samples instead of 8.

From **microstructural properties** the values of porosity and shrinkage present a correlation with the Pluronic charge for each sample:

- Samples A and B the ones with les Pluronic load (25 wt. %) are the ones with highest density (> 98%) and the lowest shrinkage (40-43%).
- Samples C and D with higher amount of Pluronic (35 wt. %) present a density ≈ 97% and a higher shrinkage (46-48%).
- Samples E and F with the highest Pluronic load (50 wt. %) and the lowest ceramic charge (40 wt. %) are the samples with the lowest density (85-87%) with the highest shrinkage (62-64%).

Even though we are taking the porosity value as the difference between 100 and the relative density to make a first triage of feedstock composition, doing that samples E and F present a lower porosity than 20%. As it said more essays to study the porosity, like Micro-CT, need to be done, due to importance of this parameter for electronic conductivity in electrode parts.

Regarding the obtained microstructure, we can observe in sample E a biphasic microstructure something expected because it ceramic load is a mixture of LSGM + 8Y-TZP.

From a **mechanical** point of view these are the behaviours were presented:

- For 8Y-TZP samples, for both compositions the Hardness was of 24 GPa, and the Elastic modulus for samples with F2 was 360 GPa and for samples with F6 was 400 GPa. In both cases values are significantly higher, around 33% more, than the ones reported from the bibliography.
- For LSGM + 8Y-TZP samples present a hardness of 14 GPa. Regarding Elastic modulus, these samples present a value of 250 GPa lower that the one expected (264 GPa) due to the porous nature of these samples.

If we try to decide between the electrolytes compositions, we are not able to have a final decision. Because although the samples with a feedstock composition F6 presents a better elastic modulus value, the other composition gives us the highest density with the lowest shrinkage and mechanical properties slightly lower than the other composition. So, we recommend to try both composition when processing the entire SOFC.

UNIVERSITAT POLITÈCNICA DE CATALUNYA
BARCELONATECH
UPC    Escola d'Enginyeria de Barcelona Est

Regarding the **damage** generated to sample E during nanoindentation, it is possible to concluded that due to the lower hardness of LSGM the material suffer damage during the indentation process generating a pile-up effect around the imprint. This event is consequence of a intergranular crack propagation as depicted the FIB cross-section in this particular region.

Retaking *Figure 3.1* where was exposed all the features to control during an Additive manufacturing process for a SOFC, *Figure A* presents this scheme actualized to show graphically what we achieve during this Master's project, and what is still pending to develop as a future work.
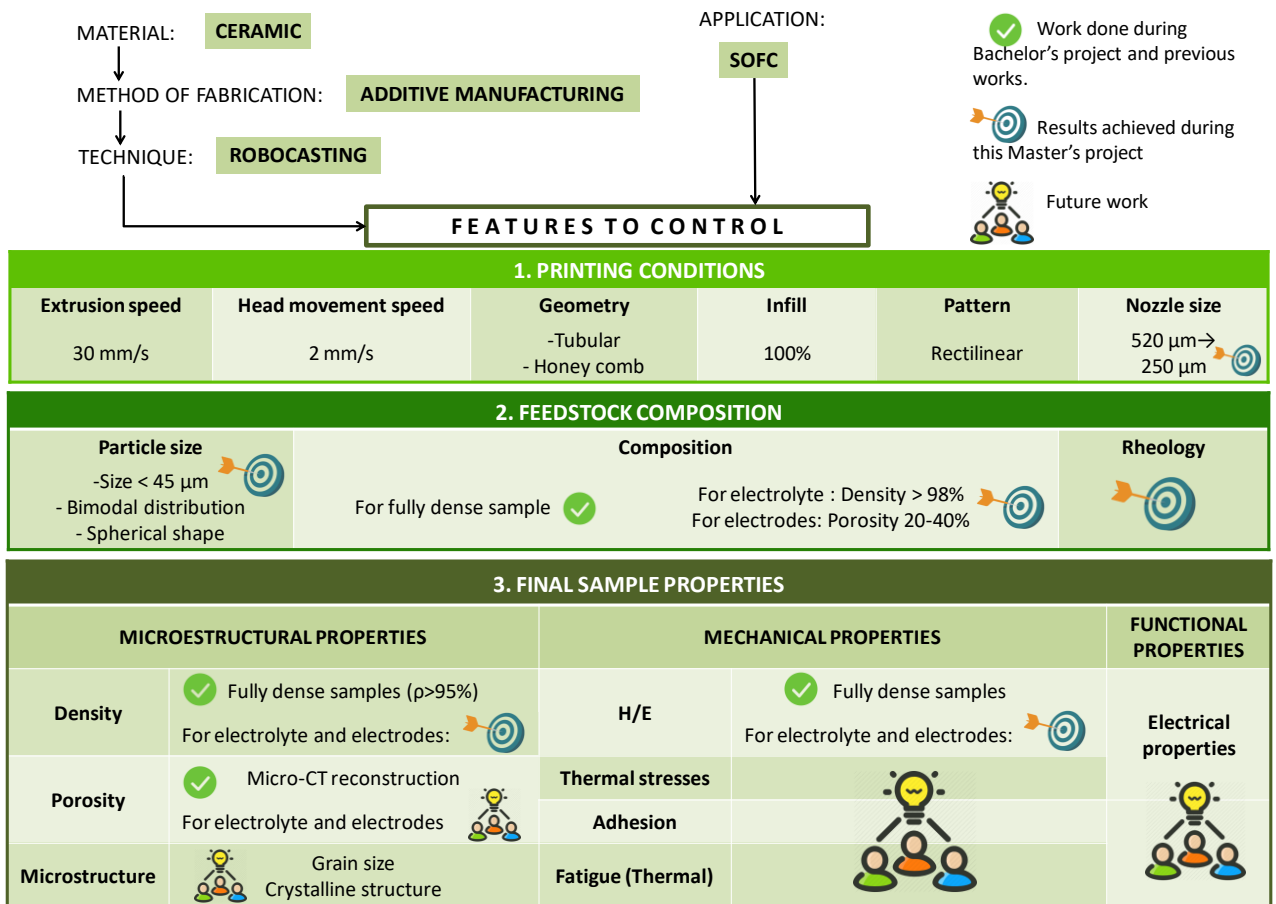


*Figure A:* *Schematic representation of the features to control during a 3D printing process of SOFC. This update version of* ***Figure 3.1*** *highlights the results achived during the Master's project.*

# Future work

After this Master's project and as it is mentioned during all the work, this project represents a puzzle piece to achieve the **long term goal** which is to be able to develop a systematic protocol to print solid oxide fuel cells (SOFC) with complex shapes with at least the same microstructural, mechanical and electrical properties as for the manufactured SOFC by the conventional processing routes.

Print relative complex, like honeycomb or tubular were attained as a result from my Bachelor's project. From this Master's project, we see that is possible to be able to control the porosity through the modification of feedstock. In addition, the optimal composition for each part was obtained.

From these results some challenges appear to succeed in our **long term goal:**

i. *Be able to sinter some additive manufactured samples based on Gadolinium powder.*
ii. *Print all parts together on a tubular SOFC, supported on the electrolyte. Which it means to define the steps to follow on the printing and sintering processes.*
iii. *Make a complete characterization of the printed SOFC; mechanical characterization (study the adhesion between parts, the thermal fatigue and the values of Hardness and Elastic modulus), as well as an electrical characterization (study of the electrical impedance and ionic conductivity). All of that with the aim to find a correlation between mechanical and electrical properties, to try to response the following question; is this SOFC functional?*

UNIVERSITAT POLITÈCNICA DE CATALUNYA
BARCELONATECH
Escola d'Enginyeria de Barcelona Est

# Budget and financial analysis

***Table 7.1:*** *Summary of the consumables employed in this Master's project.*

| CONSUMABLES | | | |
|---|---|---|---|
| **PRODUCT** | **QUANTITY** | **COST/UD.** | **COST** |
| **Pluronic F-127** | 0.20 Kg | 190 €/Kg | 38 € |
| **8Y-TZP** | 0.3 Kg | 125 €/Kg | 62.5 € |
| **LSM** | 0.04 Kg | 4.9 €/g | 196 € |
| **Gadolinium (III)** | 0.04 Kg | 145€/100g | 58 € |
| **Distilled water** | 1l | 0.7 €/Kg | 0.70 € |
| **Grinding paper P80** | 3 | 0.8 €/un. | 2.40 € |
| **Grinding paper P240** | 3 | 0.8 €/un. | 2.40 € |
| **Grinding paper P400** | 5 | 0.8 €/un. | 4 € |
| **Grinding paper P600** | 5 | 0.8 €/un. | 4 € |
| **Grinding paper P1200** | 3 | 0.8 €/un. | 2.40 € |
| **Cloth MD-Dac** | 2 | 53 €/un. | 106 € |
| **Cloth MD-Nap** | 1 | 75 €/un. | 75 € |
| **Diamond suspension 6µm** | 0.1 L | 83 €/L | 8.30 € |
| **Diamond suspension 3µm** | 0.1 L | 75 €/L | 7.50 € |
| **Colloidal silica suspension** | 0.1 L | 150 €/L | 15 € |
| **Epoxy resin** | 0.1 L | 11.16 €/L | 1.12 € |
| **Ethanol** | 3 L | 8€/L | 24 € |
| **SUBTOTAL:** | | | **607.32 €** |

UNIVERSITAT POLITÈCNICA DE CATALUNYA
BARCELONA**TECH**
Escola d'Enginyeria de Barcelona Est

*Table 7.2: Summary of the equipment employed in this Master's project.*

| EQUIPMENT | | | |
|---|---|---|---|
| **CONCEPT** | **QUANTITY** | **COST/UD.** | **COST** |
| **Balance** | 5 h | 10.3 €/h | 51.50 € |
| **SpeedMixer** | 5 h | 5 €/h | 25 € |
| **3D Printer** | 80 h | 12.4 €/h | 992 € |
| **Nabathern Furnace** | 90 h | 12.4 €/h | 1116 € |
| **Turbula** | 72 h | 5€/h | 360 € |
| **Rotavapor** | 15 h | 10€/h | 150 € |
| **Sheeve** | 60 h | 8.85 €/h | 531 € |
| **Polisher LaboPol-5** | 5 h | 20 €/h | 100 € |
| **Nanoidenter** | 10 h | 60 €/h | 600 € |
| **SEM-FIB** | 10h | 106.74 €/h | 1067.40 € |
| **AFM** | 2 h | 23.75 €/h | 47.50 € |
| **MasterSizer** | 3 h | 20€/h | 60 € |
| **Rehometer** | 4 h | 23 €/h | 92 € |
| **Magnify lent** | 2 h | 7 €/h | 14 € |
| **SUBTOTAL:** | | | **5206.4 €** |

UNIVERSITAT POLITÈCNICA DE CATALUNYA
BARCELONA**TECH**
Escola d'Enginyeria de Barcelona Est

*Table 7.3: Summary of the personal costs employed to conduct this Master's project.*

### COST OF SUPPORT ENGINEERING

| CONCEPT | QUANTITY | COST/UD. | COST |
|---|---|---|---|
| Support technician | 10 h | 40 €/h | 400 € |
| Supervisor | 20 h | 50 €/h | 1000 € |
| SUBTOTAL: | | | 1400 € |

*Table 7.4: Summary of the cost of engineering by the designer.*

### COST OF ENGINEERING BY THE DESIGNER

| CONCEPT | QUANTITY | COST/UD. | COST |
|---|---|---|---|
| Sample preparation | 110 h | 24.8 €/h | 2728 € |
| Sample Characterization | 41 h | 24.8 €/h | 892.8 |
| Search for information | 60 h | 24.8 €/h | 1488 |
| Analysis results | 30 h | 24.8 €/h | 744 € |
| Memory development | 100 h | 24.8 €/h | 2480 € |
| SUBTOTAL: | | | 8332.80 € |

UNIVERSITAT POLITÈCNICA DE CATALUNYA
BARCELONATECH
Escola d'Enginyeria de Barcelona Est

***Table 7.5:*** *Summary table of the total cost of the project.*

| TOTAL COST OF THE PROJECT | |
|---|---|
| **CONCEPT** | **COST** |
| **Total cost associated with consumables** | 607.32 € |
| **Total cost associated with the sample characterisation** | 5206.4 € |
| **Total cost associated with the engineering** | 8332.80 € |
| **Total cost associated with support engineering** | 1400 € |
| **TOTAL:** | 15546.52€ |
| **IVA (21 %):** | 3264.77 € |
| **TOTAL + IVA:** | **18811.29 €** |

UNIVERSITAT POLITÈCNICA DE CATALUNYA
BARCELONATECH
Escola d'Enginyeria de Barcelona Est

# Bibliography

[1]   «ISO / ASTM52900-15, Standard Terminology for Additive Manufacturing – General Principles – Terminology, ASTM International, West Conshohocken, PA, 2015, www.astm.org».

[2]   K. S. Prakash, et al., «Additive Manufacturing Techniques in Manufacturing – An Overview,» *Materials Today: Proceedings,* vol. 5, pp. 3873-3882, 2018.

[3]   J.W.Halloran, et al., «Photo polymerization of powder suspensions for shaping ceramics,» *Journal of the European Ceramic Society,* vol. 31, pp. 2613-2616, 2011.

[4]   S. Bose, et al., «Additive Manufacturing of Biomaterials,» *Progress in Materials Science,* vol. 93, pp. 45-111, 2018.

[5]   R. Singh, A. Gupta, O. Tripathi, et al., «Powder bed fusion process in additive manufacturing: An overview», *Materials Today: Proceedings*, https://doi.org/10.1016/j.matpr.2020.02.635 (Article in press).

[6]   T.D.Ngo, et al., «Additive manufacturing (3D printing): A review of materials, methods, applications and challenges.,» *Composites Part B,* vol. 143, pp. 172-196, 2018.

[7]   D. Vyas and D. Udyawar, "A Review on Current State of Art of Bioprinting," in *3D Printing and Additive Manufacturing Technologies*, SpringerLink e-books, 2019.

[8]   L. J. Kumar and C. K. Nair, "Current Trends of Additive Manufacturing in the Aerospace Industry," in *Advances in 3D Printing & Additive Manufacturing Technologies*, SpringerLinks e-books, 2017.

[9]   "Additive manufacturing Takes Off in Aerospace Industry," Assembly, [Online]. Available: https://www.assemblymag.com/articles/93176-additive-manufacturing-takes-off-in-aerospace-industry. [Accessed 04 04 2020].

[10] A. Bandyopadhyay, et al., "Additive manufacturing of multi-material structures," *Materials Science and Engineering: R: Report,* vol. 129, pp. 1-16, 2018.

[11] S. Masciandaro, et al., "Three-dimensional printed yttria-stabilized zirconia self-supported electrolytes for solid oxide fuel cell applications," *Journal of the European Ceramic Society,* vol. 39, pp. 9-16, 2019.

[12] T. Malkow, "SOFC in Brief," in *Modeling Oxide Fuel Cells*, SpringerLink e-book, 2008.

[13] Z.Shao and M. O. Tadé, Intermediate-Temperature Solid Oxide Fuel Cells, SpringerLink e-books, 2016.

[14] N. Q. Minh, Science and technology of ceramic fuel cells, Elsevier, 1995.

[15] I. B. Celik and S. R. Pakalapati, "From a Single Cell to a Stack Modeling," in *Modeling Solid Oxide Fuel Cells*, SpringerLink e-books, 2008.

[16] H. Liu, et al., "Electrochemical performances of spinel oxides as cathodes for intermediate temperature solid oxide fuel cells," *International Journal of Hydrogen Energy,* vol. 38, pp. 1052-1057, 2013.

[17] H. Geng, et al., "Sustained release of VEGF from PLGA nanoparticles embedded thermo-sensitive hydrogel in full-thickness porcine bladder acellular matrix," *Nanoscale Research Letters,* vol. 6, p. 312, 2011.

[18] M. S. H. Akash, et al., «Natural and Synthetic Polymers as Drug Carriers for Delivery of Therapeutic Proteins,» *Polymers Reviews,* vol. 6, pp. 371-406, 2015.

[19] Y. Maazouz, et al., «Self-hardening and thermoresponsive alpha tricalcium phosphate/pluronic pastes,» *Acta Biomaterialia,* vol. 49, pp. 563-574, 2017.

[20] J. Chevalier, et al., "What Future of Zirconia as a Biomaterial?," *Biomaterials,* vol. 27, pp. 535-543, 2006.

[21] R. Hannink, et al., "Transformation Toughening in Zirconia-Containing Ceramics," *Journal of American Ceramic Society,* vol. 83, pp. 461-487, 2000.

[22] N. Gupta, et al., «Y-TZP ceramics with optimized toughness: new results,» *Journal of Alloys and Compounds,* vol. 379, pp. 228-232, 2004.

[23] I. Žma, et al., «Hardness and Indentation Fracture Toughness of Slip Cast Alumina and Alumina-Zirconia Ceramics,» *Materials,* vol. 13, pp. 1-17, 2020.

[24] M. Bucko, "Microstructural Aspects of Ionic Conductivity in Nanocrystalline Zirconia," in *Handbook of Nanoelectrochemistry*, SpringerLink e-books, 2016.

UNIVERSITAT POLITÈCNICA DE CATALUNYA
BARCELONATECH
Escola d'Enginyeria de Barcelona Est

[25] T. Kawada, "Perovskite Oxide for Cathode of SOFCs," in *Perovskite Oxide for Solid Oxide Fuel Cells*, SpringerLink e-books, 2009.

[26] S. Shaikh, et al., "A review on the selection of anode materials for solid-oxide fuel cells," *Renewable and Sustainable Energy Reviews,* vol. 51, pp. 1-8, 2015.

[27] J. C. Ruiz-Morales, et al., "Performance of a novel type of electrolyte-supported solid oxide fuel cell with honeycomb structure," *Journal of Power Sources,* vol. 195, pp. 516-521, 2010.

[28] E. Feilden, et al., «Robocasting of structural ceramic parts with hydrogel inks,» *Journal of the European Ceramic Society,* vol. 36, pp. 2525-2533, 2016.

[29] Y. Fernández, et al., «Guia del Usuario – P1503023 – UPC – BCN3D+ Dual Paste», Fundació CIM (BarcelonaTech) (2015).

[30] J. Chevalier, et al., «Critical effect of cubic phase on aging in 3mol% yttria-stabilized zirconia ceramics for hip replacement prosthesis,» *Biomaterials,* vol. 25, p. 5539–5545, 2004.

[31] K. Raghvendra, et al., «Electrical conductivity of LSGM–YSZ composite materials,» *Journal of Materials Science,* vol. 49, p. 5571–5578, 2014.

[32] "Mastersizer 3000 smarter particle sizing (brochure)," Malvern, [Online]. Available: https://www.malvernpanalytical.com/en/products/product-range/mastersizer-range/mastersizer-3000. [Accessed 15 05 2020].

[33] G. B. J. d. Boer, et al., "Laser Diffraction Spectrometry: Fraunhofer Diffraction Versus Mie Scattering," *Particle Characterization,* vol. 4, pp. 14-19, 1987.

[34] J. Goldstein, D. E. Newbury, J. R. Michael, N. W. M. Ritchie, J. H. Scott and D. C. Joy, Scanning Electron Microscopy and X-Ray Microanalysis, SpringerLink ebooks, 2018.

[35] H. Yao, *FORMATEX-Modern Research and Educational Topics in Microscopy,* Barcelona: PhD Thesis, School of Materials Science, UPC University, 2013.

[36] B. S. Majumdar, *FE-SEM Principle,* New Mexico, US: New Mexico Tech-Materials Department, 2009.

[37] R. Moreno, "Rheology," in *Encyclopedia of Materials: Science and Technology*, Elsevier, 2001.

UNIVERSITAT POLITÈCNICA DE CATALUNYA
BARCELONA**TECH**
Escola d'Enginyeria de Barcelona Est

[38] R. O'Neill, et al., "Critical review: injectability of calcium phosphate pastes and cements," *Acta biomaterialia,* vol. 50, pp. 1-19, 2017.

[39] "Basics of rheology," Anton Paar, [Online]. Available: https://wiki.anton-paar.com/en/basics-of-rheology/#definition-of-terms-shear-stress-shear-rate-law-of-viscosity-kinematic-viscosity. [Accessed 14 05 2020].

[40] E. Broitman, et al., "Indentation Hardness Measurements at Macro-, Micro-, and Nanoscale: A critical overview," *Tribology Letters,* vol. 65, pp. 1-18, 2017.

[41] W. C. Oliver and G. M. Phar, "An improved technique for determining hardness and elastic modulus using load and displacement sensing indentation experiments," *Journal of Materials Research,* vol. 7, pp. 1564-1583, 1992.

[42] W. C. Oliver and G. M. Phar, "Measurement of hardness and elastic modulus by instrumented indentation: Advances in understanding and refinements to methodology," *Journal of Materials Research,* vol. 19, pp. 3-20, 2004.

[43] "Nanoidenter Tip," Surface-Tec, [Online]. Available: http://www.surface-tec.com/nanotips.php. [Accessed 30 05 2020].

[44] J. J. Roa, et al., "Mechanical characterization at Nanometric Scale of Ceramic Superconductor Composites," in *Nanotechnology: Nanofabrication, Pattering and Self Assembly*, Nova Science Publishers, 2011.

[45] J. J. Roa, et al., «Nanohardness and Young's modulus of YBCO samples textured by the Bridgman technique,» *Nanotechnology,* vol. 18, pp. 385701-385706, 2007.

[46] R. A. Wilson i H. A. Bullen, *Introduction to Scanning Probe Microscopy (SPM): Basic Theory Atomic Force Microscopy (AFM),* Creative Commons Attribution-Noncomercial-Share Alike, 2006.

[47] L. Lianquing, "Chapter4 - Atomic Force Microscope-Based Nanorobotic system for Nanoassembly," in *Nano Optoelectronic Sensors and Devices*, Oxford, 2012.

[48] P. R. Munroe, et al., "The application of focused ion beam microscopy in the material sciences," *Materials characterization,* vol. 60, pp. 2-13, 2009.

UNIVERSITAT POLITÈCNICA DE CATALUNYA
BARCELONA**TECH**
Escola d'Enginyeria de Barcelona Est

[49] M. Sezen, "Focused Ion Beams (FIB) — Novel Methodologies and Recent Applications for Multidisciplinary Sciences," in *Modern Electron Microscopy in Physical and Life Sciences*, IntechOpen, 2016.

[50] L. Liu, et al., "Modeling of thermal stresses and lifetime prediction of planar solid oxide fuel cell under thermal cycling conditions," *Journal of Power Sources,* vol. 195, pp. 2310-2318, 2010.

[51] "Zirconia Brochure," Tosoh, [Online]. Available: http://www.eskens.com/wp-content/uploads/2014/05/ZIRCONIA-BROCHURE.pdf. [Accessed 13 05 2020].

[52] M. Morales, et al., "A review of doped lanthanum gallates as electrolytes for intermediate temperature solid oxides fuel cells: From materials processing to electrical and thermo-mechanical properties," *Journal of the European Ceramic Society ,* vol. 36, pp. 1-16, 2016.

[53] A. Gómez-Gómez, et al., "Improved crack resistance and thermal conductivity of cubic zirconia containing graphene nanoplatelets," *Journal of the European Ceramic Society,* vol. 40, pp. 1557-1565, 2020.

[54] Y. Gaillard, et al., "Quantification of hydrothermal degradation in zirconia by nanoindentation," *Acta Materialia,* vol. 56, pp. 4206-4216, 2008.

[55] Y. Gaillard, et al., "Nanoindentation of yttria-doped zirconia: Effect of crystallographic structure on deformation mechanisms," *Journal of Materials Reserch,* vol. 24, pp. 719-727, 2009.

[56] M. Fujikane, et al., "Nanoindentation examination of yttria-stabilized zirconia (YSZ) crystal," *Journal of Alloys and Compounds,* vol. 431, pp. 250-251, 2007.

UNIVERSITAT POLITÈCNICA DE CATALUNYA
BARCELONA**TECH**
Escola d'Enginyeria de Barcelona Est

# Annexe

## Annexe A: Data sheets

### Annexe A.1: Pluronic F-127 Sigma Aldrich

**SIGMA-ALDRICH**

*sigma-aldrich.com*

3050 Spruce Street, Saint Louis, MO 63103, USA
Website: www.sigmaaldrich.com
Email USA: techserv@sial.com
Outside USA: eurtechserv@sial.com

## Product Specification

Product Name:
Pluronic® F-127 – powder, BioReagent, suitable for cell culture

**Product Number:** P2443
CAS Number: 9003-11-6
MDL: MFCD00082049

| TEST | Specification |
|---|---|
| Appearance (Color) | White |
| Appearance (Form) | Powder |
| Solubility (Color) | Colorless |
| Solubility (Turbidity) | Clear |
| 50 mg/mL, H2O, at less than 10 deg C | |
| pH | 6.0 - 7.0 |
| (2.5% solution) | |
| Moisture Content | ≤ 0.75 % |
| Cell Culture Test | Pass |
| Recommended Retest Period | --------------------- |
| 2 Years | |
| Note | --------------------- |
| Pluronic is a registered trademark of BASF SE. | |

Specification: PRD.1.ZQ5.10000051983

**UNIVERSITAT POLITÈCNICA DE CATALUNYA**
BARCELONA**TECH**
Escola d'Enginyeria de Barcelona Est

## Annexe A.2: Zirconia Tosoh:

### Powder Characteristics and Properties

| | TZ-3Y-E (TZ-3YB-E) | TZ-3YS-E (TZ-3YSB-E) (TZ-3YSB-C) | TZ-4Y | TZ-6Y | TZ-8Y | TZ-8YS (TZ-8YSB) | TZ-10YS | TZ-3Y20A (TZ-3Y20AB) | TZ-0 |
|---|---|---|---|---|---|---|---|---|---|
| $Y_2O_3$ (mol%) | 3 | 3 | 4 | 6 | 8 | 8 | 10 | 3 | 0 |
| Actual Particle Size (μm) | 0.04 (40nm) | 0.09 (90nm) | 0.04 (40nm) | | | 0.09 (90nm) | | − | 0.04 (40nm) |

### Powder Characteristics

| | TZ-3Y-E | TZ-3YS-E | TZ-4Y | TZ-6Y | TZ-8Y | TZ-8YS | TZ-10YS | TZ-3Y20A | TZ-0 |
|---|---|---|---|---|---|---|---|---|---|
| $Y_2O_3$ (wt%) | 5.2 ± 0.5 | | 7.0 ± 0.6 | 10.3 ± 0.6 | 13.3 ± 0.6 | | 15.9 ± 0.7 | 3.9 ± 0.3 | − |
| $Al_2O_3$ (wt%) | 0.1 ~ 0.4 | | ≦ 0.1 | | | | | 18 ~ 22 | ≦ 0.1 |
| $SiO_2$ (wt%) | ≦ 0.02 | | | | | | | | |
| $Fe_2O_3$ (wt%) | ≦ 0.01 | | | | | | | | |
| $Na_2O$ (wt%) | ≦ 0.04 | | ≦ 0.06 | ≦ 0.12 | | | | ≦ 0.04 | ≦ 0.04 |
| Specific Surface Area ($m^2$/g) | 16 ± 3 | 7 ± 2 | 16 ± 3 | | | 7 ± 2 | 6 ± 2 | 15 ± 3 | 14 ± 3 |

### Typical Properties of Sintered Body

| | TZ-3Y-E | TZ-3YS-E | TZ-4Y | TZ-6Y | TZ-8Y | TZ-8YS | TZ-10YS | TZ-3Y20A | TZ-0 |
|---|---|---|---|---|---|---|---|---|---|
| Density ($g/cm^3$) | 6.05 | | 6.05 | 6.02 | 5.90 | | 5.80 | 5.50 | − |
| Bending Strength R.T. (MPa)[1] | 1200 | | 1000 | 500 | 300 | | 200 | 2000 (HIPing) | − |
| Hardness (Hv10)[2] | 1250 | | | | | | | 1400 | − |

*1 : JIS R1601 ( 3-point bending test )     *2 : JIS R1610 ( Loads : 98.07N )

**Annexe A.3: LSGM Sigma-Aldrich:**

# SIGMA-ALDRICH®

## Product Specification

**Product Name:**
Lanthanum gallate, strontium and magnesium doped – powder, 0.3–0.6 µm, 99% trace rare earth metals basis

| | | |
|---|---|---|
| **Product Number:** | 757357 | $La_{0.8}Sr_{0.2}Ga_{0.8}Mg_{0.2}O_3$ |
| **CAS Number:** | 165900-07-2 | |

**Formula:** La0.8Sr0.2Ga0.8Mg0.2O3
**Formula Weight:** 237.29 g/mol

| TEST | Specification |
|---|---|
| Appearance (Color) | White to Light Brown |
| Appearance (Form) | Powder |
| X-Ray Diffraction | Conforms to Structure |
| Surface Area | 4 - 8 m2/g |
| Particle Size (µm) (d50) | 0.4 - 0.8 |
| Purity 99% Based On Rare Earth Analysis | Meets Requirements |
| Trace Rare Earth Analysis | $\leq$ 20000.0 ppm |

Specification: PRD.1.ZQ5.10000031358

**UNIVERSITAT POLITÈCNICA DE CATALUNYA**
BARCELONA**TECH**
Escola d'Enginyeria de Barcelona Est

**Annexe A.4: Gadolinium (III) Alfa-Aesar:**

**ThermoFisher**
S C I E N T I F I C

**Product Specification**

## 36355 Gadolinium(III) oxide, 99.9% (REO)

| | |
|---|---|
| **Product Number:** | 36355 |
| **CAS number:** | 12064-62-9 |
| **MDL number:** | MFCD00011026 |
| **Molecular formula:** | $Gd_2O_3$ |
| **Molecular weight:** | 362.50 |

## Product Specification

| | |
|---|---|
| **Total Rare Earth Oxide Impurities:** | 0.1% max. |

| | |
|---|---|
| **Date of Print:** | June 9, 2020 |
| **Version:** | 1 |

Product Specifications are subject to amendment and may change over time.

UNIVERSITAT POLITÈCNICA DE CATALUNYA
BARCELONA**TECH**
Escola d'Enginyeria de Barcelona Est

## Annexe A.5: Synolite 0328-A-1:

**Product Data Sheet**

DSM
BRIGHT SCIENCE. BRIGHTER LIVING.

## Synolite 0328-A-1

### Applications
Synolite 0328-A-1 is recommended for the production of water clear castings and encapsulations.

### Principal properties
Synolite 0328-A-1 is a pre-accelerated low reactivity orthophthalic acid based resin with a very gradual cure. The product has a low peak exotherm combined with a low polymerisation shrinkage and high brilliance after polymerisation. This resin is UV-light stabilised.

### Product specifications upon delivery

| Property | Range | Unit | TM |
|---|---|---|---|
| Viscosity, 23°C | 360 - 620 | mPa.s | 2013 |
| Colour, APHA | max. 70 | - | 2017 |
| Solids content, IR | 61.5 - 64.5 | % | 2033 |
| Refractive index, 23°C | 1.545 - 1.547 | - | 2150 |
| Appearance | clear | - | 2265 |
| Colour | blue | - | |
| Water content | Max. 1000 | ppm | 2350 |
| Acid value, as such | 12 - 18 | mg KOH/g | 2401 |
| Gel time from 25 to 35°C | 19 - 23 | minutes | 2625 |
| Cure time from 25°C to peak | 42 - 57 | minutes | 2625 |
| Peak temperature | 40 - 50 | °C | 2625 |

Remarks:
TM 2013: Z2/100s$^{-1}$/23°C
TM 2625: 1.0 g Butanox M50 (Akzo) in 100 g resins

### Other data

| Property | Value | Unit | TM |
|---|---|---|---|
| Density, 20°C | appr. 1100 | kg/m³ | 2160 |
| Flash point | appr. 33 | °C | 2800 |
| Stability, no init., dark, 25°C | 6 | months | - |

### Typical physical properties of cast unfilled resin

| Property | Value | Unit | TM |
|---|---|---|---|
| Density, 20 °C | appr. 1100 | kg/m³ | 2160 |
| Volume shrinkage | 6,1 | % | - |
| Tensile strength | 56 | MPa | ISO 527-2 |
| Elongation at break | 1,6 | % | ISO 527-2 |
| Flexural strength | 83 | MPa | ISO 178 |
| Modulus of elasticity in tension | 4,1 | GPa | ISO 178 |
| Heat deflection temperature (HDT) | 55 | °C | ISO 75-A |
| Barcol hardness | 40-45 | Barcol | GYZJ 934-1 |
| Martens temperature | 49 | °C | DIN 53548 |

### Guidelines before use
Before use, the resin should be conditioned at a well defined, application dependant temperature (usually 15°C minimum for a MEKP cure). Stir the product before blending.

### Storage guidelines
The resin should be stored indoors in the original, unopened and undamaged packaging, in a dry place at temperatures between 5°C and 30°C.
Shelf life is reduced at higher temperatures and the properties of the resin might change during storage. The shelf life of styrene containing unsaturated polyesters will be significantly reduced when exposed to light. Store in dark and in 100% light tight containers only.

### Material Safety
A material safety data sheet for the product is available on request.

### Test methods
Test methods (TM) referred to in the table(s) are available on request

I1,0

UNIVERSITAT POLITÈCNICA DE CATALUNYA
BARCELONATECH
Escola d'Enginyeria de Barcelona Est

# Annexe B: Software

## Annexe B.1: SolidWorks

*SolidWorks* is a 3D part design and modelling software, which the university pays the license. In this project this software is used to generate the layer to print. The principal tools that are used are the scratch to make the shape and the extruder tool to get a 3D figure with the high that the machine and the nozzle require. Finally the program gets to you a *STL.* file.

This file before of been read by the *Slic3r* software is needed to be processed by another program: *Netfabb.*

### Netfabb:

**Available:** https://www.autodesk.com/education/free-software/netfabb, visited 15/03/2020.

Netfabb brings additive design and manufacturing tools together in a single software environment, giving product designers and engineers all the tools they need to optimize, validate and successfully produce models using additive manufacturing processes.

In this Matser's project this software is used to adjust and perform the *STL.* file before the *Slic3r* modification. The two main parameters are the centred of the figure and the correction of triangularization of the shape.

## Annex B.2: Slic3r

**Available:** http://slic3r.org/, visited 15/03/2020

*Slic3r* is the tool you need to convert a 3D model into printing instructions for your 3D printer. It cuts the model into horizontal slices (layers), generates toolpaths to fill them and calculates the amount of material to be extruded.

This free program is used in the university to generate the *Gcode.* files directly used in the 3D-printing machine. It gives the possibility of modify the main printing parameters: infill of the layer, the geometry of the infill and the printing velocity. Also this program needs some inputs parameters for print like the size of the nozzle and the size of the printing bed.

In the following part, a brief explanation of the inputs used during this Master's project will be presented:

1. First of all is important to export de *STL.* file and go to *File → Export Conf Bundle →* and select the file of the extruder that you are going to use.

2. The first parameter that you need to modify is the *Printing Settings (**Figure B.1**)*. In **Figure B.2 a** are presented all the parameters.

   - **Layers and perimeters:**
     - *Layer height: h =* Diameter of the nozzle - (0.1*diameter of the nozzle) in the both options.
     - *Vertical shells* (for perimeters): *perimeter =* 1, and choose *Spiral vase*.
     - *Quality* (for perimeters): choose all the four options

   - **Infill:**
     - *Infill:* the *Fill density* for this master's project are: 100%, 90%, 80%, 70%, 60%, 50%, 40%. The *Fill pattern* and *Top/bottom fill pattern → Rectilinear*.
     - *Advanced:* In this option is just needed to modify the *Fill angle* every layer rotating it 90º, to get better mechanical properties.

   - **Speed:**
     - *Speed for print moves:* Were reduce between 2 to 3 mm/s, depending on the infill of the sample .
     - *Speed for non-print moves*: Reduce the velocity to 25 mm/s.

   - **Skirt and brim:**
     - *Skirt: Loops =* 1.

3. The following parameter is the *Printer Settings (**Figure B.1**)*. In the **Figure B.2 b** are presented all the parameters.

   - **General:**
     - *Size and coordinates:*
       - *Bed size: x =* 100; *y =* 100 mm.
       - *Print center: x =* 50; *y =* 50 mm.
       - *Z offset :* 0

   - **Extruder 1:**
     - *Size: Nozzle diameter:* the diameter of the nozzle that you are going to use.
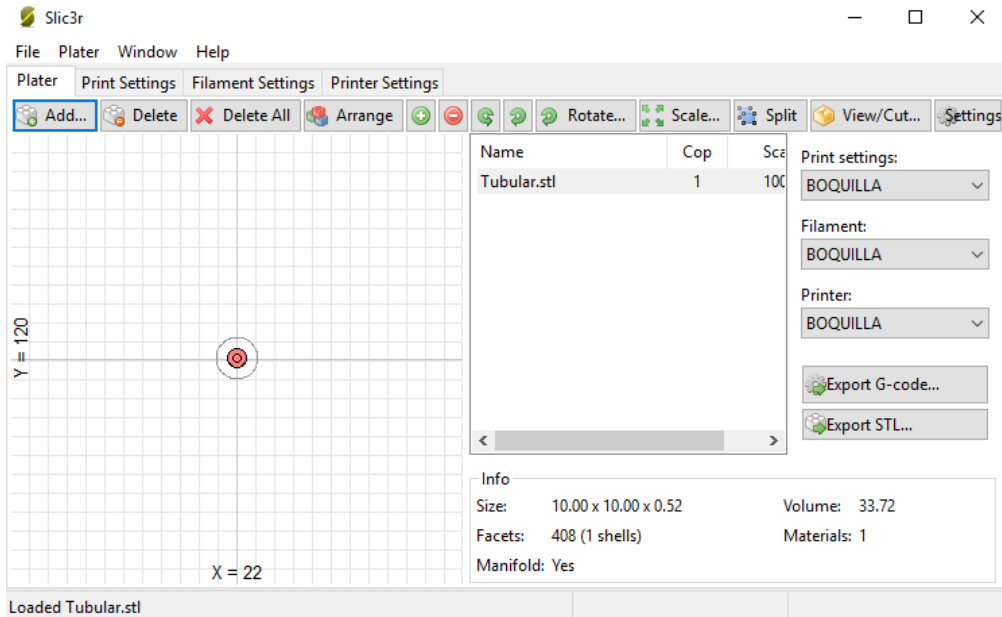
*Figure B.1: Main display of the software.*

**a)**



**b)**
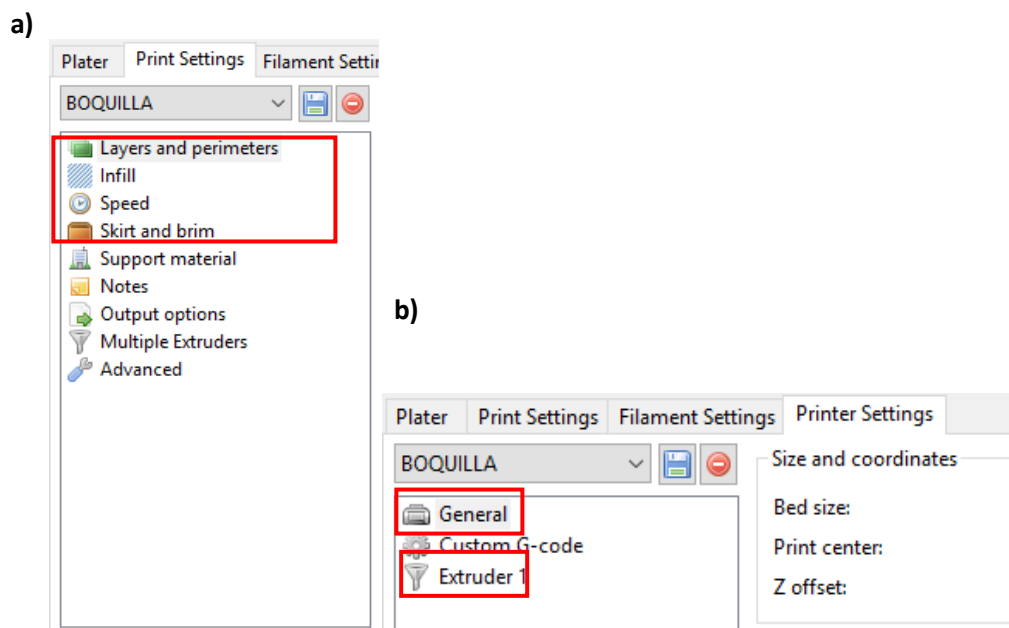


*Figure B.2:Both main menus of the principal paremetrs. a) Main menu of the* Print Settings. *b) Main menu of the* Printer Settings.

## Annex B.3: ImageJ

**Available:** https://imagej.nih.gov/ij/, visited 15/03/2020

*ImageJ* is an image processing and analysis software written in Java, which allows it to run on Linux, Mac OS X and Windows, in both 32-bit and 64-bit modes. *ImageJ* and its Java source code are freely available and in the public domain. No license is required.

In this Master's project this software is used to measure and for image processing in order to characterize the shrinkage of the samples.

In the following part, a brief explanation of these two applications will be presented.

A.  **Measure:** This application is used to measure different parameters of an image.
    1.  Select the option to make lines in the picture (**Figure B.3**) and draw a line in the scale line push in *Ctrl+D.*
    2.  After that go to *Analyze (**Figure B.1 c)** and chose *Set scale,* **Figure B.4.a**. A new windows will be open (see **Figure B.4.b**).
    3.  In the new windows the part of *Know distance*, goes the measure of the scale of the treated picture. Then in the part of *Unit of length*, goes the unit of the scale.
    4.  Finally with the option of drawing line (**Figure B.3**) you can draw lines and measure them push in *Ctrl+M,* and a new window is opened with all the measures.
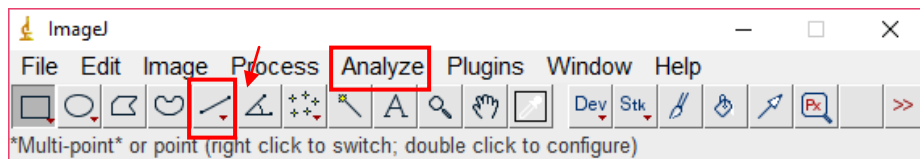


*Figure B.3: Principal menu of the* ImageJ *software.*
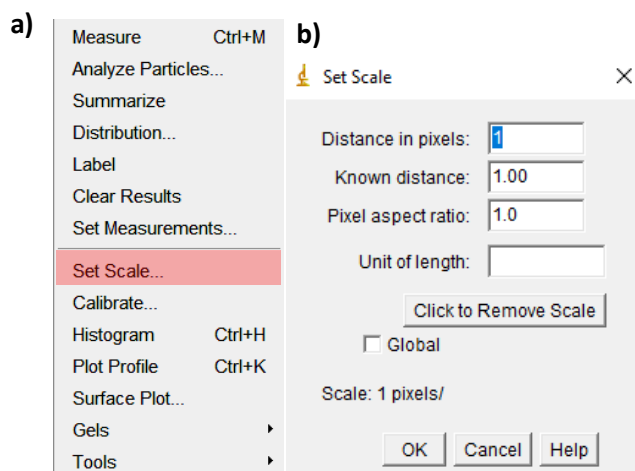


*Figure B.4: Analyze menu. a)Main analyze menu. b) Set scale window.*

## Annexe C: Nozzle catalogue from Nordson

# Precision Dispense Tips

## PRECISION STAINLESS STEEL TIPS

| Gauge | | Color | ID mm | ID inch | OD mm | OD inch | 6.35 mm (0.25") | 12.7 mm (0.50") | 25.4 mm (1.0") | 38.1 mm (1.5") | 45°/12.7 mm (0.5") | 90°/12.7 mm (0.5") | 45°/38.1 mm (1.5") | QTY |
|---|---|---|---|---|---|---|---|---|---|---|---|---|---|---|
| 14 | | Olive | 1.54 | 0.060 | 1.83 | 0.072 | 7018029 | 7018043 | 7018032 | 7018035 | 7018044 | 7018045 | 7016906 | 50 |
| 15 | | Amber | 1.36 | 0.053 | 1.65 | 0.065 | 7018056 | 7018068 | 7018059 | 7018062 | 7018069 | 7018070 | n/a | 50 |
| 18 | | Green | 0.84 | 0.033 | 1.27 | 0.050 | 7018107 | 7018122 | 7018110 | 7018113 | 7018123 | 7018124 | 7016908 | 50 |
| 20 | | Pink | 0.61 | 0.024 | 0.91 | 0.036 | 7018163 | 7018178 | 7018166 | 7018169 | 7018179 | 7018180 | n/a | 50 |
| 21 | | Purple | 0.51 | 0.020 | 0.82 | 0.032 | 7005005 | 7018233 | 7018222 | 7018225 | 7018234 | 7018235 | 7016910 | 50 |
| 22 | | Blue | 0.41 | 0.016 | 0.72 | 0.028 | 7018260 | 7018272 | 7018263 | 7018266 | 7018273 | 7018274 | n/a | 50 |
| 23 | | Orange | 0.33 | 0.013 | 0.65 | 0.025 | 7018302 | 7018314 | 7018305 | 7018308 | 7018315 | 7018316 | n/a | 50 |
| 25 | | Red | 0.25 | 0.010 | 0.52 | 0.020 | 7018333 | 7018345 | 7018336 | 7018339 | 7018346 | 7018347 | n/a | 50 |
| 27 | | Clear | 0.20 | 0.008 | 0.42 | 0.016 | 7018395 | 7005008 | n/a | n/a | 7018404 | 7018405 | n/a | 50 |
| 30 | | Lavender | 0.15 | 0.006 | 0.31 | 0.012 | 7018424 | 7018433 | n/a | n/a | 7018434 | 7018435 | n/a | 50 |
| 32 | | Yellow | 0.10 | 0.004 | 0.24 | 0.009 | 7018462 | n/a | n/a | n/a | n/a | n/a | n/a | 50 |

Burr-free, polished, passivated stainless steel dispense tips with polypropylene SafetyLok™ hubs for a secure fit to barrel reservoirs.

## SMOOTHFLOW TAPERED TIPS

| Gauge | | Color | ID mm | ID inch | Standard | Opaque Rigid | QTY |
|---|---|---|---|---|---|---|---|
| 14 | | Olive | 1.60 | 0.063 | 7018052 | 7018049 | 50 |
| 16 | | Grey | 1.19 | 0.047 | 7018100 | 7018097 | 50 |
| 18 | | Green | 0.84 | 0.033 | 7018158 | 7018147 | 50 |
| 20 | | Pink | 0.58 | 0.023 | 7005009 | 7005006 | 50 |
| 22 | | Blue | 0.41 | 0.016 | 7018298 | 7005007 | 50 |
| 25 | | Red | 0.25 | 0.010 | 7018391 | 7018370 | 50 |
| 27 | | Clear | 0.20 | 0.008 | 7018417 | n/a | 50 |

Use with gel cyanoacrylates, UV-cure adhesives, sealants, and particle-filled materials or any medium to high viscosity fluid. Standard tips are molded of polyethylene with UV-light block additive. Rigid, opaque tapered tips are molded of polypropylene and the opacity delivers light-blocking functionality.

## CHAMFERED TIPS

| Gauge | | Color | ID mm | ID inch | 38.1 mm (1.50") | 12.7 mm (0.50") | 6.35 mm (0.25") | QTY |
|---|---|---|---|---|---|---|---|---|
| 18 | | Green | 0.84 | 0.033 | n/a | 7018129 | n/a | 50 |
| 20 | | Pink | 0.61 | 0.024 | 7018188 | n/a | n/a | 50 |
| 22 | | Blue | 0.41 | 0.016 | 7018281 | n/a | n/a | 50 |
| 23 | | Orange | 0.33 | 0.013 | n/a | 7018321 | n/a | 50 |
| 25 | | Red | 0.25 | 0.010 | n/a | 7018352 | n/a | 50 |
| 27 | | Clear | 0.20 | 0.008 | n/a | n/a | 7015236 | 50 |
| 33 | | Clear | 0.10 | 0.004 | n/a | n/a | 7018482 | 25 |
| 33 | | Black | 0.10 | 0.004 | n/a | n/a | 7018477 | 25 |

Use for microdot application of low viscosity fluids.

## PTFE-COATED TIPS

| Gauge | | Color | ID mm | ID inch | OD mm | OD inch | 12.7 mm (0.50") | QTY |
|---|---|---|---|---|---|---|---|---|
| 21 | | Purple | 0.51 | 0.020 | 0.84 | 0.033 | 7018243 | 20 |
| 22 | | Blue | 0.41 | 0.016 | 0.74 | 0.029 | 7018290 | 20 |
| 23 | | Orange | 0.33 | 0.013 | 0.66 | 0.026 | 7018326 | 20 |
| 25 | | Red | 0.25 | 0.010 | 0.53 | 0.021 | 7018359 | 20 |

Controls wicking to stop drips for optical media applications.

## PTFE-LINED TIPS

| | Color | ID mm | ID inch | 12.7 mm (0.50") | 25.4 mm (1.0") | QTY |
|---|---|---|---|---|---|---|
| | Grey | 0.51 | 0.020 | 7018256 | 7005003 | 50 |
| | Pink | 0.30 | 0.012 | 7018388 | 7005004 | 50 |

Resists clogging of cyanoacrylates. Use for microdot application of low viscosity fluids.

## FLEXIBLE TIPS

| Gauge | | Color | ID mm | ID inch | 12.7 mm (0.50") | 38.1 mm (1.5") | QTY |
|---|---|---|---|---|---|---|---|
| 15 | | Amber | 1.36 | 0.053 | 7018085 | 7018080 | 50 |
| 18 | | Green | 0.84 | 0.033 | 7018143 | 7018138 | 50 |
| 20 | | Pink | 0.61 | 0.024 | 7018205 | 7018201 | 50 |
| 25 | | Red | 0.25 | 0.010 | 7018366 | 7018362 | 50 |

Flexible polypropylene tubing for application into difficult-to-access areas. Easily drags along edges and around corners and prevents scratching. Tubing can be cut to length.

## OVAL TIPS

| Gauge | | Color | 12.7 mm (0.50") | QTY |
|---|---|---|---|---|
| 15 | | Amber | 7018078 | 50 |
| 18 | | Green | 7024653 | 50 |
| 23 | | Orange | 7024656 | 50 |

Flat ribbon deposits of thick pastes, sealants, and epoxies.

UNIVERSITAT POLITÈCNICA DE CATALUNYA
BARCELONATECH
Escola d'Enginyeria de Barcelona Est